ABSTRACT

Title of dissertation: LOW-LATENCY SEARCHES FOR GRAVITATIONAL WAVES AND THEIR ELECTROMAGNETIC COUNTERPARTS WITH ADVANCED LIGO AND VIRGO

Min-A Cho, Doctor of Philosophy, 2019

Dissertation directed by: Professor Peter Shawhan
Department of Physics

For the first time in history, advanced detectors are available to observe the stretching and squeezing of space—gravitational waves—from violent astrophysical events. This opens up the prospect of joint detections with instruments of traditional astronomy, creating the new field of multi-messenger astrophysics. Joint detections allow us to form a coherent picture of the unfolding event as told by the various channels of information: mass and energy dynamics from gravitational waves, charged particle environments (along with magnetic field and specific element environments) from electromagnetic radiation, and thermonuclear reactions/relativistic particle outflows from neutrinos.

In this work, I motivate low-latency electromagnetic and neutrino follow-up of sources known to emit gravitational radiation in the sensitivity band of ground-based interferometric detectors, Advanced LIGO and Advanced Virgo. To this end, I describe the low-latency infrastructure I developed with colleagues to select and enable successful follow-up of the first few gravitational-wave candidate events in history, including the first binary black hole merger, named GW150914, and binary neutron star coalescence, named GW170817,

from the first and second observing runs.

As a review, I outline the theory behind gravitational waves and explain how the advanced detectors, low-latency searches, and data quality vetting procedures work. To highlight the newness of the field, I also share results from an offline search for a more speculative source of gravitational waves, intersecting cosmic strings, from the second observing run.

Finally, I address how LIGO/Virgo is prepared to adapt to challenges that will arise during the upcoming third observing run, an era that will be marked by near-weekly binary black hole candidate events and near-monthly binary neutron star candidate events. To handle this load, we made several improvements to our low-latency infrastructure, including a new, streamlined candidate event selection process, expansions I helped develop for temporal coincidence searches with electromagnetic/neutrino triggers, and data quality products on source classification and probability of astrophysical origin to provide to our observing partners for potential compact binary coalescences. These measures will further our prospects for multi-messenger astrophysics and increase our science returns.

LOW-LATENCY SEARCHES FOR GRAVITATIONAL WAVES AND THEIR ELECTROMAGNETIC COUNTERPARTS WITH ADVANCED LIGO AND VIRGO

by

Min-A Cho

Dissertation submitted to the Faculty of the Graduate School of the
University of Maryland, College Park in partial fulfillment
of the requirements for the degree of
Doctor of Philosophy
2019

Advisory Committee:
Professor Peter Shawhan, Chair/Advisor
Professor Paulo Bedaque
Professor Sarah Eno
Professor Jordan Goodman
Professor M. Coleman Miller, Dean's Representative

For my umma and appa, Inseon Cho-Kim and Kijo Cho,
and for my unni, Min Jeong Cho.

"My heart is a traitor," the boy said to the alchemist, when they had paused to rest the horses. "It doesn't want me to go on."

"That makes sense. Naturally it's afraid that, in pursuing your dream, you might lose everything you've won."

"Well, then, why should I listen to my heart?"

"Because you will never again be able to keep it quiet. Even if you pretend not to have heard what it tells you, it will always be there inside you, repeating to you what you're thinking about life and about the world."

"You mean I should listen, even if it's treasonous?"

"Treason is a blow that comes unexpectedly. If you know your heart well, it will never be able to do that to you. Because you'll know its dreams and wishes, and will know how to deal with them."

Paulo Coelho, the Alchemist

Acknowledgments

Professor Peter Shawhan, thank you for mentoring me and advising me through the past 6 years of my life. When I applied to graduate school at the University of Maryland, I remember thinking, "Wow! It would be so cool if I could work for this guy and work on detecting gravitational waves..." Thus, I have been truly fortunate to be one of your graduate students. Aside from the physics, seeing you interact with your colleagues, students, and family, I've also learned how to become a better and kinder person under your advisory. Thank you.

Professors Paulo Bedaque, Sarah Eno, Jordan Goodman, and M. Coleman Miller, thank you for encouraging *cough terrorizing* me while being a part of my doctoral committee. I appreciate your incisive questions and detailed feedback during my examination. In particular, thank you Professor Sarah Eno, because you told me to seek support early on in my graduate studies when my mom's health was deteriorating. I appreciate that to this day because I needed it!

Dr. Timothy Edberg, Pauline Rirksopa, and Cregg Yancey, you made my day-to-day life at work more fulfilling and enjoyable, so thank you. Tim, it is always a pleasure to say hello to you. It also makes me happy to look at your nature photography. Pauline, I adore you! I cherish our 5 or 10 minute conversations and your laughter. I hope you are having fun traveling with your husband in your retirement. Cregg, my one and only office mate. Thank you for your whiteboard explanations, your stories, and your friendship. I will miss all of these things.

Paulina Alejandro, Lorraine DeSalvo, Donna Hammer, and Sally Megonigal, thank you for making life manageable—not just for me, but also for many

other graduate students, professors, and researchers. I would not have had access to my office after hours or health insurance or travel reimbursement or opportunities to do public outreach if it weren't for you. Thank you.

Professors Tom Antonsen, Alessandra Buonanno, Adil Hassam, Ted Jacobson, Ed Ott, and Min Ouyang, thank you because I either enjoyed taking your graduate level course or being your teaching assistant. To Professor Ed Ott, I would like to point out that I found your doppelgänger. He is also a professor albeit in the animated series Futurama.

Professors Christoph Boehme, John DeFord, Henryk Hecht, Stefan LeBohec, and Nicholas Korevaar, thank you because you shaped my undergraduate studies. Professor Boehme, you once told me to study something I am naturally curious about, because it will keep me going—especially when the times get hard... It proved to be profound advice; I have passed it along to other students as well.

Sarah Antier, Deep Chatterjee, Shaon Ghosh, Giuseppe Greco, Barbara Patricelli, Karelle Siellez, and Koh Ueno (a.k.a. the O2 EM Follow-up Paper Writing Team)—Yay, we did it! Thank you because it's been an honor working with you guys. I cherish our friendship and am inspired by your scholarship. Don't ever hesitate to reach out!

Imène Belahcene, Kipp Cannon, Florent Robinet, and Daichi Tsuna (the O2 Cosmic Strings Search Analysis Team), thank you for accepting me into the team and for your patience while teaching me. Imène and Daichi, I am also thankful for our friendship; I hope we keep in touch.

Patrick Brady, Marica Branchesi, Gaby González, Jonah Kanner, Erik Katsavounidis, Laura Nuttall, and Leo Singer, thank you for entrusting me with important tasks and for believing in me. With great trust comes great responsibility... I also want to thank you Leo, for elevating my standards,

whether it came to coding practices and style or dissertation and presentation aesthetics. I was definitely inspired!

Imani Herring, Nishat Mhamud, and Arul Teimouri, thank you for filling our house with laughter. Arul, my fellow INFP and book enthusiast! Thank you for being my friend through all the ups and downs this past year. I look forward to more swimming adventures with you and Melanie, perhaps in Cuba next time. *Wink*

Amanda Alexander, Adella Croft, Connie Eng Fulkerson, Maria Garcia, Julia Schneider, Olha Krechkivska, and Izzy Velez, thank you for your love and support throughout the years. I miss and love you guys!

Chaka Freeman, Tingting Liu, Joe Murray, Dalia Ornelas, Holly Tinkey, Ana Valdés, Chiao-Hsuan Wang, Hongcheng Xu, and Vitaley Zaretsky. Thank you for your friendship, I am glad we got to meet and get to know each other. I adore you all. Chaka, one word: all-sky! Holly, you have a great sense of humor. (Are skin pockets still a thing?) Tingting, my fellow ballet enthusiast! Hongcheng, my National Geographics worthy birder.

Renee Ren-Patterson, I look up to you for so many different reasons—each time I talk with you I learn something new, and I love it. Thank you. You are my beauty and brains inspo.

Omar Ortiz, I'm so glad we became friends! Thank you for all of the laughter and tears; I'm looking forward to more memories and can't wait to see what the future holds!

Sharon Wall and Meghan Hughes. Four words: annual Christmas cookie-baking parties! Sharon, because of you I had family away from family my first few years of graduate school. Thank you for letting me get to know them. Mr. and Mrs. Wall, Leeroy, Jess, Aunt Cheryl, Audrey and Mike, Ashlee and Susie, thank you for accepting me with open arms. Leeroy, thank you for being

my brother (I've always wanted one!). Also Sharon, because of you I started eating much healthier and am aware of nutrition—thank you babe!

Yao Odamtten, Vincent W. Williams, and Julieane 'Julie' Hill. Yao, thank you for your LARGE LOVE AND SPIRIT. There is no other way to put it. You are a shining star in my heart. You are a shining star, PERIOD! Vincent, the other shining star in my heart. How did I get so lucky? Thank you for being my friend, boo! Julie, my sweet, smart, kind, and beautiful friend! Sometimes I smile and think to myself, "Wow, there are people like Julie in the world!", and I know I'm not alone in thinking that *cough Vincent and Yao*; I love you guys! Let's keep on dancing.

Naasir Ali, Alex 'Axiz' Benitez, Geoffrey 'Toyz' Chang, Carrington Lewis-Sweeney, Jonathon 'Frenzy' Marie, Kerrie 'Kerrie-Sauce' Marie, Nelson Mencho, Fasil Sheta, Julie 'Ju-Ju' Stoessel, Grisha Tikhonov, and James Ulmer. I am so lucky to have met and danced with you guys! You are all so mad talented. Fasil, please keep drawing! Carrington, I consider you one of my closest friends although I hardly ever see you. Alex, eres mi tesoro, the Hobbes to my Calvin. Thank you for sharing life's little moments with me, and making everything a little bit sweeter. *Mwah*

John (cat), Piyali 'Pipi' Das, Davy Foote, John Giannini, Prasoon Gupta, and Luke 'Lukey' Robertson (a.k.a. The Perch Family), I love you guys! I petition that we meet up at least once a year. Pipi and Lukey... I could not have made it through this past year without your support. *Squeeze*

Benjamin Chung (정복헌) and Christine Chung (위성숙), thank you for reaching out when my mom passed. I know that your family was important to her and that she cherished your friendship.

Suok Pak (박수옥) and Kyongsook Kim (김경숙), I consider you both like my godmothers, and I'm so lucky! I love you both, and thank you for

helping me become who I am today. I also want to say thank you for being close friends with my mom, and for being there for her. That means the world to me. On a similar note, I would like to thank my mom's dear friends, Samuel Roh and Jungsooki-eemo... Thank you from the bottom of my heart.

Weh-halmunee (선귀화) and weh-halabujee (김영택), thank you for loving me and my sister unconditionally throughout the years. We felt it even from overseas, especially with your homemade kimchi and side dishes, halmunee! I would love to meet you again—soon—to cook with you and listen to your stories. Halabujee, I wish I could buy you pizza one more time and go hiking! Rest In Peace.

Umma (김 인 선) and appa (조 기 조). Minnie (조 민 정) and Darami. Darami, sweet baby sister. When you were five (six?), you asked me, "Min-A, what is treasure?" and I said, "Treasure is something you love and hold dear in your heart." Wherever you are, you are so loved—and treasured! Umma, I miss you and think about you all the time... Appa! I will always remember your words, "힘들겠지만 즐겁게 생각하고 하자." Words to live by.

Umma and appa, the most important thing you've taught me is to be a promise keeper to myself. I evaluate daily whether my action or inaction for the day has measured up to what I say I want for my life. Thank you for guiding me to become a more accountable and self-actualized human being. And more than anything, thank you for your love and support. It gave me the courage to dream and to go after my dreams.

Lastly, to my older sister Minnie. You are the person I look up to the most! There is no one more grounding than you. Thank you for being able to tell me the hard things I need to hear in life. You are my rock and keeper, and I am your rock and keeper too. Love you.

Contents

List of Figures

List of Tables

List of Abbreviations

1RXS first Röntgensatellit X-ray Survey; astronomical catalog

3XMM third XMM-Newton Serendipitous Source Catalogue; astronomical catalog

ADVREQ advocate required

AGN active galactic nuclei

aLIGO Advanced LIGO

AXP anomalous X-ray pulsar

BAYESTAR Bayesian Triangulation And Rapid Localization; software package for gravitational-wave events

BBH binary black hole

BH black hole

BNS binary neutron star

CBC compact binary coalescence

CCO central compact object

CCSN core-collapse supernova

CDF cumulative distribution function

CMB cosmic microwave background

CSM circumstellar medium

cWB coherent WaveBurst; software package for gravitational-wave events

DM dispersion measure

DWD double white dwarf

FAP false alarm probability

FAR false alarm rate

FGMC Farr-Gair-Mandel-Cutler

FITS flexible image transport system

GBM the Gamma-ray Burst Monitor instrument on board the Fermi Gamma-ray Space Telescope

GCN Gamma-ray Coordinates Network

GLADE Galaxy List for the Advanced Detector Era; galaxy catalog

GPS the Global Positioning System

GraceDb gravitational-wave candidate event database

GRB gamma-ray burst

GstLAL GStreamer LAL; software package for gravitational-wave events

GUT grand unified theory

GW gravitational wave

HMNS hypermassive neutron star

ICRS international celestial reference system

IFAR inverse FAR

IIR infinite impulse response

INTEGRAL the International Gamma-Ray Astrophysics Laboratory; space telescope

IR infrared

ISI internal seismic isolation platform

ISM interstellar medium

KAGRA Kamioka Gravitational Wave Detector

LAL LIGO algorithm library; software package for gravitational-wave events

LIGO Laser Interferometer Gravitational-wave Observatory

LISA Laser Interferometer Space Antenna

LOOC UP Locating and Observing Optical Counterparts to Unmodeled GW Pulses; project for gravitational-wave event follow-up during the Initial LIGO era

LVAlert LIGO-Virgo alert system

LVT LIGO-Virgo trigger

MBTA Multi-Band Template Analysis; software package for gravitational-wave events

MCMC Markov chain Monte Carlo

ML maximum likelihood

MOU memorandum of understanding

NGC New General Catalogue; astronomical catalog

NIR near-infrared

NS neutron star

NS-BH neutron star-black hole

oLIB Omicron LALInferenceBurst; software package for gravitational-wave events

P_astro probability of astrophysical origin

PDF probability density function

PN post-Newtonian

PSD power spectral density

PSR pulsar

pubsub publish-subscribe

PyCBC python CBC; software package for gravitational-wave events

QED quantum electrodynamics

RAVEN rapid, on-source VOEvent coincidence monitor; software package for gravitational-wave events

RESTful API representational state transfer application program interface

RMS root mean square

RRAT rotating radio transient

RRT rapid response team

RSE resonant sideband extraction

SAA South Atlantic anomaly

SGR soft gamma-ray repeater

sGRB short gamma-ray burst

skymap sky localization probability map

SN supernova

SNEWS SuperNova Early Warning System

SNR signal-to-noise ratio

SPI-ACS the Spectrometer and Anti-Coincidence Shield on board INTEGRAL

SPIIR Summed Parallel Infinite Impulse Response; software package for gravitational-wave events

SR signal recycling

SRC signal recycling cavity

SSB solar system barycenter

STF symmetric trace-free

TF time-frequency

TT transverse trace-free

UTC coordinated universal time

VOEvent virtual observatory event

WDM Wilson-Daubechies-Meyer

XDIN X-ray dim isolated neutron star

XMM X-ray Multi-Mirror Mission; space observatory

XMPP extensible messaging and presence protocol

XTE X-ray Timing Explorer; space telescope

Chapter 1

Multi-Messenger Sources and Motivations

The state of gravitational-wave physics before the discovery of the Hulse-Taylor binary pulsar system PSR B1913+16 (Hulse & Taylor, 1975; Taylor et al., 1976; Taylor & Weisberg, 1982) in many ways resembled the state of neutrino physics in the 1940's and 1950's. As one contemporary observer noted, "There can be no two opinions about the practical utility of the neutrino hypothesis ... but ... until clear experimental evidence for the existence of the neutrino could be obtained ... the neutrino must remain purely hypothetical" (Ellis, 1937). Then, in 1959, Reines and Cowan delivered the first crucial bit of evidence: the first direct observation of the free neutrino (Cowan et al., 1956). Fast-forward a few decades and today neutrinos are considered by astrophysicists to be a valuable probe of the structure of matter and perhaps less well-known, a key ingredient to reviving stalled stellar core-collapse explosions (Section 1.1).

The first serious attempt to detect gravitational waves began with Joseph Weber at the University of Maryland, College Park in the 1960's. Previous to his efforts, gravitational waves, while deemed essential for the structural integrity of the General Theory of Relativity (Einstein, 1916, 1918), seemed so weak in their visible manifestations that Einstein himself believed that they would never be detected, and perhaps even worse, that they would be of no practical importance. Not to be deterred, Weber built his aluminum bar detectors and his claim of detection in 1969 (Weber, 1969) propelled others to

attempt to do the same—and more importantly—convinced the skeptics that detection could be possible. While results of the bar detector experiments were not reproduced, in 1974, the discovery of the Hulse-Taylor binary pulsar (see Section 2.4) confirmed the existence of gravitational waves.

In present-day gravitational-wave physics, theory is now confirmed by direct observations with advanced ground-based interferometric detectors, leading to the advent of gravitational-wave astronomy (e.g., Abbott et al., 2016b,c, 2017c). In addition, recent discovery of gravitational waves from the first binary neutron star coalescence ever observed (Abbott et al., 2017) along with its many electromagnetic counterparts has now signaled that multi-messenger astronomy has officially begun (e.g., Abbott et al., 2017a; Albert et al., 2017; Haggard et al., 2017; Savchenko et al., 2017; Troja et al., 2017; D'Avanzo et al., 2018; Dobie et al., 2018; Margutti et al., 2018; Ruan et al., 2018).

This chapter is dedicated to exploring in depth astrophysical sources expected to be jointly observed by a network of advanced ground-based interferometric detectors and its traditional astronomy partners. Select unsolved problems that are related to these sources are also presented since they could be resolved by such observations.

1.1 Core-Collapse Supernovae

Core-collapse supernovae are the explosive deaths of massive stars that require the full power of general relativity, the strong and weak interactions, electrodynamics, and transport theory in order to be understood. The basics of modern-day core-collapse supernova theory are summarized in this section with a focus on the 50+ year old supernova problem: "How is the stellar core infall eventually reversed so that the disruption of the star is triggered, along with the ejection of the stellar mantle and stellar envelope?"

In the advent of a core-collapse supernova in the Milky Way (suspected to occur once every ∼50 years), it will be possible to explore the supernova problem with advanced ground-based gravitational-wave detectors and/or their near-term upgrades. Therefore, key gravitational-wave signatures from core-collapse supernovae are discussed. In addition, information obtained from gravitational-wave detections from neutron star binaries (Section 1.3) could contribute to the effort of modeling core-collapse supernovae and are therefore included.

The origins of the supernova problem start in 1925, when Pauli stated in his exclusion principle (Pauli, 1925) that electrons from the same quantum system must be in different quantum states. When applied to stars that are counteracting their own attractive force of gravitation, the Pauli exclusion principle prevents electrons in the stars from getting infinitely close to each other. Instead, the electrons are forced to fill up energy levels that are available to them, starting from the very lowest.

However, the sheer number of electrons present in a star means ultimately that some of the electrons end up with high energies, and therefore high momenta. Thus, the electrons moving outward in the star provide a kind of 'electron degeneracy pressure' that can support the star against its own gravitational implosion (e.g., Burrows & Ostriker, 2014):

$$P = \frac{\pi^2 \hbar^2}{5 m_e m_p^{5/3}} \left(\frac{3}{\pi}\right)^{2/3} \left(\frac{\rho}{\mu_e}\right)^{5/3}$$

where $\hbar$ is Planck's constant divided by 2π, m_e is the mass of an electron, m_p is the mass of a proton, ρ is the density, and μ_e is the ratio of electrons to protons.

Here, it is important to note that the same Pauli exclusion principle that is applied for electrons applies for protons as well, although the partial pressure

contribution from the degenerate proton gas is much less in the non-relativistic limit. This is simply due to the high proton-to-electron mass ratio, $\sim$1836, that results in the degenerate proton gas having a kinetic energy $\sim 1/1836$ times the energy of the degenerate electron gas (Schutz, 2004).

An important moment in the life cycle of a star is reached when hydrogen fusion to carbon and oxygen essentially completes and the star is not massive enough to achieve the internal pressure/temperature needed to fuse the carbon and oxygen into heavier elements. In this case, fusion stops, leading to the cooling down of the star at essentially fixed density (i.e., the star begins to shrink). For stars that begin less massive than $\sim 8-10\ M_\odot$, electron degeneracy pressure will halt the shrinking. This occurs when the electron Fermi energy exceeds the electron thermal energy, $k_B T$. For non-relativistic electrons this occurs at $T_{10} \sim 4\rho_8^{2/3}$, and for relativistic electrons at $T_{10} \sim \rho_8^{1/3}$ with $T_x \equiv T/(10^x \text{ K})$ and $\rho_y \equiv \rho/(10^y \text{ g cm}^{-3})$ (Janka, 2012). Such a star is now a white dwarf.

Equally important as Pauli's exclusion principle is Chandrasekhar's discovery in 1931 (Chandrasekhar, 1931) that there is an upper mass limit to stars that can be supported via the above electron degeneracy pressure. In modern-day core-collapse supernova theory, Chandrasekhar's limit (e.g., Woosley et al., 2002) is the starting point for describing the upper mass limit of metastable, degenerate cores at the centers of massive stars near the onset of core-collapse. These cores resemble hot white dwarfs close to their maximum effective Chandrasekhar mass[1] given by:

$$M_{\text{Ch, eff}} \approx 1.44 \left(\frac{Y_e}{0.5}\right)^2 M_\odot + \text{corrections...}$$

[1]The effective Chandrasekhar mass given in the equation is for cold neutron stars. The cores of massive stars which are still hot can have a mass up to a few tenths of a solar mass above $M_{\text{Ch, eff}}$ without collapsing.

where Y_e is the electron fraction, the number density of electrons divided by the total number density of baryons, with typical values $\sim$0.45 (Janka et al., 2012) and $M_\odot$ is one solar mass. Then, because no equilibrium solutions exist for relativistic and degenerate electron gases with $M > M_{\rm Ch,\ eff}$, core-collapse ensues when the stellar core mass exceeds the effective Chandrasekhar limit.

Progenitors

The lowest-mass progenitors of core-collapse supernovae have oxygen-neon-magnesium (ONeMg) cores (Nomoto, 1984, 1987) that reach the electron degeneracy state before hydrostatic Ne-burning can be ignited. However, ONeMg cores experience high rates of electron capture by protons and nuclei in the cores, meaning the electron degeneracy pressure quickly lets up due to a decrease in Y_e. Therefore, these cores are the progenitors of electron capture supernovae (ECSN) which are believed to comprise up to 20$-$30% of all core-collapse supernovae (Wanajo et al., 2009, 2010).

More massive progenitors are able to ignite Ne-burning and develop iron cores which become unstable at temperatures around 10^{10} K ($k_BT \sim 1$ MeV). Then, electron degeneracy pressure support becomes reduced due to photodissociation of the iron-group nuclei (e.g., Janka, 2012; Burbidge et al., 1957) and reactions such as

$$\gamma + {}^{56}_{26}\mathrm{Fe} \leftrightharpoons 13\alpha + 4n$$

favor the production of α-particles which proceed to capture more electrons, speeding up the core-collapse.

In more detail, the collapsing iron core splits into two pieces, an inner core and an outer core, because of radius-dependent local sound speeds and infall velocities. (The outer core falls in supersonically while the inner core falls in subsonically.) However, the collapsing inner core cannot collapse indefinitely

due to the repulsive nature of nucleon-nucleon interactions at extremely short ranges (Bethe & Johnson, 1974). Thus, when the inner core reaches nuclear densities, $\rho_{\rm nuc} \sim 2.7 \times 10^{14}$ g cm^{-3}, the repulsive term of the strong force kicks in, causing the nuclear equation of state there to 'stiffen', i.e., $\Gamma = d \ln P / d \ln \rho$ (or equivalently, the Γ in $P \propto \rho^{\Gamma}$) jumps from 4/3 up to $\sim$2.6$-$2.8 as the composition transitions from inhomogeneous matter (nucleons, α-particles, and nuclei) towards pure nucleons. The effect of this stiffening is that the inner core 'bounces' and launches the shock wave that eventually triggers the supernova (e.g., Mezzacappa et al., 2014).

The shock wave however, stalls, leading to the modern-day supernova problem. As the inner core rebounds and expands into the surrounding outer iron core material, it loses energy due to the dissociation of iron-group nuclei into free nucleons ($\sim$8.8 MeV per nucleon in the post-shock matter). $\sim$1$-$2 ms after the shock formation, velocities downstream from the shock become negative. Finally, the shock comes to a halt when the mass accretion rate from the outer core gets low enough (Janka et al., 2012).

If the shock is not revived within $\sim$0.5$-$3 s, the shock becomes an accretion-shock, and infalling matter from the outer core accretes onto the central object, enabling the formation of a final black hole (Bethe, 1990). Else, the inner core eventually becomes a neutron star or black hole. This is where we introduce the present-day supernova problem.

There are also more energetic supernovae which require magneto-rotational driving but these constitute only 0.1-1% of all core-collapse supernovae (Woosley & Weaver, 1981). The observational evidence for this is indirect: as of 2016, there were 11 long GRB—core-collapse supernovae associations. It was determined that neutrino-driven core-collapse explosions (which constitute the

majority of core-collapse explosions) have insufficient energy to generate long GRBs.

The stiffened nuclear equation of state describing the inner stellar core generally has $\Gamma > 5/3$, which is the value predicted for cold neutron star interiors (assuming $T = 0$ and that the interiors are composed of non-relativistic Fermi neutron and proton gases) (Ott, 2014). This means that neutron stars must be held up by more than the neutron and proton degeneracy pressures, otherwise ones above $0.7M_{\odot}$ could not exist. Indeed, neutron stars are also held up by the strong interactions which add another layer of difficulty to the problem of obtaining the correct nuclear equation of state. However, figuring out the nuclear equation of state (perhaps with the help of advanced ground-based gravitational-wave detectors) could narrow down the number of viable core-collapse supernovae mechanisms, a possibility that will be visited again and explained later in this section.

The Supernova Problem

The fundamental supernova problem is that Nature is very good at producing core-collapse supernovae, but we are not good at modeling them. Of the $\sim 3 \times 10^{53}$ erg of gravitational binding energy released through the formation of the final neutron star or black hole, only $\sim$1% ends up as kinetic and internal energy of the expanding ejecta. The remaining 99% is radiated away as neutrinos over hundreds of seconds as the proto-neutron star (the accreting inner core) cools (Bethe, 1990; Janka, 2001).

In 1966, Colgate and White (Colgate & White, 1966) were the first to suggest that neutrinos could play an important role in explosion, by depositing some of their energy into the rest of the star. In the present-day paradigm where core-collapse supernovae are indeed neutrino-driven (albeit much dif-

ferently than was originally proposed by Colgate and White), the crux of the supernova problem is that the shock from the inner core bounce becomes stalled. In other words, neutrinos from the electron captures become trapped by the infalling outer core which supplies a 'ram pressure' to the neutrinos, preventing them from getting out. Thus, any information about the bounce is unable to propagate out faster than it is being swept back in.

This problem was addressed by Wilson in 1985 who suggested that there can be delayed shocks due to net neutrino heating regions that develop behind the shock (Wilson, 1985). At matter densities near 3×10^{12} g cm^{-3}, the neutrino mean free paths decrease and the neutrinos become trapped due to the shortened time between consecutive neutrino reactions. The radii at which this occurs for each flavor of neutrino defines its respective neutrinosphere, i.e., the approximate 'surface' of the proto-neutron star (Mezzacappa et al., 2006) (Figure 1.1). Between the shock and the neutrinosphere, radially dependent heating and cooling determines the 'gain region' where neutrino opacities, i.e., neutrino-matter interactions favor the absorption of neutrinos and anti-neutrinos by protons and neutrons over their emissions (Bethe & Wilson, 1985):

$$\nu_e + n \rightarrow p + e^-$$

$$\bar{\nu}_e + p \rightarrow n + e^+$$

This energy deposition onto matter can deliver delayed (however, weak) explosions Bethe & Wilson (1985).

The next two milestones in contemporary supernova theory were discovered through computations. The first was the prediction that neutrino convection behind the shock can produce robust explosions with 2-dimensional (axisymmetric) models, whereas 1-dimensional (spherically symmetric) mod-

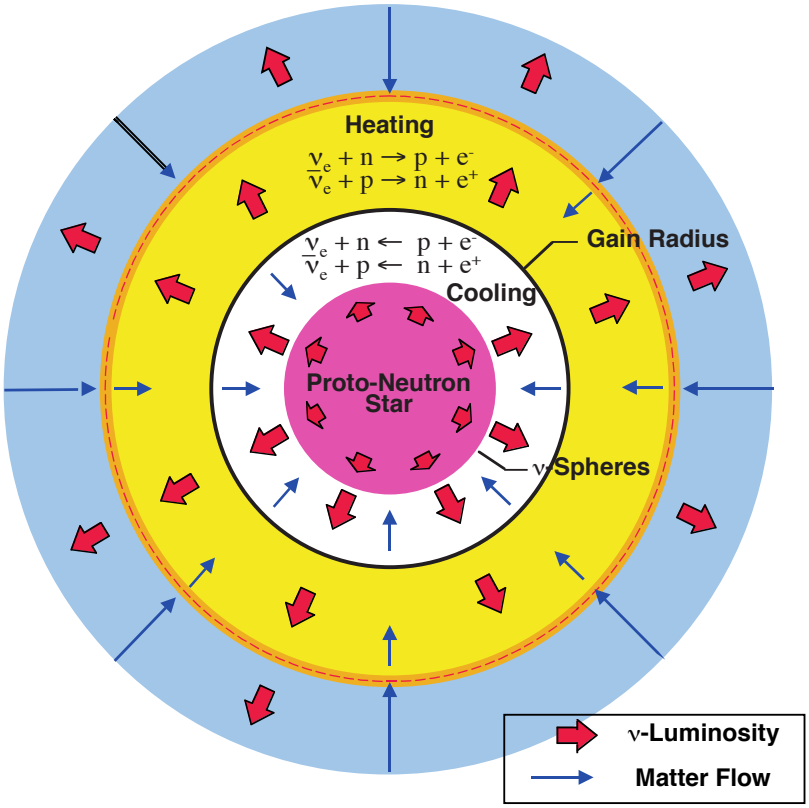

Figure 1.1: Net heating and cooling regions between the shock and proto-neutron star 'surface' which is defined by the neutrinospheres. (Figure from Mezzacappa et al., 2006)

els cannot (Herant et al., 1994). This suggests neutrino convection can play an important role in marginally explosive cases, and that the dimensionality of the modeling alone can make the difference in the production (or not) of the explosion.

The second computational prediction was of the standing accretion-shock instability (SASI) in 2003 (Blondin et al., 2003). Previously, researchers had studied the formation and the evolution of the shock but never its stability. The SASI prediction shows that non-radial perturbations to the shock are unstable and cause the shock to grow. However, radial perturbations are stable and cause the shock to ring back to where it was.

Therefore, to address the supernova problem realistically requires (1) a fully general relativistic treatment of gravity and its corrections to the neutrino transport equations (e.g., Bruenn et al., 2001; Liebendörfer et al., 2005), (2) net neutrino heating in the gain regions to overcome the infalling core's ram pressure (e.g., Wilson, 1985; Bethe & Wilson, 1985), (3) neutrino convection to better describe neutrino transport to the gain regions (Herant et al., 1994), (4) SASI which grows the shock upon non-radial disturbances (Blondin et al., 2003), and (5) other corrections from stellar rotations and the presence of magnetic fields, etc. to realistically model core-collapse supernovae. These state-of-the-art models have already been used to produce preliminary gravitational-wave waveforms to study their detection prospects by the advanced ground-based gravitational-wave detector network.

Detection Prospects

Less than 0.01% of the available $\sim 3 \times 10^{53}$ erg from core-collapse is radiated away via gravitational waves (Ott, 2009; Kotake, 2013). This strictly limits prospective sources for advanced ground-based gravitational-wave detectors to Galactic events up to 10 kpc away (Yakunin et al., 2017). However, much time and effort is dedicated to being ready for the next Galactic core-collapse supernova. This is because gravitational waves directly probe the central engine of the supernova, and particulars about the explosion dynamics can be extracted from gravitational-wave detections (e.g., Powell et al., 2016). Even more critically, this extracted information can also be used to validate differing core-collapse supernovae models.

The leading order contribution to gravitational waves is due to spherically asymmetric accelerations of mass and energy (Einstein, 1916, 1918). Thus, it is fitting that observations of electromagnetic emissions from core-

collapse supernovae (along with theory) predict strong asymmetries (Foglizzo et al., 2015). Then, it is possible to detect gravitational waves from neutrino convection and large-scale standing accretion-shock instabilities (SASI) for neutrino-driven core-collapse supernovae. (As a reminder, these were both historically predicted using 2-dimensional (spherically asymmetric) computer models (Herant et al., 1994; Blondin et al., 2003)).

The core-collapse supernova rate in the Milky Way and close-by Small and Large Magellanic Clouds is rather low, $\lesssim 1$ event per 30−50 years (Ott, 2009). However, the rate increases to ∼1 per 20 years if the entire local group of galaxies up to M31 at 0.8 Mpc is included (van den Bergh & Tammann, 1991). In general, a core-collapse event at 10 kpc (which is well within the Milky Way Galaxy), will produce gravitational-wave strains of amplitude $\sim 10^{-22}-10^{-21}$ with gravitational-wave energy outputs totaling $\sim 10^{-11}-10^{-10} M_{\odot} c^2$ (Murphy et al., 2009). This is more than enough for a detection by Advanced LIGO which at design sensitivity, is expected to detect Galactic events with minimum signal-to-noise ratios ∼10−20 (Harry & the LIGO Scientific Collaboration, 2010; Murphy et al., 2009).

Gravitational Wave Signatures

Gravitational wave signals were extracted from 2-dimensional and 3-dimensional hydrodynamic simulations using a weak-field, slow-motion formalism that considers strain contributions from the dominant mass-quadrupole moment only (Murphy et al., 2009; Yakunin et al., 2015; Nakamura et al., 2016). There are three key phases present in gravitational-wave emissions (Figure 1.2).

The first of the three phases is the prompt convection phase which lasts ∼70−80 ms after the core bounce. This is produced by Ledoux convec-

tion (Keil et al., 1996) in the proto-neutron star, which is due to a negative entropy gradient, $(\partial\rho/\partial \ln s)_{Y_l,P}$, or a negative (positive) lepton gradient, $(\partial\rho/\partial \ln Y_l)_{s,P}$ for large (small) lepton fractions, Y_l, below the neutrinosphere.

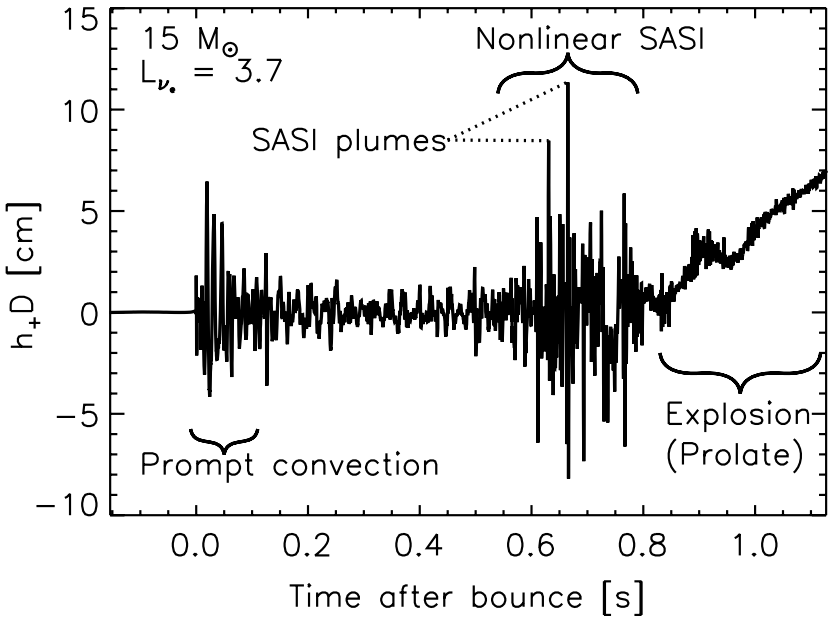

Figure 1.2: Sample gravitational-wave strain (h+) times the distance D vs. time after bounce. This signal was extracted from a 2-dimensional 15 $M_\odot$ simulation. (Figure from Murphy et al., 2009)

The second phase is the neutrino convection/SASI phase which starts around 120 ms for 15 $M_\odot$ 2-dimensional and 3-dimensional models (Murphy et al., 2009; Yakunin et al., 2017) and grows for about ∼550 ms past the bounce (Murphy et al., 2009). This is the strongest part of the gravitational-wave signal, as up to this point the shock is still quasi-spherical. The SASI in particular causes dense and narrow 'SASI plumes' that strike the proto-neutron star surface and correlate with large distinctive spikes in the gravitational-wave signal (Murphy et al., 2009; Marek & Janka, 2009) (Figure 1.2). In general, higher mass progenitors produce higher characteristic plume frequencies, f_p, which increase monotonically from ∼100 Hz at bounce to ∼300−400 Hz before explosion. Thus, although the gravitational-wave power declines between the

prompt convection phase and the SASI phase, the time-frequency spectrogram of the signal reveals the characteristic plumes and their increasing frequencies clearly (Figure 1.3) (Murphy et al., 2009).

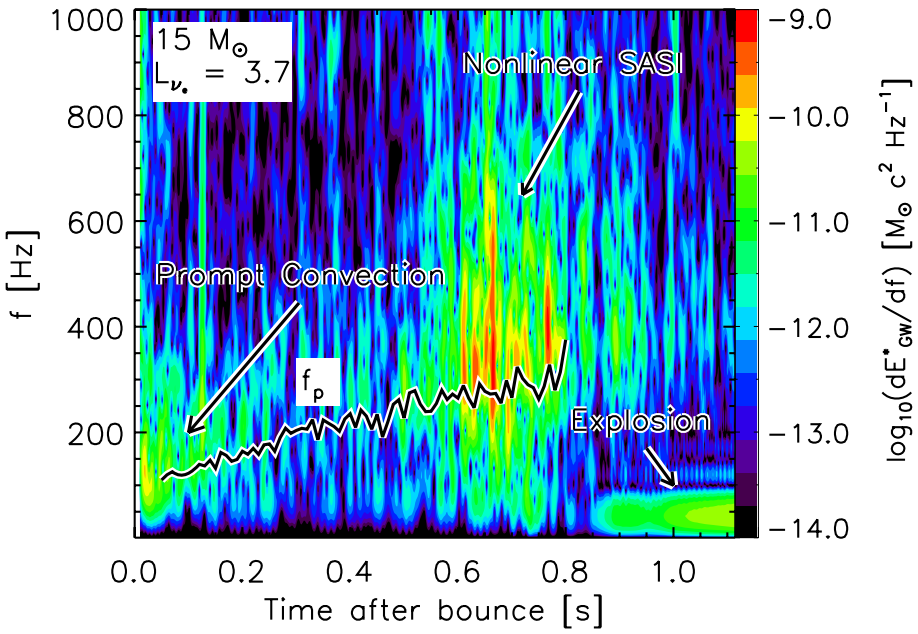

Figure 1.3: Comparisons of plume frequencies, f_p, with the gravitational-wave spectrogram. This signal was extracted from a 2-dimensional 15 $M_\odot$ simulation. (Figure from Murphy et al., 2009)

Comparisons of the gravitational-wave signals from the 2-dimensional and 3-dimensional cases show that the SASI phase is strong in 2 dimensions, although strong signal components below 250 Hz are still present in the 3-dimensional cases (Andresen et al., 2017). On the other hand, gravitational-wave signals from neutrino convection are stronger in 3-dimensional models than in 2, although their overall contribution to the gravitational-wave signal is less prominent.

The third and last phase is the explosion phase, which has a 'memory' feature originating from the outer exploding regions of the star, i.e., there are distinct differences in the gravitational-wave signal that reveal the general morphology of the explosion (i.e., prolate, oblate, and spherical) (Murphy

et al., 2009). As expected, when the explosion is spherical, there is very little gravitational radiation and the strain drops to 0. However, a prolate explosion results in a rise in strain that is specifically positive (in the reference frame of the star where the explosion would be seen as prolate) vs. an oblate explosion whose strain will become negative.

The explosions are also much lower in frequency, ∼tens of Hz (Figure 1.3). In many of the 3-dimensional simulations, the models did not run long enough to produce explosions[2]. However, it is expected that the 3-dimensional gravitational-wave signal will be smaller in amplitude than the 2-dimensional case due to a smaller mass fraction contained inside the shock wave (Lentz et al., 2015).

One critical point in this section is that 2-dimensional models by necessity admit only one polarization state of the gravitational waves, +, due to their axisymmetry. Therefore, realistic core-collapse supernovae which are more likely to be similar to the 3-dimensional case will have increased chances of detection due to both + and × polarizations being available for detection.

Electromagnetic/Neutrino Signatures

Neutrinos compose nearly 99% of the energy released in a core-collapse supernova. Thus, recent 3-dimensional core-collapse simulations of non-rotating progenitors with neutrino transport looked for correlations between the resultant neutrino and gravitational-wave signals (Kuroda et al., 2017). These models show that strong correlations between the two signals are characteristic of vigorous SASI activity in the supernova core.

On the electromagnetic signature side, main classes and subclasses of

[2]Simulations take millions of processing hours to complete, which convert into months when running on thousands of computing cores (Messer et al., 2013).

supernovae are determined by their spectral properties. The two main classes of supernovae are Type I and Type II, established by the absence or presence of hydrogen lines in the peak optical spectrum (Minkowski, 1941). Subclasses of Type I exist to distinguish between supernovae with or without silicon or helium lines. Of the different classes of supernovae in Table 1.1, we focus on those with a core-collapse[3] explosion mechanism only (Types Ib, Ic, and II). In reality, there is a continuum among the core-collapse supernovae classes depending on the amount of hydrogen and helium lost from the outer envelopes before the explosion (due to stellar winds) and of that, how much is retained after the explosion. This results in differences among the supernovae light curves that leads to further refinement of classification.

	H	**He**	**Si**	**Mechanism**	**Subclassification**
Type I			✓	thermonuclear	Type Ia
Type I		✓		core-collapse	Type Ib
Type I				core-collapse	Type Ic
Type II	✓			core-collapse	Type II

Table 1.1: Supernova classification depends on the absence or presence (marked by ✓) of hydrogen (H), helium (He), or silicon (Si) lines in the peak optical spectra.

Type II supernovae are typically observed in the spiral arms of spiral galaxies with Population I[4] stars as progenitors. They have characteristic Balmer lines in their peak optical spectra. Among Type II supernovae, those with thicker retained hydrogen envelopes have light curves with a long plateau phase (Type IIP) in contrast to those with thinner hydrogen envelopes retained whose light curves decline more quickly (Type IIL). Progenitors of Type IIL supernovae are also expected to have larger radii than Type IIP in order to

[3]Type Ia supernovae are produced by accreting white dwarfs in close binaries where the silicon lines are thought to come from runaway carbon fusion in the white dwarf core.

[4]Population I stars are young, high-metallicity stars, formed from the gas of previous generation stars.

explain their higher peak luminosities (Hicken et al., 2017).

Type IIb supernovae are a class between Type II and Type Ib, where a few tenths of a solar mass of the original hydrogen envelope was retained. Thus, Balmer lines that appear in the early spectra quickly disappear as the supernova ages, and are replaced with strong helium lines. This suggests retreat of the supernova photosphere through the hydrogen envelope and into the helium layer. Progenitors of Type IIb supernovae are in the $10-18\ M_{\odot}$ range and are likely to be in binary systems.

Type IIn supernovae have distinct narrow hydrogen and helium emission lines which indicate the presence of a dense circumstellar medium (CSM). There is considerable heterogeneity in this supernova class, with some supernovae featuring a strong Hα line[5] while in others it is noticeably faint, and some supernovae evolving into strong radio and X-ray sources while others do not.

Type Ib and Ic supernovae have only been observed in spiral galaxies near sites of recent star formation (i.e., H II regions[6]). Furthermore, Type Ib and Ic supernovae fall into the category of stripped-envelope supernovae where Type Ib progenitors have lost their hydrogen envelope and Type Ic progenitors have additionally lost their helium envelope. These two clues suggest progenitors of Type Ib/Ic supernovae are Wolf-Rayet stars (i.e., stars with mass $\gtrsim 25\ M_{\odot}$).

In particular, Type Ic progenitors (especially those born with sub-solar metallicity) are interesting because they are associated with the majority of observed long-duration gamma-ray bursts (long GRBs), which are intense beamed signals of gamma-rays with durations lasting $2-100$ s ($>$ 10,000 s

[5]The Hα line is the first of the Balmer lines, meaning it occurs when a hydrogen electron falls from its n=3 to n=2 energy level, corresponding to a wavelength of 656.28 nm.

[6]H II regions are regions of ionized interstellar atomic hydrogen, commonly found in spiral galaxy disks.

in the case of ultra-long GRBs). It is also likely that these long GRB progenitors are rapidly rotating, which would consequently alter the observed GW signal from the associated core-collapse supernova. However, it remains unclear whether rapidly rotating Wolf-Rayet stars exist, although some models suggest surface rotation velocities of ∼200 km/s (Shenar et al., 2014). Thus, there are low-latency searches in place by advanced ground-based interferometric GW detectors to look for coincidences between unmodeled transient gravitational-wave signals and GRBs/neutrinos (Section 8.1).

Lastly, supernovae leave behind spectacular supernovae remnants which can be observed for hundreds to thousands of years after the explosion. These remnants are created by the surrounding interstellar medium which is violently compressed and chemically enriched by the gaseous shell ejected from the supernova.

It is now more than 80 years since Baade and Zwicky proposed that neutron stars are formed in core-collapse supernovae (Baade & Zwicky, 1934). They were correct, although the exact internal mechanism still eludes us. The advanced ground-based gravitational-wave detectors will allow us to directly probe the supernova central engine at design sensitivities. Thus, an end is in sight to the 50+ year old supernova problem, likely with the help of gravitational-wave astronomy.

1.2 Magnetars

Magnetars are a special class of neutron stars that were originally identified by their ultra-strong magnetic fields, in excess of the quantum critical field[7], $B_{\rm QED} = \frac{m_e^2 c^3}{\hbar e} = 4.4 \times 10^{13}$ G (Kouveliotou, 1999). In present-day magne-

[7]This is the value of the magnetic field at which the cyclotron energy (the energy between Landau levels of electrons) equals the rest-mass energy for an electron (Duncan & Thompson, 1992; Mereghetti, 2008).

tar physics, they are more generally defined as neutron stars with magnetically-powered emissions, regardless of their measured or inferred surface dipole fields (Turolla et al., 2011; Rea et al., 2012; Rea et al., 2014), and regardless of being powered in-part by rotation (Kumar & Safi-Harb, 2008). They are further characterized by slow X-ray pulsations (periods $P \sim 2{-}12$ s) and large spin-down rates (period derivatives $\dot{P} \sim 10^{-10}{-}10^{-12}$ s s^{-1}) (Rea et al., 2008).

Magnetars were proposed in 1992 to explain in a unified way, two observationally distinct classes of objects known by then (Duncan & Thompson, 1992): soft gamma repeaters (SGRs) and anomalous X-ray pulsars (AXPs), which were discovered in 1979 (Mazets et al., 1979a,b; Mazets & Golenetskii, 1981) and 1981 (Fahlman & Gregory, 1981) respectively.

As of 2014, there were 21 confirmed magnetars and 5 magnetar candidates, with thousands of them expected to exist in our Galaxy (Olausen & Kaspi, 2014; Negreiros et al., 2018). Of the confirmed magnetars, SGR 0418+5729, Swift J1822.3−1606, and 3XMM J185246.6+003317 are the lowest magnetic field magnetars, with inferred surface dipole fields of magnitude $B_{\rm p} <\sim 7.5 \times 10^{12}$ G, 2.7×10^{13} G, and 4.1×10^{13} G (Turolla et al., 2011; Rea et al., 2012; Rea et al., 2014), all less than $B_{\rm QED}$. These lower magnetic field magnetars are aged magnetars with rapidly decaying magnetic fields. SGR 0418+5729 and Swift J1822.3−1606 are estimated to be ∼1 Myr and ∼550 kyr old.

A central question regarding magnetars is, "What is the origin of the high magnetic fields observed in magnetars?" In particular, the magnetic field strength impacts the structure and evolution of neutron stars on three different fronts: microscopically by altering the equation of state through Landau quantization which leads to pressure anisotropies that affect particle composition,

macroscopically by requiring a full axially symmetric (rather than spherically symmetric (Oppenheimer & Snyder, 1939)) treatment of perfect fluids within the General Theory of Relativity framework that changes the mass/radii of neutron stars, and temporally by altering the spin-down properties (P and $\dot{P}$) which can mask the true age of the neutron star if the field exhibits non-canonical behavior. So far, we understand that magnetar magnetospheres are made up of twisted magnetic field lines both inside and outside of the star as shown in Figure 1.4, which can explain their characteristic persistent emissions and X-ray spectral shapes (Subsection 1.2) (Thompson & Duncan, 2001; Thompson et al., 2002).

Furthermore, the study of magnetar subpopulations and their thermal evolution is important to understanding physical conditions that lead to the formation of different types of young, isolated neutron stars (Ertan et al., 2014): AXPs, SGRs, dim isolated neutron stars (XDINs), central compact objects (CCOs), and rotating radio transients (RRATs). Past population synthesis studies suggest that up to ∼10% of neutron stars are expected to have companions (Iben & Tutukov, 1996), thus another lingering astrophysical question regarding magnetars is, "Why are all the known magnetars isolated?" (Popov & Prokhorov, 2006). In the case of AXPs, they were dubbed "anomalous" because their high X-ray luminosities could not be explained by accretion from a binary companion or from rotational energy loss, $\dot{E}$, as in the case of standard pulsars.

Electromagnetic/Neutrino Signatures

Nearly 10% of all core-collapse supernovae explosions (Section 1.1) result in magnetars, manifesting themselves as either SGRs or AXPs (which could be a later phase in the evolution of SGRs) (Kouveliotou, 1999). In 1986,

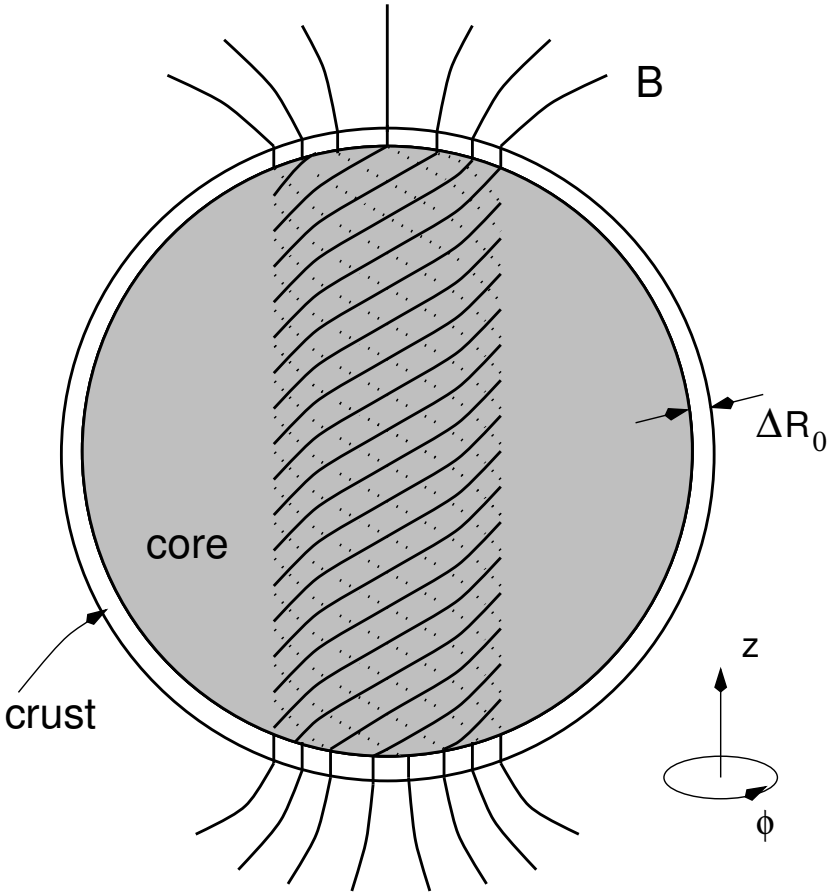

Figure 1.4: Schematic diagram of magnetar magnetic field lines. Uniform poloidal field lines thread the liquid core and the solid, outer crust of the star while toroidal field lines are created by twisted field lines inside the core. (Figure from Thompson & Duncan, 2001)

SGRs were recognized as a class of objects separate from GRBs, with the most important difference being the recurrence of SGR events. This excluded the possibility of SGRs having the same progenitors as GRBs, which were (correctly) conjectured at the time to be caused by the catastrophic destruction of their parent object population. Indeed, the best current model of SGR and AXP events suggests they are glitches and flares caused by stresses built up in the magnetar crust due to internal toroidal fields, B_ϕ, that are twisted up to 10 times more than the external dipole fields. This induces a rotation of the surface neutron star layers that deforms the crust and leads to fractures (i.e.,

starquakes), outbursts, and flares.

There have been 3 types of magnetar bursting events detected thus far: short bursts, intermediate bursts, and giant flares (Turolla et al., 2015). Short bursts are the most common and observed in both SGRs and AXPs. They typically last 0.1−1 s and have peak luminosities $10^{39}-10^{41}$ erg/s with soft (∼10 keV) thermal spectra. Intermediate bursts are also observed in both SGRs and AXPs but last longer (1−40 s) and have more energetic peak luminosities ($10^{41}-10^{43}$ erg/s). Finally, there are also giant flares which have been observed only 3 times since SGRs were discovered: from SGR 0526−66 in 1979 (Mazets et al., 1979a), SGR 1900+14 in 1998 (Hurley et al., 1999), and SGR 1806−20 in 2004 (Hurley et al., 2005; Palmer et al., 2005). These rare events are characterized by peak luminosities in the range $10^{44}-10^{47}$ erg/s. As observed from Earth, giant flares could appear as short gamma-ray bursts (sGRBs) (Section 1.3) if emitted by extragalactic SGRs (Palmer et al., 2005; Hurley et al., 2005). Upper limits on the fraction of sGRBs due to these events are ∼1−15% (Hurley, 2011).

Magnetars also have persistent (non-bursting), often variable X-ray luminosities in the range $10^{33}-10^{36}$ erg/s. The low-energy thermal component of these emissions can be fit with one blackbody spectrum of temperature ∼0.3−0.6 keV and a power law with a steep photon index $\Gamma \sim 2-4$, or by two blackbody spectra of temperatures ∼0.3 keV and ∼0.7 keV (Rea et al., 2008). On top of this, there are also non-thermal emissions caused by charged particles trapped in the twisted magnetic field lines (Figure 1.4) that interact with the surface X-ray thermal emissions through resonant cyclotron scattering (Thompson et al., 2002). While soft X-ray emissions (below 10 keV) can be explained by resonant cyclotron scattering, hard X-ray emissions (above ∼20 keV) remain poorly understood. It is suspected that either thermal

bremsstrahlung from magnetar surface layers heated by returning currents or synchrotron emissions from pair creation in the upper magnetosphere ($\sim$100 km) are responsible for these hard emissions (Thompson & Beloborodov, 2005).

Although more than 90% of magnetar bolometric luminosities are concentrated in the 1$-$200 keV range, there are still faint ($K \sim 20$) optical and/or NIR counterparts (Israel et al., 2004) that are sometimes pulsed and transient. As of 2003, there were four IR-identified counterparts to AXPs: 4U 0142+61 (Hulleman et al., 2000), 1E 2259+586 (Kaspi et al., 2003), 1E 1048.1$-$5937 (Israel et al., 2002), and 1RXS J170849$-$400910 (Israel et al., 2003).

Magnetar radio emissions remain controversial. In the past, it was assumed they would be absent due to photon splitting, a quantum electrodynamical effect which kicks in for $B > B_{\rm QED}$, and can overtake electron-positron pair production deemed essential for pulsar radio emissions (Baring & Harding, 1998). However, as observed in AXP XTE J1810$-$197, magnetars can also emit radio pulses after an outburst (Camilo et al., 2006; Camilo et al., 2007). These emissions differ from standard radio pulsar emissions (Subsection 2.4) in that their spectrum is flatter and both the flux and pulse profile show strong variations with time. This indicates either the emission mechanism or emission region topology differs between standard radio pulsars and magnetars.

Lastly, newborn magnetars could emit neutrinos during the $\sim$10$-$100 s cooling epoch following core-collapse (Murase et al., 2014). These emissions would be generated by a relativistic nucleon-rich wind where the neutrons eventually undergo inelastic collisions, producing neutrinos in the energy range $\sim$0.1$-$1 GeV.

Gravitational Wave Signatures

Two types of gravitational-wave emissions are expected from magnetars. The first are short bursts of gravitational waves which could be generated in the event of a starquake. In the most energetic case where giant flares erupt, there could be up to $\sim 10^{49}$ erg emitted in the form of gravitational waves (Corsi & Owen, 2011). These upper limits are calculated from models where the internal toroidal field lines of the magnetars become reconfigured during the starquake, changing the shape of the star, causing a sudden fractional jump in the moment of inertia, $\Delta\mathcal{I}/\mathcal{I} \sim 10^{-4}$. A change in the moment of inertia of this magnitude was observed in the giant flare event of SGR 1900+14 in 1998.

The second main type of gravitational-wave emission is continuous and caused by rotation of a deformed body around one of its principal axes. Advanced ground-based interferometric detectors can detect gravitational waves from newborn magnetars up to ~20 Mpc away if they have internal toroidal fields $B_\phi \gtrsim 10^{16}$ G, especially if dipole fields $B_\mathrm{p} <$ a few 10^{14} G and initial spin periods $P_i \sim$ a few ms (Kashiyama et al., 2016). Strong toroidal fields make the star more prolate and triaxial so that in general, the principal moments of inertia, $I_1 \neq I_2 \neq I_3$. Then, the deformation can be described in terms of an ellipticity parameter, ϵ:

$$\epsilon = \frac{I_1 - I_2}{I_3},$$

and the gravitational-wave amplitude is proportional to $I_1 - I_2 = \epsilon I_3$. In the special case that $I_1 = I_2 \neq I_3$ is symmetric about the axis of rotation, no gravitational waves are generated. Lastly, a population of rotating, deformed magnetars could contribute to an overall stochastic gravitational-wave background (Marassi et al., 2011).

1.3 Compact Binary Coalescences

The three endpoints of stellar evolution are white dwarfs, neutron stars, and stellar mass black holes, listed in order of increasing compactness, dependent on the mass of the progenitor star. Binary systems of compact objects (herein defined as neutron stars and stellar mass black holes) such as two neutron stars or two stellar mass black holes orbiting around their common center of mass have already been observed to emit gravitational waves. There has been indirect observation in the case of binary pulsars with time-changing orbits that are consistent with gravitational wave emission (see Section 2.4 for the Hulse-Taylor binary, the first of such systems to be discovered), and direct observation in the case of all confident mergers listed in *GWTC-1: A Gravitational-Wave Transient Catalog of Compact Binary Mergers Observed by LIGO and Virgo during the First and Second Observing Runs* (Abbott et al., 2018). Because orbital decay is a direct consequence of gravitational-wave emission, compact objects in these systems eventually inspiral and merge. During the inspiral phase, gravitational waves are emitted in a highly predictable manner that can be modeled using various techniques depending on the masses and compactness of the system involved. Eventually, these objects reach their final few cycles before merger, which occurs in the sensitivity band of advanced ground-based interferometric gravitational-wave detectors. For BNS systems (and low-mass BBH systems to a lesser extent), there can be up to hundreds and thousands of cycles observed in the Advanced LIGO and Virgo sensitivity band.

During these last few cycles, it becomes more and more difficult to model the gravitational-wave emission, especially when neutron stars make up one or both of the compact objects. Compact systems involving two neutron stars always tidally disrupt whereas neutron star-black hole binaries might or might

not (depending on the mass ratio and spin of the two objects). When tidal disruption does occur, there are opportunities for multi-messenger observations. In the case of binary stellar mass black hole systems, multi-messenger observations are less likely, although not impossible.

Because compact binary coalescences are by far the most common class of objects detectable by advanced ground-based interferometric detectors, there is an entire section devoted to waveforms and searches for these events (see Section 4.1). Here, we will explore various observing scenarios for joint gravitational wave, electromagnetic, and neutrino emissions from compact binary coalescences.

Progenitors

Here, we focus on compact binary coalescences involving only neutron stars and black holes, which are sources of gravitational waves in the Advanced LIGO and Virgo sensitivity bands. Therefore, systems of interest are binary neutron stars (BNS), neutron star-black holes (NS-BH), and binary black holes (BBH).

As an aside, binary white dwarfs (known as double white dwarfs, DWD) also emit gravitational waves, albeit in the sensitivity band of space-based interferometric gravitational-wave detectors (0.1 mHz to 100 mHz) (Sathyaprakash & Schutz, 2009). These systems involve complex mass transfer between the donor stars and accretors that could result in the systems becoming AM Canum Venaticorum variable stars (Nather et al., 1981; Tutukov & Yungelson, 1996) or Type Ia supernovae (e.g., Iben & Tutukov (1984); Webbink (1984)). Thus, DWD systems are also multi-messenger sources that will detected with the advent of LISA, the Laser Interferometer Space Antenna, the space-based interferometric gravitational-wave detector in the works.

Stellar Mass Black Hole Binaries

It is possible for stellar mass binary black hole (BBH) systems to have electromagnetic/neutrino counterparts under more exotic circumstances (Ford et al., 2019). In particular, either disks formed around the remnant black hole with sufficient mass accretion at late times of the merger will be required, or dense gaseous environments in order to produce strong electromagnetic and/or neutrino emissions. The latter case is likely to arise in Active Galactic Nuclei (AGN), where stellar mass black holes will congregate towards the accretion disk of the supermassive black hole and merge quickly, with mini-accretion disks formed around the inspiraling black holes that can power relativistic outflows.

Neutron Star Binaries

So far, there has been one confirmed observation of a BNS merger by the Advanced LIGO and Virgo gravitational-wave detectors, GW170817 (Abbott et al., 2017). Discovery of its electromagnetic counterparts, a short gamma-ray burst, GRB 170817A, and optical transient, SSS17a/AT 2017gfo, has led to separate insights about the progenitor of GW170817.

The optical transient, SSS17a/AT 2017gfo, was first identified by Swope in a nearby ($\sim$40 Mpc) host galaxy, NGC 4993, less than 11 hours after the time of the neutron star merger. This identification estimated the event to take place at a projected distance of $\sim$2 kpc from the galaxy's center, giving us the first kinematic constraints on the progenitor system's natal (supernova) kicks and size of the pre-supernova semi-major axes of the system (Abbott et al., 2017b). Thus, progenitor models of the BNS system (starting at the time of the second supernova, with various pre- and post- second supernova properties) were evolved forward in time in the context of a model of the host

galaxy, and then narrowed down to those systems that became GW170817-like, by using the physical location of the observed electromagnetic counterpart and the gravitational-wave inspiral time/frequency as a veto. In the case of NGC 4993, an early-type spheroidal galaxy with few globular clusters (250^{+750}_{-150}), the progenitor of GW170817 likely evolved as an isolated binary in the galaxy's field population over $\gtrsim 1$ Gyr before merger.

Prior to observations of GW170817 and its short gamma-ray burst (sGRB) counterpart, sGRBs (at least those produced by neutron star binaries) were thought to be powered by collimated, relativistic jets produced during rapid accretion onto disks formed around the remnant final object—usually a black hole—at late times of the merger. However, GW170817 showed that these jets are not as sharply collimated as previously assumed. In general, these electromagnetic counterparts are only observable by viewers within the half-opening angle of the jets.

Observations of the short gamma-ray burst, GRB 170817A, by *Fermi*/GBM and *INTEGRAL*/SPI-ACS (Goldstein et al., 2017; Savchenko et al., 2017), confirm for the first time that at least of a fraction of short gamma-ray bursts (whose origins have long been debated) are due to BNS mergers, providing insight into the energetics and phenomenology of the progenitor system's final moments. Before GW170817/GRB 170817A, clues about the origin of short gamma-ray bursts were given: the first afterglow detections in May to July 2005 of GRBs 050509b (Gehrels et al., 2004, 2005), 050709 (Villasenor et al., 2005; Fox et al., 2005; Hjorth et al., 2005), and 050724 (Barthelmy et al., 2005; Berger et al., 2005), revealed that short gamma-ray bursts are not associated with core-collapse of massive stars (as in the case of long gamma-ray bursts), occur at cosmological distances in both elliptical and star-forming galaxies, and have afterglows with lower energy and density scales than long gamma-

ray bursts.

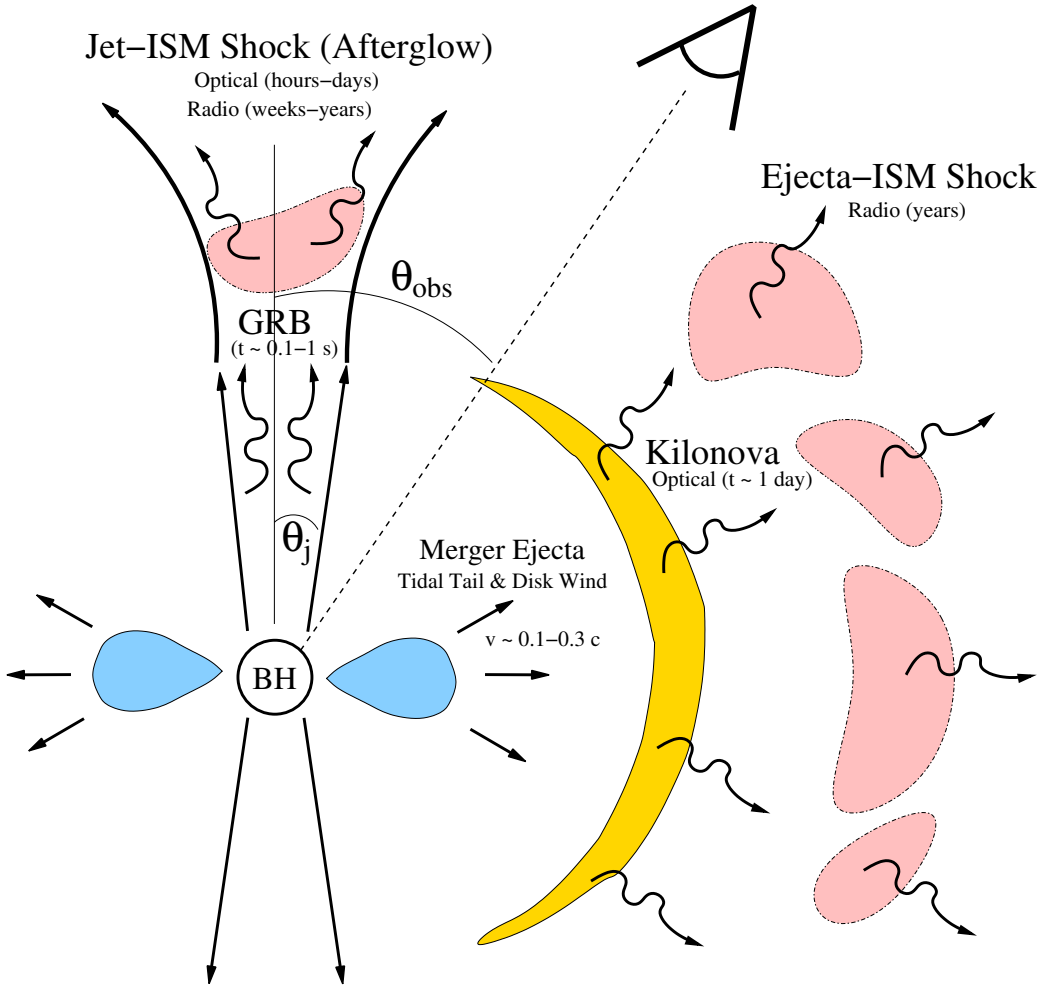

Figure 1.5: Possible electromagnetic counterparts to neutron star binaries. In blue is the cross section of the centrifugally supported disk around the final black hole, in red is the surrounding circumburst medium, and in yellow is the more isotropic kilonova. (Figure from Metzger & Berger, 2012)

Thus, the most probable electromagnetic counterparts to a binary neutron star coalescence are the kilonova emission and the kilonova precursor. During the neutron star merger, a small amount of neutron rich matter is ejected both dynamically from the neutron star(s) being torn apart and from remnant disk outflows if a disk is created. The neutrons are then captured for r-process nucleosynthesis (including Lanthanide production) and radioactively decay for days to weeks long, producing the isotropic kilonova (Li &

Paczyński, 1998). However, a small fraction ($\sim 1 \times 10^{-4} M_{\odot}$) escapes being captured through r-process and instead undergoes β-decay, producing the kilonova precursor which occurs a few hours after the merger (Metzger et al., 2015).

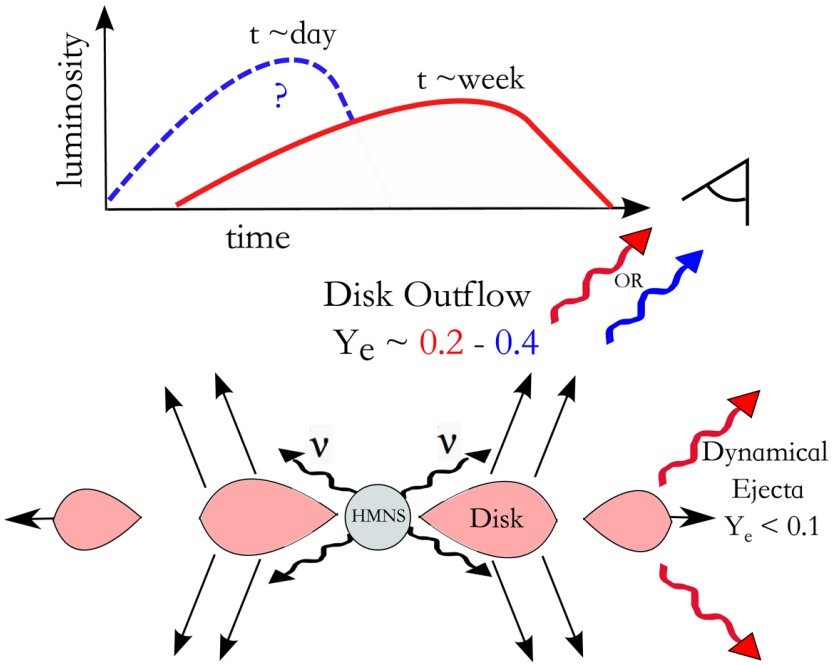

Figure 1.6: A possible blue bump in the observed kilonova emission could be indicative of a long-lived hypermassive neutron star phase where the electron fraction is raised to a high enough value ($Y_e \sim 0.4$) that no Lanthanides are produced. On the other hand, if the remnant black hole is formed promptly after the merger, both the dynamical ejecta before the merger and disk outflows after the merger will be highly neutron rich ($Y_e < 0.1$) generating a kilonova emission that peaks later and in the near-infrared. (Figure from Metzger & Fernández, 2014)

Both the kilonova and the kilonova precursor are important counterparts because they can encode information to discern the nature of the progenitor, i.e., confirm whether it is a binary neutron star or neutron star-black hole merger, or whether the merger went through a brief period where a hypermassive neutron star (HMNS) was created before collapsing into the remnant black hole (Metzger & Fernández, 2014). For instance, the ∼week long kilonova emission with a spectral peak in the near-infrared (NIR) could be indica-

tive of prompt ($\lesssim$ 100 ms) remnant black hole creation and the production of Lanthanides whereas a shorter-lived ∼day long emission with a bluer optical peak before the late NIR peak could be indicative of a HMNS phase with Lanthanide-free outflows (Figure 1.6).

Constraining the Nuclear Equation of State

Both core-collapse supernovae and neutron star mergers (Section 1.3) involve the same rich physics: they both require general relativity, the strong and weak interactions, fluid and magnetohydrodynamics, and transport theory. One way a neutron star merger detection could aid the supernova theorists is by narrowing down the correct nuclear equation of state from a number of contenders.

The equation of state strongly determines the stiffness of the inner core and the species of nuclides at the time of bounce (Togashi et al., 2017), which ultimately affects the final mass of the proto-neutron star. This is turn determines the amount and rate at which neutrinos revive the shock wave. In general, studies have shown that increasing the proto-neutron star mass increases the average neutrino luminosity and energy, as well as the evolutionary timescale (Pons et al., 1999).

To date, the two most massive neutron stars were observed in binary pulsar systems. They reveal masses of $1.97 \pm 0.04\ M_{\odot}$ from PSR J1614−2230 (Demorest et al., 2010) and $2.01 \pm 0.04\ M_{\odot}$ from PSR J0348+0432 (Antoniadis et al., 2013). These two masses put constraints on the viable mass-radius curves from different equations of state in the neutron star mass vs. radius parameter space. In particular, they rule out a large range of soft hadronic, mixed hadronic-exotic, and strange-quark matter equations of state (Lattimer & Prakash, 2011; Özel et al., 2010).

As of yet, there have not been any robust neutron star radius (or mass plus radius) measurements to further constrain the parameter space (Lattimer, 2012; Miller, 2013; Miller & Lamb, 2016). However, radius measurements could be determined by gravitational-wave detections. For instance, the combination of gravitational-wave and electromagnetic data from GW170817 and its kilonova has already led to the binary's neutron star radii estimates (Abbott et al., 2018). It is also possible that signals from binary neutron star mergers (Subsection 1.3), specifically the peak frequency of the post-merger emission, could reveal the neutron star radius in the case of symmetric mass binaries (Bauswein & Janka, 2012). For neutron star-black hole mergers, tidal deformation and neutron star disruption could reveal the neutron star radius as well (Lattimer, 2012).

Chapter 2

Gravitational Waves

2.1 General Theory of Relativity in a Nutshell

In the opening chapter of the book *Gravitation* (Misner et al., 1973), Einstein's geometric view of gravity is summarized in two sentences: "Space acts on matter, telling it how to move. In turn, matter reacts back on space, telling it how to curve."

Mathematically, the first statement, "Space acts on matter...", is known as the geodesic equation and can be written as:

$$\frac{d^2x^\rho}{d\lambda^2} + \Gamma^\rho_{\mu\nu}\frac{dx^\mu}{d\lambda}\frac{dx^\nu}{d\lambda} = 0.$$

It is the statement that objects free of all forces, move in straight lines locally.

The second statement, "In turn, matter reacts back on space..." , is known as Einstein's field equations[1] and can be written as:

$$R_{\mu\nu} - \frac{1}{2}g_{\mu\nu}R = \frac{8\pi G}{c^4}T_{\mu\nu}.$$

Now, there are a lot of scary looking symbols in both equations above but most of them can ultimately be written in terms of the key players: space-time (time as x^0 or t plus three spatial coordinates x^1, x^2, x^3, or x^i) and mass/energy. The symbols that cannot be reduced to these are Newton's gravitational constant (G) and the speed of light in vacuum (c).

[1] There are 6 truly independent equations in Einstein's field equations: 10 independent equations from equating symmetric rank (0,2) tensors minus 4 constraints on $R_{\mu\nu}$ from the Bianchi identity.

When we calculate the differential separation between two points in space-time, we use the line element:

$$ds^2 = g_{\mu\nu} dx^\mu dx^\nu,$$

which gives us the metric tensor[2], $g_{\mu\nu}$. It has a related inverse metric, $g^{\mu\nu}$, such that

$$g^{\mu\nu} g_{\nu\rho} = g_{\rho\nu} g^{\nu\mu} = \delta^\mu_\rho = \begin{cases} 1 \text{ when } \mu = \rho \\ \\ 0 \text{ when } \mu \neq \rho \end{cases},$$

where the Einstein summation convention[3] is used. The inverse metric and metric come in handy when raising and lowering indices of a given tensor.

Fundamental quantities can be computed using the metric tensor. For example, the proper time of an object following a time-like path, τ, is:

$$\Delta\tau = \int \sqrt{-g_{\mu\nu} \frac{dx^\mu}{d\lambda} \frac{dx^\nu}{d\lambda}} d\lambda,$$

where λ is any affine parameter, i.e., it satisfies $\lambda = a\tau + b$ for some constants a and b.

The Christoffel symbols[4], $\Gamma^\rho_{\mu\nu}$, which appear in the geodesic equation are

[2] A rank (k, l) tensor is a real-valued, linear function of k vectors and l dual vectors.

[3] In the Einstein summation convention, repeated upper and lower indices are summed over. Greek letters include both spatial and temporal coordinates while Latin letters (excluding t for time) include only spatial coordinates.

[4] Christoffel symbols allow us to correctly switch between coordinate systems when describing physical objects and their rates of change. Fundamentally, all physical quantities and laws must take a geometric form, i.e., one that is free of any coordinate system or basis vectors. Thus, a vector $\vec{V}$, for example, can be expressed in one coordinate system with components V^α and basis vectors $\hat{e}_\alpha$ or equivalently, in another coordinate system with components V^β and basis vectors $\hat{e}_\beta$. Its derivative has the relation:

$$\frac{\partial \vec{V}}{\partial x^\beta} = \frac{\partial V^\alpha}{\partial x^\beta} \hat{e}_\alpha + V^\alpha \frac{\partial \hat{e}_\alpha}{\partial x^\beta},$$

where in the last term, $\partial \hat{e}_\alpha / \partial x^\beta$ is itself a vector that can be written as a linear combination of basis vectors:

$$\frac{\partial \hat{e}_\alpha}{\partial x^\beta} = \Gamma^\mu{}_{\alpha\beta} \hat{e}_\mu.$$

Then, a little substitution and renaming indices gives us an important result, the covariant

defined as:

$$\Gamma^{\rho}_{\mu\nu} = \frac{1}{2} g^{\rho\sigma} (\partial_\mu g_{\nu\sigma} + \partial_\nu g_{\sigma\mu} - \partial_\sigma g_{\mu\nu}),$$

where ∂_μ is shorthand for:

$$\partial_\mu = \frac{\partial}{\partial x^\mu} = \left(\frac{1}{c} \partial_t, \partial_i \right).$$

Thus, we have so far understood all of the symbols that appear in the first statement, "Space acts on matter, telling it how to move" via the geodesic equation.

In the Einstein field equations, the two symbols $R_{\mu\nu}$ and R that appear are related to the Christoffel symbol via the Riemann tensor:

$$R^{\mu}{}_{\nu\rho\sigma} = \partial_\rho \Gamma^{\mu}_{\nu\sigma} - \partial_\sigma \Gamma^{\mu}_{\nu\rho} + \Gamma^{\mu}_{\alpha\rho} \Gamma^{\alpha}_{\nu\sigma} - \Gamma^{\mu}_{\alpha\sigma} \Gamma^{\alpha}_{\nu\rho},$$

which gives a local description of space-time curvature at each point. It gives us the change δV^μ in the vector V^μ, if we move it around a closed loop via parallel transport[5] first along $\delta a\ \hat{e}_\sigma$, then $\delta b\ \hat{e}_\rho$, then $-\delta a\ \hat{e}_\sigma$, and $-\delta b\ \hat{e}_\rho$:

$$\delta V^\mu = \delta a\ \delta b\ R^{\mu}{}_{\nu\rho\sigma} V^\nu.$$

Then, the Ricci tensor, $R_{\mu\nu}$, is just a contraction of the first and third indices:

$$R_{\mu\nu} = R^{\alpha}{}_{\mu\alpha\nu},$$

---

derivative:

$$\begin{aligned}
\frac{\partial \vec{V}}{\partial x^\beta} &= \frac{\partial V^\alpha}{\partial x^\beta} \hat{e}_\alpha + V^\alpha \frac{\partial \hat{e}_\alpha}{\partial x^\beta} \\
&= \frac{\partial V^\alpha}{\partial x^\beta} \hat{e}_\alpha + V^\alpha \Gamma^{\mu}{}_{\alpha\beta} \hat{e}_\mu \\
&= \frac{\partial V^\alpha}{\partial x^\beta} \hat{e}_\alpha + V^\mu \Gamma^{\alpha}{}_{\mu\beta} \hat{e}_\alpha \\
&= \left(\frac{\partial V^\alpha}{\partial x^\beta} + V^\mu \Gamma^{\alpha}{}_{\mu\beta} \right) \hat{e}_\alpha.
\end{aligned}$$

[5]The parallel transport of vector $\vec{V}$ along a curve $\vec{U}$ means $\vec{V}$ is defined at every point along the curve and requires $\vec{V}$ to be parallel and of equal length at infinitesimally close points along the curve.

and the curvature scalar, R, is its trace:

$$R = R^{\mu}{}_{\mu} = g^{\mu\nu} R_{\mu\nu}.$$

Now, let us factor in the presence of mass and energy that curves space-time. The symbol $T^{\mu\nu}$ is the energy-momentum tensor (also known as the stress-energy tensor). It represents everything we need to know about the energy-like aspects of the system. This includes the energy density (T^{00}), the momentum densities (T^{0i}), and the stresses (spatial terms T^{ij}, of which the diagonal terms, T^{ii}, are known as pressure).

All together, this summarizes the second statement, "In turn, matter reacts back on space, telling it how to curve." Thus, in the General Theory of Relativity, gravitation is a geometric effect that arises from objects trying to move along straight lines locally in an overall curved space-time, where space-time is curved because of the presence of mass and energy.

One of the consequences of this theory, as shall be seen in Section 2.2, is that changes in gravity (i.e., changes in the curvature of space-time) do not spread instantaneously throughout the Universe. Instead, they travel at the vacuum speed of light, c, in the form of gravitational waves[6].

2.2 Gravitational Waves

We can analyze the propagation of gravitational waves, which are changes to the curvature of space-time/gravitational field, in two spatial domains: in the near zone and the wave zone. These are defined by the following scaling

[6]This statement will be clarified in Section 2.3 to distinguish between gravitational potentials and traditional gravitational waves.

quantities:

$$\begin{aligned} t_c :=& \text{ characteristic time scale of the source, i.e.,} \\ & \text{time required for noticeable changes to} \\ & \text{occur within the source,} \\ \omega_c := \frac{2\pi}{t_c} =& \text{ characteristic frequency of the source,} \\ \lambda_c := \frac{2\pi c}{\omega_c} = ct_c =& \text{ characteristic wavelength of the} \\ & \text{gravitational waves,} \end{aligned}$$

where they are separated because (1) the difference between $\tau = t - r/c$ and t is small in the near zone versus large in the wave zone (i.e., field retardation is unimportant versus important) and (2) time derivatives are small compared with spatial derivatives (multiplied by a factor of c) in the near zone versus of order unity in the wave zone.

Then, the near zone and wave zone are defined as:

$$\text{near zone}, \mathscr{N} : r \ll \lambda_c$$

$$\text{wave zone}, \mathscr{W} : r \gg \lambda_c$$

where the general solution to the wave equation of form

$$\left(\nabla^2 - \frac{1}{c^2}\frac{\partial^2}{\partial t^2}\right)\psi = -4\pi\mu$$

is

$$\psi(t, \mathbf{x}) = \int \frac{\mu(t - |\mathbf{x} - \mathbf{x}'|/c, \mathbf{x}')}{|\mathbf{x} - \mathbf{x}'|} d^3x',$$

using the retarded Green's function. Here, the full set of Einstein field equations has been converted into a wave equation plus the harmonic gauge condition, i.e., the 'relaxed' field equations:

$$\left(\nabla^2 - \frac{1}{c^2}\frac{\partial^2}{\partial t^2}\right) h^{\alpha\beta} = -\frac{16\pi G}{c^4}\tau^{\alpha\beta} \text{ and}$$

$$\partial_\beta h^{\alpha\beta} = 0,$$

where $h^{\alpha\beta}$ are the gravitational potentials and $\tau^{\alpha\beta}$ is the effective energy-momentum pseudotensor. We drop the indices for simplicity to write down the general solutions and then evaluate in the near zone and wave zone limits to give:

$$\psi = \psi_{\mathscr{N}} + \psi_{\mathscr{W}}$$

for

$$\psi_{\mathscr{N}}(x) = \sum_{l=0}^{\infty} \frac{(-1)^l}{l!} \partial_L \left[\frac{1}{r} \int_{\mathscr{M}} \mu(\tau, \mathbf{x}') x'^L d^3x' \right],$$
$$\psi_{\mathscr{W}}(x) = \frac{n^{\langle L \rangle}}{r} \left[\int_0^{\mathscr{R}} ds f(\tau - 2s/c) A(s,r) + \int_{\mathscr{R}}^{\infty} ds f(\tau - 2s/c) B(s,r) \right]$$

when x is in the wave zone, and

$$\psi_{\mathscr{N}}(x) = \sum_{l=0}^{\infty} \frac{(-1)^l}{l! c^l} \left(\frac{\partial}{\partial t} \right)^l \int_{\mathscr{M}} \mu(t, \mathbf{x}') |\mathbf{x} - \mathbf{x}'|^{l-1} d^3x',$$
$$\psi_{\mathscr{W}}(x) = \frac{n^{\langle L \rangle}}{r} \left[\int_{\mathscr{R}-r}^{\mathscr{R}} ds f(\tau - 2s/c) A(s,r) + \int_{\mathscr{R}}^{\infty} ds f(\tau - 2s/c) B(s,r) \right]$$

when x is in the near zone.

In the solutions above, $\tau = t - r/c$ is retarded time, $\mathscr{M}$ is a surface of constant time bounded by the sphere $r' = \mathscr{R}$, L is a multi-index that contains l individual spatial indices, and μ is assumed to be of the form

$$\mu(x) = \frac{1}{4\pi} \frac{f(\tau)}{r^m} n^{\langle L \rangle}$$

where $\boldsymbol{n}$ is the radial unit vector $\mathbf{x}/r$, and $n^{\langle L \rangle}$ is the corresponding STF (symmetric trace-free) tensor:

$$n^{\langle j_1 j_2 \ldots j_l \rangle} = \sum_{p=0}^{[l/2]} (-1)^p \frac{l!(2l-2p-1)!!}{(l-2p)!(2l-1)!!(2p)!!} \times \delta^{(j_1 j_2} \delta^{j_3 j_4} \ldots \delta^{j_{2p-1} j_{2p}} n^{j_{2p+1}} n^{j_{2p+2}} \ldots n^{j_l)}$$

in which $[l/2]$ is the largest integer not larger than $l/2$, and the round brackets indicate symmetrization[7].

Lastly, $A(s,r)$ and $B(s,r)$ are:

$$A(s,r) = \int_{\mathscr{R}}^{r+s} \frac{P_l(\xi)}{r'^{(m-1)}} dr',$$
$$B(s,r) = \int_{s}^{r+s} \frac{P_l(\xi)}{r'^{(m-1)}} dr'$$

for $\xi = (r+2s)/r - 2s(r+s)/(rr')$ where P_l are the Legendre polynomials:

$$P_l(\mu) = \frac{1}{2^l l!} \frac{d^l}{d\mu^l} (\mu^2 - 1)^l.$$

So, a very good question one might ask at this point is, "Why did we do all this?" The answer is, we did it for the sake of completeness. In practicality, when solving for gravitational-wave signals that are characteristic of neutron star and/or black hole coalescences for instance, one approach is to integrate the wave equation in iterations, using an updated expression for the source that must satisfy the harmonic gauge condition each iteration.

For our purposes of deriving basic properties of gravitational waves and their effects on freely falling objects in the very far-away wave zone, we can study plane wave solutions to the wave equation in vacuum. This neglects corrections of order $\lambda_c/|\mathbf{x}| \ll 1$ which turn out to be very small. For example, a binary neutron star or black hole merger with a characteristic frequency near 100 Hz ($\lambda_c \sim 3000$ km) at a distance of 100 Mpc ($\sim 3\times 10^{21}$ km) will have terms we neglect of order 10^{-18}.

[7] A symmetrized rank-q tensor is defined by:

$$C^{(k_1 k_2 \cdots k_q)} = \frac{1}{q!}(C^{k_1 k_2 \cdots k_q} + \cdots),$$

where the remaining $\cdots$ terms consist of all possible permutations of the q indices.

Thus, plane wave solutions to the vacuum relaxed field equations:

$$\left(\nabla^2 - \frac{1}{c^2}\frac{\partial^2}{\partial t^2}\right) h^{\alpha\beta} = 0$$

are:

$$\begin{aligned} h^{00} &= 0, \\ h^{0j} &= 0, \\ h^{jk} &= \frac{G}{c^4|\mathbf{x}|} A^{jk}_{\mathrm{TT}}(\tau, \mathbf{x}/|\mathbf{x}|). \end{aligned}$$

The TT subscript in the h^{jk} expression means the gravitational potentials are evaluated in the transverse trace-free gauge, which is a specialization of the harmonic gauge condition. It indicates that the two independent components of A^{jk}_{TT} must contain all the radiative degrees of freedom regarding gravitational fields. This can be represented in matrix form as:

$$A^{jk}_{\mathrm{TT}} = \begin{pmatrix} A_+ & A_\times & 0 \\ A_\times & -A_+ & 0 \\ 0 & 0 & 0 \end{pmatrix}$$

in the case of a wave traveling in the $\hat{z}$-direction. The two degrees of freedom are referred to as the plus $(+)$ and cross $(\times)$ polarizations to describe their effect on a circular ring of freely falling particles lying in the x-y plane (Figure 2.1).

To see this, we consider the geodesic deviation equation:

$$\frac{D^2\xi^\alpha}{dt^2} = -R^\alpha{}_{\beta\gamma\delta} u^\beta \xi^\gamma u^\delta,$$

which describes the separation between two nearby freely falling masses, ξ^α, each moving along their respective geodesics with four-velocities u^α. Here, D/dt is the covariant derivative along the direction of u^α. Then, in the trans-

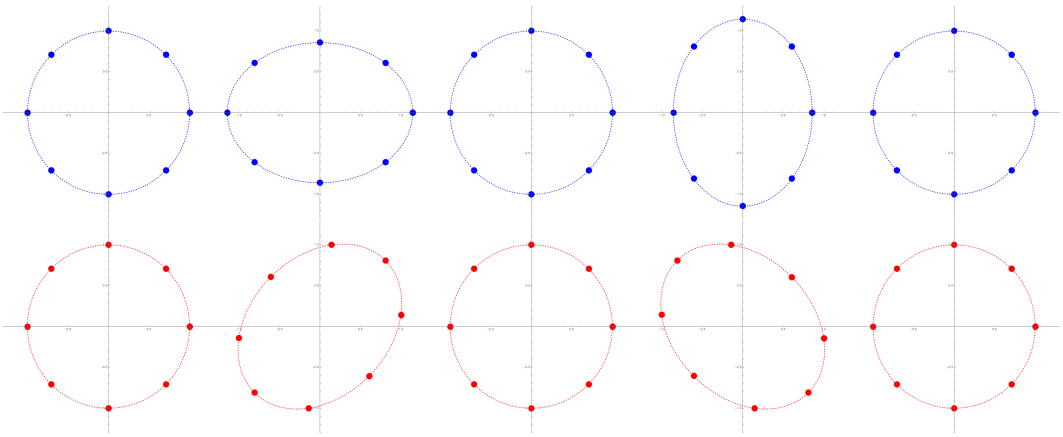

Figure 2.1: A circular ring of freely falling masses distorted by + (blue, top) and × (red, bottom) polarizations of a gravitational wave propagating out of the page. A rotation of 45° takes a + mode into a × mode and vice versa. For the figure, a complete wave cycle is shown from left to right.

verse trace-free gauge for slowly moving masses, the geodesic deviation equation becomes:

$$\frac{d^2\xi^j}{dt^2} = \frac{G}{2c^4|\mathbf{x}|}(\partial_{\tau\tau}A^{jk}_{\mathrm{TT}})\xi_k$$

which can be integrated to give us the solution:

$$\begin{aligned}\xi^j(t) &= \xi^j(0) + \frac{G}{2c^4|\mathbf{x}|}A^{jk}_{\mathrm{TT}}(t)\xi_k(0) \\ &= \begin{cases} \Delta x(t) = \Delta x_0 + \frac{G}{2c^4|\mathbf{x}|}(A_+(t)\Delta x_0 + A_\times(t)\Delta y_0), \\ \Delta y(t) = \Delta y_0 + \frac{G}{2c^4|\mathbf{x}|}(A_\times(t)\Delta x_0 - A_+(t)\Delta y_0), \\ \Delta z(t) = \Delta z_0. \end{cases}\end{aligned}$$

Thus, a purely + polarization gives us a distortion of the ring into an ellipse:

$$\left(\frac{\Delta x}{1+\eta_+(t)}\right)^2 + \left(\frac{\Delta y}{1-\eta_+(t)}\right)^2 = (\Delta x_0)^2 + (\Delta y_0)^2,$$

and a purely × polarization gives us a distortion of the ring into an ellipse:

$$\frac{1}{2}\left(\frac{\Delta x + \Delta y}{1+\eta_\times(t)}\right)^2 + \frac{1}{2}\left(\frac{\Delta x - \Delta y}{1-\eta_\times(t)}\right)^2 = (\Delta x_0)^2 + (\Delta y_0)^2,$$

where $\eta_+(t) = \frac{1}{2}(G/c^4|\mathbf{x}|)A_+(t)$ and $\eta_\times(t) = \frac{1}{2}(G/c^4|\mathbf{x}|)A_\times(t)$.

However, the positions of freely falling masses initially at rest do not change. To see this, we can take the geodesic equation for a freely falling mass where $dx^i/d\tau = 0$ at $\tau = 0$:

$$\begin{aligned}\left.\frac{d^2x^i}{d\tau^2}\right|_{\tau=0} &= -\left[\Gamma^i_{\mu\nu}\frac{dx^\mu}{d\tau}\frac{dx^\nu}{d\tau}\right]_{\tau=0} \\ &= -\left[\Gamma^i_{00}\left(\frac{dx^0}{d\tau}\right)^2\right]_{\tau=0}.\end{aligned}$$

Then, for a metric $g_{\mu\nu} = \eta_{\mu\nu} + h_{\mu\nu}$, the Christoffel symbols are:

$$\Gamma^\rho_{\mu\nu} = \frac{1}{2}\eta^{\rho\sigma}(\partial_\mu h_{\nu\sigma} + \partial_\nu h_{\sigma\mu} - \partial_\sigma h_{\mu\nu}).$$

Thus,

$$\begin{aligned}\left.\frac{d^2x^i}{d\tau^2}\right|_{\tau=0} &= -\left[\Gamma^i_{00}\left(\frac{dx^0}{d\tau}\right)^2\right]_{\tau=0} \\ &= -\left[\frac{1}{2}(2\partial_0 h_{0i} - \partial_i h_{00})\left(\frac{dx^0}{d\tau}\right)^2\right]_{\tau=0} \\ &0,\end{aligned}$$

because h^{00} and h^{0j} are both taken to be zero in the transverse trace-free gauge. Thus, $dx^i/d\tau$ must remain 0 at all times if the freely falling masses are initially at rest ($dx^i/d\tau|_{\tau=0} = 0$) and $d^2x^i/d\tau^2 = 0$.

This means we can think of marking the coordinates of the transverse trace-free gauge with freely falling masses. The positions of the masses (initially at rest) do not change although the coordinates are stretched and squeezed by incident gravitational waves. This interaction will allow us to conceptually build a gravitational-wave detector in Chapter 3.

2.3 Sources of Gravitational Waves

Although several astrophysical examples of gravitational-wave sources were mentioned in Chapter 1, we now explore more generally how gravitational waves are generated.

The first important result is known as Birkhoff's Theorem in the General Theory of Relativity. It states that space-time outside a spherical, non-rotating body (i.e., the spherically-symmetric solution to Einstein's field equations in vacuum) is static and given by the Schwarzschild external metric:

$$ds^2 = -\left(1 - \frac{R}{r}\right) d(ct)^2 + \left(1 - \frac{R}{r}\right)^{-1} dr^2 + r^2(d\theta^2 + \sin^2\theta \; d\phi^2),$$

where R is the Schwarzschild radius, $R = 2GM/c^2$, describing the body. This emphatically means spherically-symmetric matter distributions do not emit gravitational waves. Thus, for example, a perfectly spherically-symmetric core-collapse supernova would not generate any gravitational waves, despite large accelerations of mass and energy during the event.

This begs the question, "What kind of mass and energy motions produce gravitational waves?". The intuitive answer is non-spherically symmetric accelerations of mass and energy produce gravitational waves.

In the very far-away wave zone from perfect fluids moving in slow-motion ($|\mathbf{x}| \gg \lambda_c$), exact solutions to the relaxed field equations:

$$\left(\nabla^2 - \frac{1}{c^2}\frac{\partial^2}{\partial t^2}\right) h^{\alpha\beta} = -\frac{16\pi G}{c^4}\tau^{\alpha\beta}$$
$$\partial_\beta h^{\alpha\beta} = 0,$$

reduce to the gravitational potentials:

$$\begin{aligned}
h^{00} &= \frac{4G}{c^2|\mathbf{x}|}\left[M + \frac{1}{2c^2}\ddot{\mathcal{I}}^{jk} n_j n_k + \dots\right], \\
h^{0j} &= \frac{4G}{c^3|\mathbf{x}|}\left[\frac{1}{2c}\ddot{\mathcal{I}}^{jk} n_k + \dots\right], \\
h^{jk} &= \frac{4G}{c^4|\mathbf{x}|}\left[\frac{1}{2}\ddot{\mathcal{I}}^{jk} + \dots\right]
\end{aligned}$$

where M is the total gravitational mass of the source, $n^j = x^j/|\mathbf{x}|$, and overhead dots represent differentiation with respect to retarded time, $t - |\mathbf{x}|/c$.

The lowest order time dependent parts of $h^{\alpha\beta}$ are dominated by changes in the mass quadrupole moment, $\mathcal{I}^{jk}$:

$$\mathcal{I}^{jk}(t - r/c) = c^{-2} \int \tau^{00}(t - r/c, \mathbf{x}')x'^{j}x'^{k}d^3x' + \mathcal{O}(c^{-2}).$$

Thus, at the end of Section 2.1 where I stated, "...changes in gravity (i.e., changes in the curvature of space-time) do not spread instantaneously throughout the Universe. Instead, they travel at the vacuum speed of light, c, in the form of gravitational waves.", we can see that in the case of an object accelerating rectilinearly, the term $h^{00} = 4GM/c^2|\mathbf{x}|$ is the only "gravitational wave" that reflects the changing curvature at location $\mathbf{x}$. The aforementioned gravitational-wave polarizations and what we traditionally refer to as gravitational waves are the radiative parts of the above potentials, of which the lowest order term can be extracted in the transverse trace-free gauge, to give the quadrupole formula:

$$h^{jk}_{\mathrm{TT}} = \frac{2G}{c^4 R}\ddot{I}^{jk}_{TT},$$

where

$$I^{jk}(t - r/c) = c^{-2} \int \tau^{00}(t - r/c, \mathbf{x}')x'^{j}x'^{k}d^3x'.$$

With the quadrupole formula, we can investigate gravitational waves generated by binary systems, deformed rotating neutron stars, 'mountains' on an otherwise spherically symmetric neutron star, and more. We can also find a ballpark estimate for the gravitational-wave amplitude, h_0, due to a source of mass M confined to a volume of radius r_c, with changes on a characteristic time scale t_c. Then, the quadrupole moment scales as Mr_c^2 and $\ddot{I}^{jk}$ is of order $M(r_c/t_c)^2 \sim Mv_c^2$. This gives us:

$$\begin{aligned} h_0 &\sim \frac{GM}{c^2 R}\left(\frac{v_c}{c}\right)^2 \\ &\sim 3.2 \times 10^{-19}\left(\frac{M}{10M_\odot}\right)\left(\frac{1.5\ \mathrm{Mpc}}{R}\right)\left(\frac{v_c}{c}\right)^2, \end{aligned}$$

where 10 $M_\odot$ and 1.5 Mpc (the approximate size of the Local Group of galaxies) are used as reference. This shows that even the most violent and energetic processes in the Universe still produce tiny gravitational waves by the time they reach us.

2.4 The Hulse-Taylor Binary

This section presents the first indirect evidence of gravitational waves through observation of orbital decay in the Hulse-Taylor binary pulsar system. Readers who would like to skip ahead to learn more about advanced ground-based interferometric gravitational-wave detectors are advised to do so (see Chapter 3).

Pulsars were first discovered in the 1960s as point-sources emitting electromagnetic radiation in the radio band (Hewish et al., 1968). They are highly magnetized, rotating neutron stars with periods of the order $\tau \sim 10^{-3}$ to 1 seconds. Since their original detection, over two thousand pulsars have been discovered and they are now known to emit radiation in the radio, optical, X-ray, and/or gamma-ray wavelengths (Lorimer, 2008). The period of most pulsars increases slowly with time and in a very regular manner. This predictability of the pulse time arrivals means pulsars can be used as clocks, on par with the most accurate man-made clocks.

In the case of the pulsar in the Hulse-Taylor binary system, the pulsar rotates on its axis approximately 17 times per second (Taylor & Weisberg, 1982) so the pulsation period τ is $1/17 = 0.059$ s with an angular period of

$$\omega = \frac{2\pi}{\tau} = \frac{2\pi}{0.059 \text{ s}} = 106.5 \text{ s}^{-1}.$$

The pulsar's measured period derivative is

$$\frac{d\tau}{dt} = 8.62 \times 10^{-18}$$

or

$$\frac{d\omega}{dt} = -\frac{2\pi}{\tau^2}\frac{d\tau}{dt} = -\frac{2\pi}{(0.059\text{ s})^2} \times 8.62 \times 10^{-18}$$
$$= -1.55 \times 10^{-14}\text{ s}^{-2}.$$

Furthermore, the upper limit on the time-averaged X-ray and optical flux from the pulsar region is of the order 10^{-10} erg s^{-1} cm^{-2} (Davidsen et al., 1975), meaning the X-ray and optical luminosity of the pulsar region has an upper limit of

$$L_{\text{tot}} = 10^{-10}\frac{\text{erg}}{\text{cm}^2\text{s}} \times (6400\text{ pc})^2 \times (\frac{31 \times 10^{17}\text{ cm}}{1\text{ pc}})^2$$
$$\approx 4 \times 10^{34}\text{ erg s}^{-1},$$

where 6400 pc is the distance to the binary.

The source of this luminosity is mostly in the form of synchrotron radiation, i.e., the radiation emitted by relativistic electrons as they spiral around magnetic field lines.

Pulsars Are Neutron Stars

To see that pulsars are spinning neutron stars, we will consider three possible mechanisms for producing periodicity of the observed magnitude and regularity: binaries, stellar pulsation, and stellar rotations.

For binaries, Kepler's law relates the angular frequency, masses, and separation distance as

$$\omega^2 = \frac{G(M_1 + M_2)}{a^3},$$

and therefore we get

$$\begin{aligned} a &= \frac{(G(M_1 + M_2))^{1/3}}{\omega^{2/3}} \\ &= \frac{(6.7 \times 10^{-11} \frac{\text{m}^3}{\text{kg s}^2} \times (4 \times 10^{30} \text{ kg}))^{1/3}}{(106.5 \text{ s}^{-1})^{2/3}} \\ &\approx 300 \text{ km}, \end{aligned}$$

if we assume two solar-mass objects and use the pulsar's frequency. This gives us a separation, a, which is much smaller than the radii of normal stars ($\sim 10^5$ km) or white dwarfs ($\sim 10^3$ km). Only a pair of neutron stars could exist in a binary at the above scale of separation. However, if two neutron stars were orbiting each other at such a close distance, the system would lose gravitational binding energy via the emission of gravitational waves, causing the separation distance to shrink and orbital frequency to grow, which contradicts our observation that pulsar frequencies decrease with time. Indeed, this is because pulsars have other mechanisms to lose spin energy, e.g., via magnetic dipole radiation. Thus, we can conclude that pulsars cannot be explained by orbital motion of stellar-mass objects, with the exception of neutron stars under special circumstances involving large magnetic fields to account for observed spin-downs.

Next, stars are observed to pulsate regularly in various modes, with the pulsation period dependent on density as $\tau \propto \rho^{-1/2}$. Normal stars have pulsation periods between hours and months and white dwarfs have pulsation periods of 100 to 1000 s. Neutron stars are about 10^8 times denser than white dwarfs, and should therefore have periods 10^4 times shorter than white dwarfs, putting them in the range 0.01 to 0.1 s. However, the most common period for pulsars is about 0.8 s, which is just outside the predicted pulsation range. Therefore, we rule out stellar pulsations as an explanation for pulsar periodicity.

And finally, we consider anisotropic emission from a rotating star as an explanation for pulsar periodicity. First, we can work out what the maximum mean density of the pulsar must be when it is spinning as fast as it can without breaking apart due to centrifugal forces:

$$\frac{GMm}{r^2} > m\omega^2 r \Rightarrow \frac{M}{r^3} > \frac{\omega^2}{G},$$

and therefore,

$$\bar{\rho} = \frac{3M}{4\pi r^3} > \frac{3\omega^2}{4\pi G} = \frac{3(106.5 \text{ s}^{-1})^2}{4\pi \times 6.7 \times 10^{-11} \frac{\text{m}^3}{\text{kg s}^2}}$$
$$= 4 \times 10^{13} \text{ kg m}^{-3}$$

for the pulsar in the Hulse-Taylor binary. This means if the pulsar is a spinning star and is not flying apart, it cannot be a white dwarf whose mean density is four to five orders of magnitude smaller, $\sim 10^9$ kg m^{-3}. Also, pulsars with the shortest periods of about 1 ms compared to our 59 ms, must have mean densities about 3000 times larger to avoid breaking apart, $\sim 10^{17}$ kg m^{-3}, which is the mean density predicted for neutron stars.

Thus, it is accepted that pulsars are neutron stars. Their spin rate is what would be expected from core-collapse of massive main-sequence stars down to neutron star dimensions. For millisecond pulsars, it is believed they are spun up by accretion after the neutron star formation. Also, loss of rotational energy and decreasing pulsar frequency over time can be explained by the outgoing radiation from the pulsar and surrounding nebula.

Pulsar Emission Mechanism and Age

Although the exact details of pulsar emission mechanism are still debated and an active area of research, it is widely accepted that periodic emission from

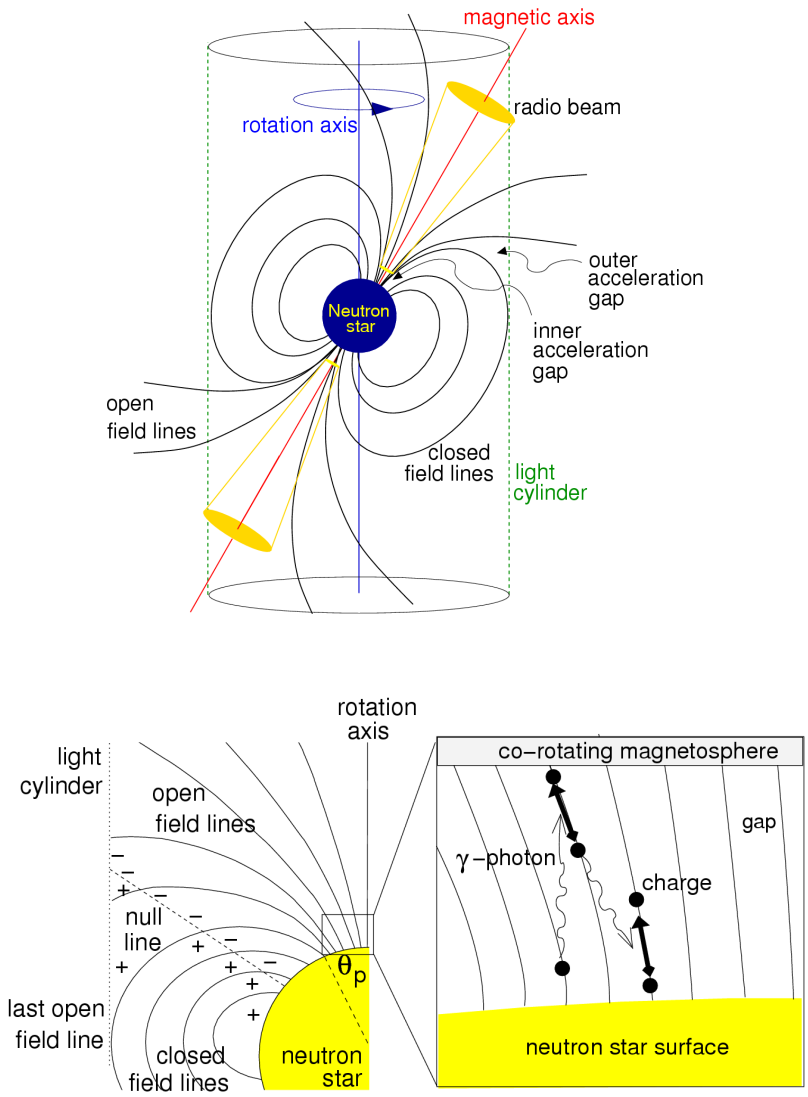

Figure 2.2: Schematic model of a pulsar. (Figure from Lorimer & Kramer, 2004)

pulsars is due to misalignment of the magnetic field axis and the star's rotation axis by some angle θ. This misalignment has the structure of a rotating magnetic dipole, as seen in Figure 2.2.

Then, we know that a spinning magnetic dipole emits electromagnetic

radiation with luminosity

$$L \sim B^2 r^6 \omega^4 \sin^2\theta$$

where B is the magnetic field on the surface of the star, at a radius r along the magnetic field axis. This is the basic emission mechanism that is held responsible for the pulsar's loss of rotational energy. Then,

$$\frac{dE_{\rm rot}}{dt} = I\omega\frac{d\omega}{dt} \propto \omega^4$$

and

$$\frac{d\omega}{dt} \propto \omega^3 = C\omega^3$$

for some constant C, which can be determined from present-day values of $d\omega/dt$ and ω as

$$C = \frac{\dot{\omega}_0}{\omega_0^3}.$$

This means that we can obtain an upper limit on the age of the pulsar by integrating the equation as follows:

$$t_{\rm pulsar} = \frac{\omega_0^3}{2\dot{\omega}_0}\left(\frac{1}{\omega_{\rm i}^2} - \frac{1}{\omega^2}\right),$$

where $\omega_{\rm i}$ is the initial angular frequency of the neutron star upon formation. Therefore, the upper limit on the age of the Hulse-Taylor pulsar is obtained by taking $\omega = \omega_0$ and $\omega_{\rm i} = \infty$:

$$\begin{aligned} t_{\rm pulsar} < \frac{\omega_0}{2|\dot{\omega}_0|} &= \frac{106.5\ {\rm s}^{-1}}{2 \times 1.55 \times 10^{-14}\ {\rm s}^{-2}} = 3.4 \times 10^{15}\ {\rm s} \\ &= 1 \times 10^8\ {\rm years}. \end{aligned}$$

Now, if we call ρ the distance from the rotation axis in cylindrical distance, magnetic field lines that reach a distance $\rho > c/\omega$ must open and escape to infinity. This is because c/ω is the maximum distance at which an object

can co-rotate with the star and not exceed the speed of light. Only the field lines fully contained within that maximum distance are closed, as shown in Figure 2.2.

Then, high-energy charged particles accelerate around the open field lines and emit electromagnetic radiation, most easily observed in the radio wavelengths. Because the open field lines are concentrated near the magnetic poles, the radiation forms two conical beams centered along the magnetic field axis, as shown in Figure 2.2. Then, as the pulsar spins on its rotation axis, the beams sweep out an annulus in the sky and distant observers detect a pulse once every rotation if they happen to lie along the path of the beams.

Timing with Pulsar Profiles

Each pulse from a pulsar has a unique shape. It is only when many such pulses are added up that the pulsar's profile can be built. The intensity and shape of the profile is frequency dependent. In Figure 2.3, we have the pulse profile for the pulsar in the Hulse-Taylor binary at 430 MHz.

Given that a millisecond pulsar will rotate over one million times during a one hour duration, an error in the rotational period will produce a shift in the time of arrivals at the end of the hour that is a million times larger. Thus, if we can measure the time of arrivals to a precision of 1 millisecond, then the rotational period of the pulsar can be resolved to a precision of 10^{-12} seconds, the equivalent of 9 decimal places for millisecond pulsars! This is why pulsars can be used as very accurate clocks.

However, most pulsars do show departures from simple, uniformly slowing rotation. One significant departure are glitches in the pulses. These glitches are thought to be caused by 'starquakes', which are sudden changes in the magnetic field configuration of the pulsar (Franco et al., 2000) due to crust

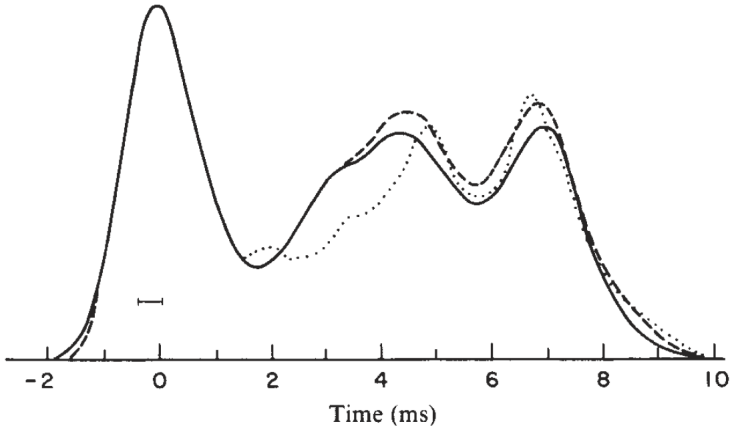

Figure 2.3: Pulse profile at 430 MHz for the pulsar in Hulse-Taylor binary. Observed during July 1977 (dotted line), June 1978 (dashed line), and October 1978 (solid line). The central component has been gradually moving to the left and becoming broader, while the third component has shifted to the right. All profiles have been smoothed to the resolution indicated by the horizontal bar, 400 μs. (Figure from Taylor et al., 1979)

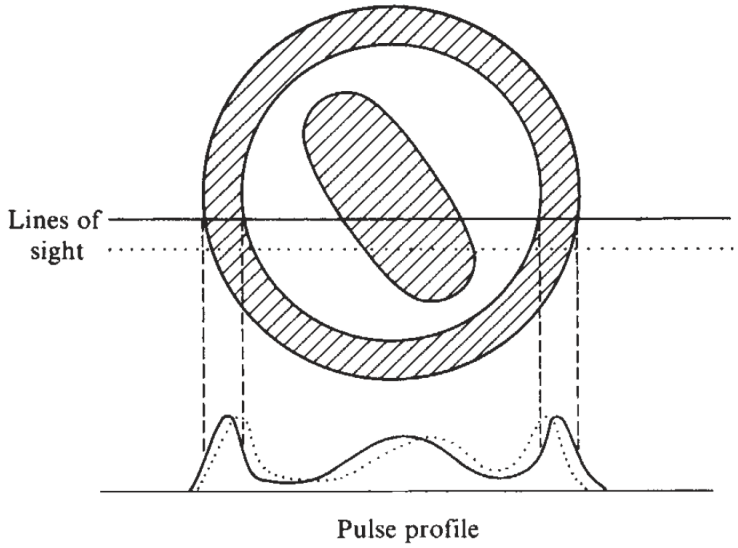

Figure 2.4: A possible geometry to account for pulse shape changes in the Hulse-Taylor binary. (Figure from Taylor et al., 1979)

cracking. For most pulsars, the magnetic field seems to increase after each glitch. Ultimately, the origin is unexplained and still an active area of research.

One possible explanation for the pulse shape changes is the following.

The shaded regions in Figure 2.4 represent active portions of a hollow cone of pulsar emission (the cross-section). The horizontal line in the figure represents the loci of the line of sight through the beam as the pulsar spins. Therefore, when the spin axis precesses, different portions of the beam move into the line of sight and thus the pulse profile would change. After three decades of observation at Arecibo, it is now assumed that the conal beams might be hourglass-shaped (Weisberg & Taylor, 2002).

Pulsar Timing Formula for Isolated Pulsars

An observer on Earth records the times, $\tau_{\rm obs}$, of the arriving pulses from an isolated pulsar. Our goal is to translate these times into times that are only dependent on the intrinsic properties of the source. As recorded, these $\tau_{\rm obs}$'s are affected by Earth's motion around the Sun, Earth's spinning on its axis, the gravitational redshifts of the Earth and the Sun, and the dispersion of the pulse as it travels through the interstellar medium. If we could subtract out these effects, we would then be left with times $t_{\rm SSB}$, which are the coordinate times at which the pulse recorded on Earth would have arrived at the Solar System Barycenter (SSB), which is the Solar System's center of mass. After we figure out how to do this, we consider the case of a pulsar in a binary.

Roemer Time Delay

The first step to getting the barycentric time of arrivals is to account for the Roemer time delay. The motion of Earth around the Sun causes a modulation in the arrival time of the pulses. Because the orbit lies very nearly in a plane, it can be described with Ω, the angular velocity of Earth around the Sun, and t_0, the time it takes light to travel from the Sun to Earth. And therefore, if a pulsar is at a latitude β above the plane of the ecliptic, the

modulation in the arrival time of the pulses can be written as

$$\triangle_{R,\odot} = t_0 \cos(\Omega t - \lambda) \cos\beta.$$

This would be precise enough classically but for pulsar timing, we need to account for Earth spinning on its axis, the orbit of Earth being elliptical, and the Sun moving around the SSB due to Jupiter's influence. The most practical way to deal with all of these effects is to account for the corrections by referring all arrival times for the observer to the SSB. Thus, we need the vector from the observer to the SSB:

$$\vec{r}_{\rm ob} = \vec{r}_{\rm oe} + \vec{r}_{\rm es} + \vec{r}_{\rm sb}$$

where $\vec{r}_{\rm oe}$ is from the observer to the center of Earth, $\vec{r}_{\rm es}$ is from the center of Earth to the center of the Sun, $\vec{r}_{\rm sb}$ is from the center of the Sun to the SSB. Then, the time we need to add to the times observed in the laboratory is

$$\triangle_{R,\odot} = -\vec{r}_{\rm ob} \cdot \hat{n}/c$$

where $\hat{n}$ is the unit vector from the SSB to the pulsar. This is the Roemer time delay in the solar system.

Shapiro Time Delay

The second step to getting the barycentric time of arrivals is to account for the Shapiro time delay. The pulse traveling in the vicinity of the Sun will take slightly longer to get to Earth than if the Sun were not there. To see this, we start with the space-time interval linearly approximated as

$$ds^2 = -(1 + 2\phi(\vec{x}))c^2dt^2 + (1 - 2\phi(\vec{x}))d\vec{x}^2.$$

And therefore photons traveling on the light-like geodesic ($ds^2 = 0$) satisfy to lowest order in ϕ:

$$cdt = \pm(1 - 2\phi(\vec{x}))|d\vec{x}|.$$

This expansion is safe to do because in the solar system, $|\phi(\vec{x})| = GM_\odot/rc^2$ is at most of order 10^{-6}. For instance, between the Sun and Mercury we get

$$\begin{aligned}\phi(\vec{x}) &= -\frac{GM_\odot}{rc^2} = -\frac{6.7\times10^{-11}\frac{\mathrm{m}^3}{\mathrm{kg\ s}^2}\times 2\times10^{30}\ \mathrm{kg}}{5.8\times10^{10}\ \mathrm{m}\times(3\times10^8\frac{\mathrm{m}}{\mathrm{s}})^2}\\ &\approx -2.6\times10^{-8}.\end{aligned}$$

Then, we can now calculate the *coordinate* time difference between the arrival time, t_{obs}, and the emission time at the pulsar, t_{e}. If we locate the fixed location of the pulsar with $\vec{r}_{\mathrm{p}}$ and the location of the observer at t_{obs} as $\vec{r}_{\mathrm{p}}$, then we get

$$\begin{aligned}c(t_{\mathrm{obs}}-t_{\mathrm{e}}) &= \int_{\vec{r}_{\mathrm{obs}}}^{\vec{r}_{\mathrm{p}}}|d\vec{x}|(1-2\phi(\vec{x}))\\ &= |\vec{r}_{\mathrm{p}}-\vec{r}_{\mathrm{obs}}| - 2\int_{\vec{r}_{\mathrm{obs}}}^{\vec{r}_{\mathrm{p}}}|d\vec{x}|\phi(\vec{x}).\end{aligned}$$

And now using the notation from above:

$$\begin{aligned}|\vec{r}_{\mathrm{p}}-\vec{r}_{\mathrm{obs}}| &= |(\vec{r}_{\mathrm{p}}-\vec{r}_{\mathrm{b}})+(\vec{r}_{\mathrm{b}}-\vec{r}_{\mathrm{obs}})|\\ &\approx |\vec{r}_{\mathrm{p}}-\vec{r}_{\mathrm{b}}| + (\vec{r}_{\mathrm{b}}-\vec{r}_{\mathrm{obs}})\cdot\frac{(\vec{r}_{\mathrm{p}}-\vec{r}_{\mathrm{b}})}{|\vec{r}_{\mathrm{p}}-\vec{r}_{\mathrm{b}}|}\\ &= |\vec{r}_{\mathrm{p}}-\vec{r}_{\mathrm{b}}| + (\vec{r}_{\mathrm{b}}-\vec{r}_{\mathrm{obs}})\cdot\hat{n}.\end{aligned}$$

Then, substituting back we get

$$c(t_{\mathrm{obs}}-t_{\mathrm{e}}) \approx |\vec{r}_{\mathrm{p}}-\vec{r}_{\mathrm{b}}| + (\vec{r}_{\mathrm{b}}-\vec{r}_{\mathrm{obs}})\cdot\hat{n} - 2\int_{\vec{r}_{\mathrm{obs}}}^{\vec{r}_{\mathrm{p}}}|d\vec{x}|\phi(\vec{x}).$$

and writing $\vec{r}_{\mathrm{b}}-\vec{r}_{\mathrm{obs}}$ as $\vec{r}_{\mathrm{ob}}$ and rearranging gives us

$$t_{\mathrm{obs}} \approx \left(t_{\mathrm{e}} + \frac{1}{c}|\vec{r}_{\mathrm{p}}-\vec{r}_{\mathrm{b}}|\right) + \frac{1}{c}\vec{r}_{\mathrm{ob}}\cdot\hat{n} - \frac{2}{c}\int_{\vec{r}_{\mathrm{obs}}}^{\vec{r}_{\mathrm{p}}}|d\vec{x}|\phi(\vec{x}).$$

The terms in the parenthesis is the barycentric time of arrival, t_{SSB}, which is the time the pulse would have arrived at the SSB if there were no effects

from the solar system's gravity. Therefore, we can get

$$t_{\rm SSB} = t_{\rm obs} - \frac{1}{c}\vec{r}_{\rm ob}\cdot\hat{n} + \frac{2}{c}\int_{\vec{r}_{\rm obs}}^{\vec{r}_{\rm P}} |d\vec{x}|\phi(\vec{x}).$$

The first correction is the Roemer delay that we found in Subsection 2.4. The second term is (minus) the solar system Shapiro time delay:

$$\triangle_{S,\odot} = -\frac{2}{c}\int_{\vec{r}_{\rm obs}}^{\vec{r}_{\rm P}} |d\vec{x}|\phi(\vec{x})$$

so that in condensed form we have so far:

$$t_{\rm SSB} = t_{\rm obs} + \triangle_{R,\odot} - \triangle_{S,\odot}.$$

If we want to calculate the maximum modulation in time induced by the Shapiro time delay, we must study the photon whose path from the pulsar to Earth just grazes the surface of the Sun. The value for $\triangle_{S,\odot}$ ends up being positive when calculated which agrees physically with the pulse arriving later since it must travel through the potential well created by the Sun.

Einstein Time Delay

Next, the Einstein time delay will account for time dilation between the clock moving with the observer, located at $\vec{x}_{\rm obs}$, versus the clock at the SSB. To see this, we start with the relationship between the observer's proper time τ versus the coordinate time t:

$$-c^2 d\tau^2 = -(1+2\phi(\vec{x}_{\rm obs}))c^2dt^2 + (1-2\phi(\vec{x}_{\rm obs}))d\vec{x}_{\rm obs}^2.$$

Then, we get

$$\frac{d\tau}{dt} = \left((1+2\phi(\vec{x}_{\rm obs})) - \frac{1}{c^2}(1-2\phi(\vec{x}_{\rm obs}))\frac{d\vec{x}_{\rm obs}^2}{dt^2}\right)^{1/2}.$$

And now using the notation $\vec{v}_{\rm obs} = d\vec{x}_{\rm obs}/dt$, we have to first order in the small parameters $\phi(\vec{x}_{\rm obs})$ and $\vec{v}_{\rm obs}$:

$$\frac{d\tau}{dt} \approx 1 + \phi(\vec{x}_{\rm obs}) - \frac{v_{\rm obs}^2}{2c^2}.$$

Integrating, we get

$$\tau \approx t + \int^t dt' \left(\phi(\vec{x}_{\rm obs}(t')) - \frac{v_{\rm obs}^2(t')}{2c^2} \right)$$

where the lower limit of the integral corresponds to an arbitrary constant shift in the origin of τ. Therefore, the Einstein time delay can be found from the relation $t \approx \tau + \triangle_{E\odot}$ as

$$\triangle_{E\odot} = \int^t dt' \left(\frac{v_{\rm obs}^2(t')}{2c^2} - \phi(\vec{x}_{\rm obs}(t')) \right)$$

Physically, the first term is dominant and is mostly due to the motion of Earth around the Sun and Earth spinning on its axis. Thus, $v_{\rm obs} \approx v_\oplus$. The second term gives us the gravitational redshift of the observer. In this case, as the observer moves away from the Sun, the rate at which time passes is increased relative to the case when the observer is closer to the Sun.

Dispersion in the Interstellar Medium

Pulses coming from the pulsar must travel through ionized interstellar gas before arriving at the observer. This gas effectively acts as a medium with index of refraction, n, significantly different from 1, which is the index of refraction of vacuum. Then, the frequency-dependent expression for the index of refraction is

$$n(\nu) = \frac{v_{\rm g}(\nu)}{c} \approx 1 - \frac{n_e e^2}{2\pi m_e} \frac{1}{\nu^2}$$

where $v_{\rm g}(\nu)$ is the group velocity of the pulse with frequency ν, e and m_e are the charge and mass of the electron, and n_e is the electron number density.

Then, the time for the pulse to travel a distance L is given by

$$\int_0^L \frac{dl}{v_g} \approx \frac{L}{c} + \left(\frac{e^2}{2\pi m_e c}\right) \frac{1}{\nu^2} \int_0^L n_e dl.$$

The quantity $\int_0^L n_e dl$ is called the dispersion measure, DM, and is typically given in cm^{-3} pc. By measuring the time of arrivals for different frequency bandwidths, we can find the DM and correct for its effect. This procedure is called de-dispersion and is crucial for pulsar observations. For values of large enough DM's, the pulses can be spread out enough that it ends up being greater than the intrinsic period of the pulsar, making the pulsar unobservable. In the search for pulsars, the DM is an unknown parameter and data are de-dispersed with various possible values. In the case of the Hulse-Taylor binary, the DM is measured to be 169 cm^{-3} pc (Hulse & Taylor, 1975). The pulses were discovered near the frequency channel 430 MHz at Arecibo Observatory, see Figure 2.3.

Thus, if we want to move the time of arrivals to the barycentric system, we need to subtract out this dispersion effect. It can be summarized as

$$\triangle_{\text{disp}} = \left(\frac{e^2}{2\pi m_e c}\right) \frac{1}{\nu^2} \text{ DM} = \frac{D}{\nu^2}.$$

Relation to the Intrinsic Pulsar Signal

All of the delays mentioned above are small and therefore can be added up linearly. Then, the time of arrivals in the barycentric system are related to the time of arrivals of the observer by:

$$t_{\text{SSB}} = \tau_{\text{obs}} - \frac{D}{\nu^2} + \triangle_{E\odot} + \triangle_{R,\odot} - \triangle_{S,\odot}.$$

These times only depend on the intrinsic properties of the pulsar because we have accounted for the effects from the solar system's gravitational field

and the pulse's interaction with the interstellar gas. Now, we want to relate these time of arrivals to the time of emission according to the pulse's proper time, T. To do this, we start by defining the accumulated phase of the spinning pulsar as Φ.

If Φ_0 is the angle at which the pulse sweeps across Earth, we will see a pulse whenever $\Phi \mod 2\pi \equiv \Phi_0$. Now, because the pulses carry energy away from the pulsar, the spinning frequency of the pulsar, ν, cannot be a constant. It can be expanded around some reference value T_0 as

$$\nu(T) = \nu_0 + \dot{\nu}_0 T + \frac{1}{2}\ddot{\nu}_0 T^2 + \ldots,$$

where $\dot{\nu}_0$, $\ddot{\nu}_0$, etc are called spindown parameters.

Then, the accumulated phase is given by

$$\begin{aligned}\Phi(T) &= 2\pi \int_0^T d\tau \nu(\tau) \\ &= \nu_0 T + \frac{1}{2}\dot{\nu}_0 T^2 + \frac{1}{3!}\ddot{\nu}_0 T^3 + \ldots \ .\end{aligned}$$

Then, emission will take place at proper times T_n such that $\Phi(T_n) \mod 2\pi \equiv \Phi_0$, i.e., $\Phi(T_n) = \Phi_0 + 2\pi n$. Then, the emission proper times, T_n, are given by

$$\nu_0 T_n + \frac{1}{2}\dot{\nu}_0 T_n^2 + \frac{1}{3!}\ddot{\nu}_0 T_n^3 + \cdots = \frac{\Phi_0}{2\pi} + n.$$

Thus, if there were no spindown parameters, the emission times would be exactly

$$T_n = \frac{\Phi_0}{2\pi\nu_0} + \frac{n}{\nu_0}.$$

However, spindown parameters do exist and they produce deviations from these times. The typical dissipation mechanisms for pulsars typically behave as $\dot{\nu} \approx C\nu^n$, for some constant C and $n \sim 2{-}3$.

In the case of the Hulse-Taylor pulsar, $\nu_0 \approx 16.9\ \mathrm{s}^{-1}$ and $\dot{\nu}_0 \approx -2.5 \times 10^{-15}\ \mathrm{s}^{-2}$. Thus, from the above model, we can expect $\ddot{\nu}_0 \approx Cn\nu^{n-1}\dot{\nu} = Cn\nu^n\dot{\nu}/\nu = n\dot{\nu}^2/\nu$ and therefore $\ddot{\nu}_0 \approx 3{\times}10^{-31}\ \mathrm{s}^{-3}$. This effect is unobservably small and can be ignored. Then, it is sufficient to keep only up to the $\dot{\nu}_0$ term.

The final step is to connect these pulsar proper times of emission, T_n, with the corresponding coordinate times, $t_{\mathrm{em},n}$. Once we find this relation, we can relate these coordinate times of emission to the time of arrivals at the SSB as $t_{\mathrm{SSB}} = t_{\mathrm{em},n} + d/c$ where d is the distance between the pulsar and the SSB.

Further Corrections for Binary Pulsars

We must also correct for the Roemer, Shapiro, and Einstein time delays for pulsars in binaries. However, because the binary has a much stronger gravitational field than the Solar System, each time delay must be treated with the General Theory of Relativity in mind and becomes technically more difficult. We will sketch how to do this for each case and discuss other corrections that come into play.

Einstein Time Delay

The Einstein delay in this case will relate the proper time kept on the pulsar to the time that is kept at the center of mass system of the binary. Here, I will sketch how to do this, still using Kepler's laws as a description of the pulsar's trajectory. First, we start by writing the potential at the location on the pulsar where the beam is emitted, $\vec{x}$:

$$\phi(\vec{x}) = -\frac{Gm_p}{c^2|\vec{x} - \vec{x}_p|} - \frac{Gm_c}{c^2|\vec{x} - \vec{x}_c|}$$

where m_p, m_c, $\vec{x}_p$, $\vec{x}_c$ are the masses and locations of the pulsar and companion star.

However, the first term in the potential is time independent since the location of the emission does not change with respect to the pulsar's center of mass. Even though in magnitude it is significant ($Gm_p/c^2 r_{\rm NS} \sim 0.2$), we can absorb it into a constant rescaling of the proper time T. Thus, the time-dependent part of the Einstein time delay is due entirely to the second term:

$$\phi(\vec{x}) = -\frac{Gm_c}{c^2|\vec{x} - \vec{x}_c|}.$$

Then, as in Subsection 2.4 on the Einstein time delay, we have

$$\frac{dT}{dt} = 1 - \frac{Gm_c}{c^2|\vec{x} - \vec{x}_c|} - \frac{v_p^2}{2c^2},$$

where v_p is the the pulsar's velocity given by the relation

$$v_p = \frac{m_c}{m_p + m_c} v,$$

where v is the relative velocity in the center of mass system. It can be found from the classical relation

$$\frac{1}{2}v^2 - \frac{G(m_p + m_c)}{r} = -\frac{G(m_p + m_c)}{2a}.$$

Therefore, plugging this back into our equation we get

$$\begin{aligned}
\frac{dT}{dt} &= 1 - \frac{Gm_c}{c^2|\vec{x} - \vec{x}_c|} - \frac{1}{c^2}\left(\frac{m_c}{m_p + m_c}\right)^2 \frac{v^2}{2} \\
&= 1 - \frac{Gm_c}{c^2 r} - \frac{G}{c^2}\left(\frac{m_c}{m_p + m_c}\right)^2 \left(\frac{m_p + m_c}{r} - \frac{m_p + m_c}{2a}\right) \\
&= 1 - \frac{G}{c^2}\left(\frac{m_c(m_p + 2m_c)}{m_p + m_c}\frac{1}{r} - \frac{m_c^2}{m_p + m_c}\frac{1}{2a}\right).
\end{aligned}$$

And now, we need to find another expression for dT/dt that depends on other measurable parameters of the orbit. Thus, we recall that the binary can be described as a Keplerian orbit

$$u - e\sin u = \frac{2\pi}{P_b}(t - t_0),$$

where t_0 is a reference time of passage through the periastron and u is the eccentric anomaly, $r = a(1 - e\cos u)$. Then, differentiation gives us

$$\frac{du}{dt}(1 - e\cos u) = \frac{2\pi}{P_b},$$

and thus

$$\frac{dT}{dt} = \frac{du}{dt}\frac{dT}{du} = \frac{2\pi}{P_b}\frac{1}{1 - e\cos u}\frac{dT}{du}.$$

Then, equating the two versions of dT/dt together gives us

$$\frac{2\pi}{P_b}\frac{1}{1 - e\cos u}\frac{dT}{du} = 1 - \frac{G}{c^2}\left(\frac{m_c(m_p + 2m_c)}{m_p + m_c}\frac{1}{r} - \frac{m_c^2}{m_p + m_c}\frac{1}{2a}\right)$$

which can be re-written as

$$\begin{aligned}\frac{2\pi}{P_b}\frac{dT}{du} &= \left(1 - \frac{G}{c^2}\frac{2m_cm_p + 3m_c^2}{2a(m_p + m_c)}\right) \\ &\quad - e\cos u\left(1 + \frac{G}{c^2}\frac{m_c^2}{2a(m_p + m_c)}\right) \\ &\approx \left(1 - \frac{G}{c^2}\frac{2m_cm_p + 3m_c^2}{2a(m_p + m_c)}\right) \\ &\quad \times \left(1 - e\cos u\left(1 + \frac{G}{c^2}\frac{m_c(m_p + 2m_c)}{a(m_p + m_c)}\right)\right).\end{aligned}$$

In the above equation, only the part proportional to $\cos u$ produces a modulation and is observable. And therefore, we rescale the proper time T:

$$T \Rightarrow \left(1 - \frac{G}{c^2}\frac{2m_cm_p + 3m_c^2}{2a(m_p + m_c)}\right)T.$$

Therefore, we end up with

$$\frac{dT}{du} = \frac{P_b}{2\pi}(1 - e\cos u) - \gamma\cos u$$

where γ is the Einstein parameter given explicitly by

$$\begin{aligned}\gamma &= e\left(\frac{P_b}{2\pi}\right)\frac{G}{c^2}\frac{m_c(m_p + 2m_c)}{a(m_p + m_c)} \\ &= e\left(\frac{P_b}{2\pi}\right)^{1/3}\frac{G^{2/3}}{c^2}\frac{m_c(m_p + 2m_c)}{(m_p + m_c)^{4/3}},\end{aligned}$$

where we eliminated a by using the Keplerian relation $G(m_p + m_c)/a^3 = (2\pi/P_b)^2$. Then, we can find the Einstein delay by writing T as $t - \triangle_E$. By using

$$\frac{dT}{du} = \frac{d(t - \triangle_E)}{du} = \frac{P_b}{2\pi}(1 - e\cos u) - \gamma\cos u$$

and

$$\frac{dt}{du} = \frac{P_b}{2\pi}(1 - e\cos u)$$

we get

$$\frac{d\triangle_E}{du} = \gamma\cos u$$

which means

$$\triangle_E = \gamma\sin u.$$

In the case of the Hulse-Taylor binary, plugging in observed values of $P_b \approx 27906$ s and $e \approx 0.61713$ (Taylor & Weisberg, 1982) gives us

$$\gamma \approx 2.94 \text{ ms} \left(\frac{m_c}{M_\odot}\right)\left(\frac{m_p + 2m_c}{M_\odot}\right)\left(\frac{m_p + m_c}{M_\odot}\right)^{-4/3}.$$

Roemer Time Delay

Because the pulsar travels in an orbit, $\vec{x}_1(t)$, around the binary system's center of mass, there is a modulation in the pulsar's location each time it emits a pulse. Thus, there is a Roemer effect we must compute. As seen in Subsection 2.4 for the Roemer time delay, the form for it is given by $\triangle_R = -\vec{x}_1 \cdot \hat{n}/c$, where $\vec{x}_1$ is the position of the pulsar in the binary center of mass system and $\hat{n}$ is the unit vector from the SSB to the binary center of mass (along the line of sight). If we define the following variables:

$$\vec{X} = \frac{m_1^*\vec{x}_1 + m_2^*\vec{x}_2}{m_1^* + m_2^*}$$

where

$$m_A^* = m_A + \frac{m_A v_A^2}{2c^2} - \frac{Gm_1m_2}{2rc^2},$$

the 1PN[8] order equations of motion become $d^2\vec{X}/dt^2 = 0$. (We use the 1PN corrections in this case because numerically, the Roemer time delay is quite large when we calculate it using classical Kepler's laws.)

Just as in the Newtonian case, for the 1PN system of equations, we end up with conservation of total angular momentum, $\vec{J}$, and total energy E. These conserved quantities allow us to find the first integrals of the equations of motion more easily and we arrive with

$$\left(\frac{dr}{dt}\right)^2 = A + \frac{2B}{r} + \frac{C}{r^2} + \frac{D}{r^3}$$

and

$$\frac{d\psi}{dt} = \frac{H}{r^2} + \frac{I}{r^3}.$$

The coefficients in the above solutions are

$$\begin{aligned}
A &= 2\varepsilon\left(1 + \frac{3}{2}(3\nu - 1)\frac{\varepsilon}{c^2}\right), \\
B &= Gm\left(1 + (7\nu - 6)\frac{\varepsilon}{c^2}\right), \\
C &= -j^2\left(1 + 2(3\nu - 1)\frac{\varepsilon}{c^2}\right) + (5\nu - 10)\frac{G^2m^2}{c^2}, \\
D &= (8 - 3\nu)\frac{GMj^2}{c^2}, \\
H &= j\left(1 + (3\nu - 1)\frac{\varepsilon}{c^2}\right), \\
I &= (2\nu - 4)\frac{GMj}{c^2}
\end{aligned}$$

where ε and $\vec{j}$ are the energy and angular momentum per unit value. Their

[8]Post-Newtonian (PN) theory is an approximation to the General Theory of Relativity in the domain of weak fields and slow motion. It combines an expansion in powers of G (to measure the strength of the field) with an expansion in powers of $1/c^2$ (to measure the velocity of the matter distribution) (Poisson & Will, 2014). Thus, 1PN is the lowest-order post-Newtonian correction that can be applied when the source is non-relativistic ($v/c \ll 1$), self-gravitating ($(R_s/d)^{1/2} \sim v/c$), and weakly stressed ($|T^{ij}|/T^{00} \sim \mathcal{O}(v^2/c^2)$).

explicit solutions are given by

$$\varepsilon = \frac{1}{2}v^2 - \frac{Gm}{r} + \frac{3}{8}(1-3\nu)\frac{v^4}{c^2} + \frac{Gm}{2rc^2}\left((3+\nu)v^2 + \nu(\hat{r}\cdot\vec{v})^2 - \frac{Gm}{r}\right)$$

and

$$\vec{j} = \left(1 + \frac{1}{2}(1-3\nu)\frac{v^2}{c^2} + (3+\nu)\frac{Gm}{rc^2}\right)\vec{r}\times\vec{v}$$

where $\vec{v}$ is the relative velocity and $\hat{r} = \vec{r}/r$.

Now, if we introduce other special variables, we can integrate the first-derivative equations to find the expression for the orbit in polar coordinates $(r(u), \psi(u))$, where $\psi(u)$ is the angle the pulsar is at with respect to the periastron.

Then, the Roemer delay is given by

$$\triangle_R = -\vec{x}_1 \cdot \hat{n}/c = r(u)\sin i \sin(\omega + \psi(u))$$

where ω and i are the angles of the periastron and inclination as shown in Figure 2.5.

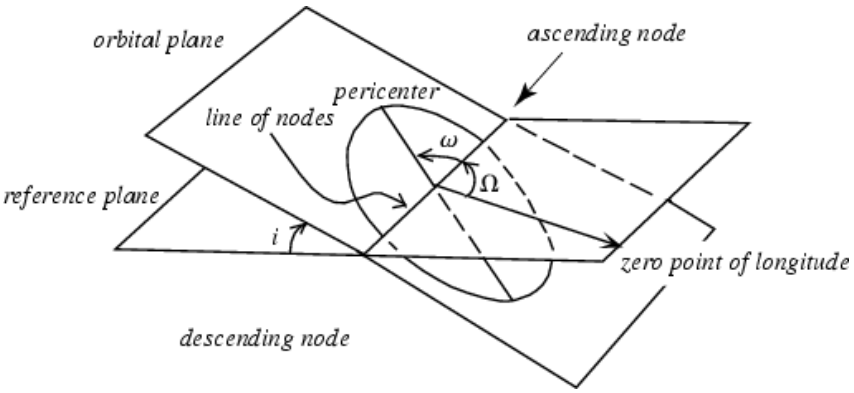

Figure 2.5: Geometry of the orbit with orbital parameters. The periastron of a binary system has been labeled as pericenter here. (Figure from Weisstein, 2018)

Then, we can use the 1PN solutions to end up with

$$\triangle_R = a_1 \sin i((\cos u - e_r)\sin\omega + (1-e_\theta^2)^{1/2}\sin u\cos\omega)$$

where a_1 is the semi-major axis of the pulsar and $e_r = (1 + \delta_r)e$ and $e_\theta = (1 + \delta_\theta)e$. Here, δ_r and δ_θ have the values

$$\delta_r = \frac{G}{c^2}\frac{3m_p^2 + 6m_p m_c + 2m_c^2}{a(m_p + m_c)}$$
$$\delta_\theta = \frac{G}{c^2}\frac{(7/2)m_p^2 + 6m_p m_c + 2m_c^2}{a(m_p + m_c)}.$$

Now, besides the Roemer time delay correction, we can also extract more information about the Hulse-Taylor binary by studying the 1PN solutions. The solution for $\psi(u)$ will show that the periastron does not advance uniformly along the orbit but at different rates according to u. Then, the derivative of ω averaged over the orbit gives us

$$\langle\dot{\omega}\rangle = \frac{3}{c^2}(G(m_p + m_c))^{2/3}\left(\frac{2\pi}{P_b}\right)^{5/3}\frac{1}{1 - e^2}$$

where using the measured values of e and P_b for the Hulse-Taylor binary (Taylor & Weisberg, 1982) gives

$$\langle\dot{\omega}\rangle = 2.11353\left(\frac{m_p + m_c}{M_\odot}\right)^{2/3} \text{ deg/yr}.$$

Therefore, if we measured $\langle\dot{\omega}\rangle$, we would have a way of knowing the total mass of the binary system.

Other Corrections

Though not covered in this dissertation, there is still a Shapiro time delay for the pulse as it feels the 'potential well' of the companion star. There must also be corrections due to the loss of energy from the binary as a result of gravitational-wave emission. This means that the orbit period P_b will ever so slightly decrease with time. However, because the Hulse-Taylor binary is quite relativistic, this effect can be and has been measured.

Two other corrections include an aberration correction and longitudinal Doppler shift correction. The aberration correction accounts for the fact that pulses arrive at Earth from different directions than was emitted as the pulsar orbits the binary center of mass. The longitudinal Doppler shift correction accounts for the proper motion of the SSB with respect to the binary center of mass. Thus, the period of the binary that is observed is not the intrinsic period of the binary. Then, we must study the relative acceleration of the SSB and the binary system caused by differential rotation of the Galaxy and correct the observed orbital period derivative for this Galactic acceleration.

Full Timing Formula and Results

In general, there are five Keplerian parameters that describe the orbital motion of the pulsar. They are

$$\{P_b, T_0, x, e, \omega\}$$

where P_b is the orbital period, T_0 is the time of passage at periastron, $x = (a/c)\sin i$ is the projected size of the orbit, e is the eccentricity, and ω is the longitude of periastron, as shown in Figure 2.5. A non-changing Keplerian orbit is what is predicted by Newtonian gravity.

There are also another eight post-Keplerian parameters which characterizes the corrections to the orbital motion of the pulsar. They are

$$\{\dot{\omega}, \gamma, \dot{P}_b, r, s, \delta_\theta, \dot{e}, \dot{x}\}$$

where the $\dot{}$s signify time derivatives of mentioned Keplerian parameters, γ is the Einstein parameter (Lorentz time dilation), $s = x(P_b/2\pi)^{-2/3}T_\odot^{-1/3}M^{2/3}m_2^{-1}$, and $r = T_\odot m_2$ where $T_\odot \equiv GM_\odot/c^3 = 4.925\ \mu$s. These post-Keplerian parameters are independently measurable.

And now, assuming that the General Theory of Relativity is correct, all eight of the post-Keplerian parameters are predicted once we know the value of the Keplerian parameters and the two masses of the stars in the binary. What this means is that if we can somehow extract the five Keplerian parameters and any two of the post-Keplerian parameters from the data, we can find the masses m_p and m_c. At this point, we would be able to find all of the other post-Keplerian parameters. Thus, an accurate fit of the observed time of arrivals to the timing formula is extremely important.

In the case of the Hulse-Taylor binary, it was possible to extract all five Keplerian parameters along with three post-Keplerian quantities $\langle\dot{\omega}\rangle$, γ, and $\dot{P}_b$. Then, using $\langle\dot{\omega}\rangle$ and γ, it was possible to determine m_p and m_c (see Figure 2.6) to check if the predicted value of $\dot{P}_b$ matched the corrected[9] observed value of $\dot{P}_b$, which it did.

Shown in Figures 2.6 and 2.7 are two famous diagrams from nearly three decades of observation at Arecibo. There is excellent agreement between the observed and predicted values of binary orbital period decay, $\dot{P}_b$, due to gravitational-wave emission. Thus, the Hulse-Taylor binary pulsar is historically important as giving the first experimental evidence for the existence of gravitational waves. For this work and "for the discovery of a new type of pulsar, a discovery that has opened up new possibilities for the study of gravitation", Hulse and Taylor were awarded the Nobel Prize in 1993.

[9]The observed value of $\dot{P}_b$ must be corrected by subtracting out the Galactic acceleration term, as mentioned previously in Subsection 2.4.

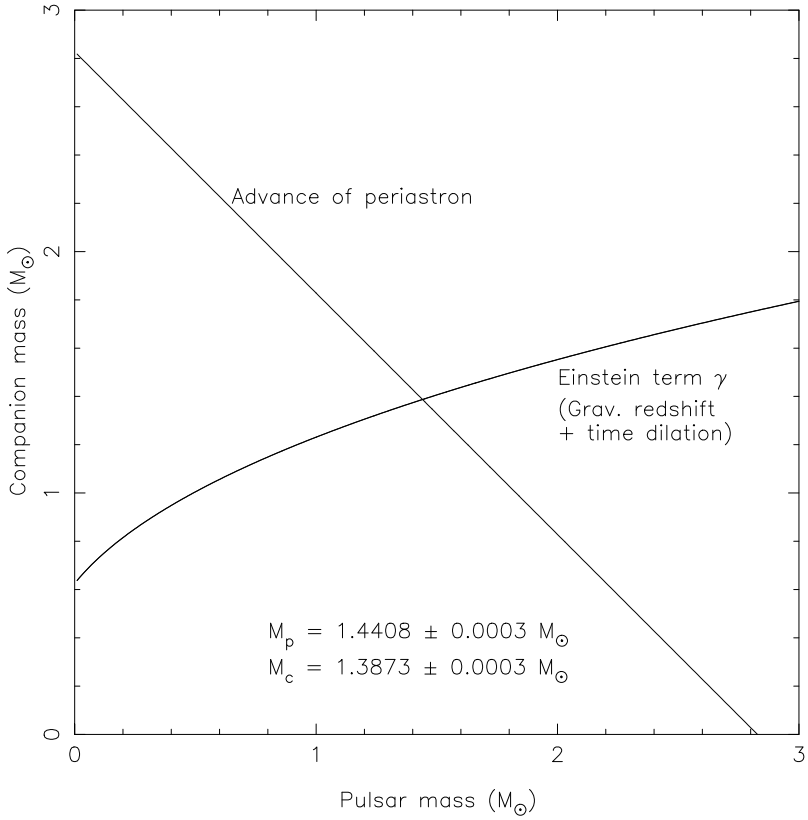

Figure 2.6: Constraints on the pulsar mass, m_p, and companion mass, m_c, from extracted values of $\langle\dot{\omega}\rangle$ and γ. (Figure from Weisberg & Taylor, 2002)

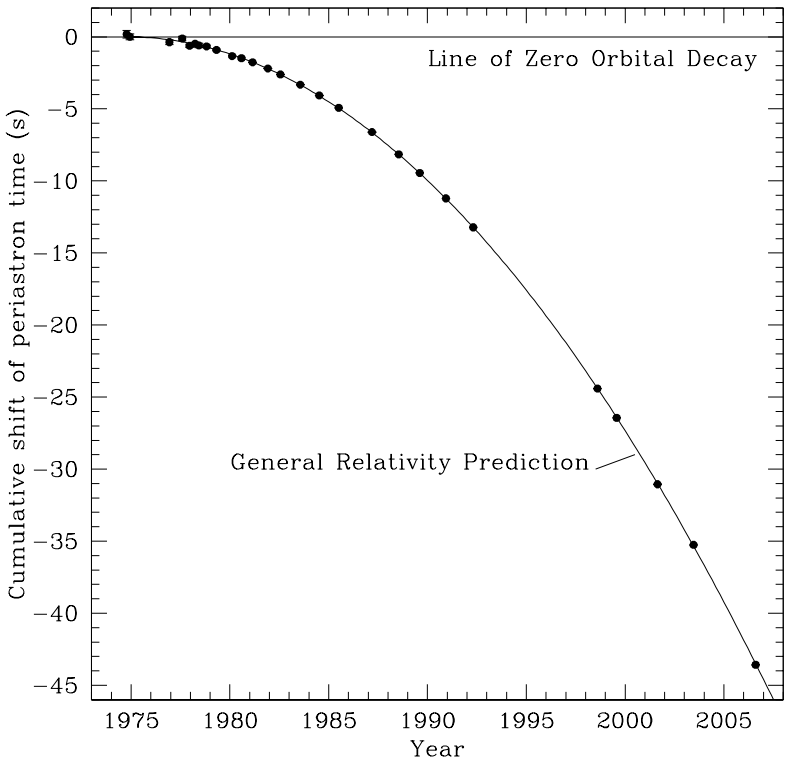

Figure 2.7: Orbital decay of PSR B1913+16. The data points represent measured orbital phase errors caused by assuming a fixed value of P_b that have been translated into cumulative shift of periastron time, in seconds. The parabola is the General Theory of Relativity prediction for the binary emitting gravitational waves. Error bars for data points are too small to see. (Figure from Weisberg et al., 2010)

Chapter 3

Advanced Ground-Based Laser Interferometric Gravitational-Wave Detectors

In this chapter I present the advanced ground-based gravitational-wave detectors, with a focus on the Advanced LIGO instruments. I capture the basic science of how these instruments operate and how detection is made possible. However, this requires an understanding of the fundamental and technical noise sources that must be accounted for and minimized. Thus, I also provide an in-depth look at the various noise sources.

3.1 A Simple Michelson interferometer

We can now capture the essential physics of how ground-based laser interferometric gravitational-wave detectors work (Figure 3.1). At the heart of one of these detectors is a Michelson interferometer, which acts as a transducer to convert differential displacements between freely-falling test mass mirrors into an optical signal. We will call $\omega_{\rm L}$, $k_{\rm L} = \omega_{\rm L}/c$, and $\lambda_{\rm L} = 2\pi/k_{\rm L}$ the frequency, wavenumber, and wavelength of the laser light[1].

Consider the input light electric field in the Michelson interferometer: $E_{\rm in} = E_0 e^{i(-\omega_{\rm L} t + \vec{k}_{\rm L}\cdot\vec{x})}$. Its reflection off and transmission through a 50-50 beamsplitter is described by the amplitude reflection coefficient, $r = 1/\sqrt{2}$, and amplitude transmission coefficient, $t = i/\sqrt{2}$. Thus, light that travels down the $\hat{x}$-arm of the detector has a field $i(E_0/\sqrt{2})e^{i(-\omega_{\rm L} t + k_{\rm L} x)}$ whereas light reflected

[1] In practice, both Advanced LIGO and Virgo use pre-stabilized 1064 nm Nd:YAG lasers.

Figure 3.1: From top to bottom, aerial views of Advanced LIGO/Hanford, Advanced LIGO/Livingston, and Advanced Virgo. (Figures from LIGO Laboratory/Virgo)

into the $\hat{y}$-arm has a field $(E_0/\sqrt{2})e^{i(-\omega_{\rm L}t+k_{\rm L}y)}$. When each field reflects off the end test mass mirrors located at $(L_x,\, 0)$ and $(0,\, L_y)$, the amplitudes are multiplied by -1. Thus, the fields in the $\hat{x}$- and $\hat{y}$-arms on their return path to the beamsplitter are: $-i(E_0/\sqrt{2})e^{i(-\omega_{\rm L}t+k_{\rm L}L_x)}$ and $-(E_0/\sqrt{2})e^{i(-\omega_{\rm L}t+k_{\rm L}L_y)}$. At last, when they reflect off and transmit through the beam splitter once more, we end with a final electric field at the photodetector of:

$$\begin{aligned}
E_{\rm out} &= -\frac{i}{2}E_0 e^{i(-\omega_{\rm L}t+2k_{\rm L}L_x)} - \frac{i}{2}E_0 e^{i(-\omega_{\rm L}t+2k_{\rm L}L_y)} \\
&= -\frac{i}{2}E_0 e^{-i\omega_{\rm L}t}\left[e^{ik_{\rm L}((L_x+L_y)+(L_x-L_y))} + e^{ik_{\rm L}((L_x+L_y)-(L_x-L_y))}\right] \\
&= -iE_0 e^{i(-\omega_{\rm L}t+k_{\rm L}(L_x+L_y))}\left(\frac{e^{ik_{\rm L}(L_x-L_y)} + e^{-ik_{\rm L}(L_x-L_y)}}{2}\right) \\
&= -iE_0 e^{i(-\omega_{\rm L}t+k_{\rm L}(L_x+L_y))}\cos(k_{\rm L}(L_x-L_y)).
\end{aligned}$$

Thus, the power output at the photodetector is proportional to:

$$|E_{\rm out}|^2 = E_0^2\cos^2(k_{\rm L}(L_x-L_y)),$$

and any variation in the detector arm lengths will result in a corresponding variation in the power output.

3.2 Interaction with Gravitational Waves in the Transverse Trace-Free Gauge

Independent of the choice of reference frame, the physical effect of incident gravitational waves on an interferometric detector can be seen by calculating the (invariant) roundtrip proper times as measured at the beamsplitter of two photons, one traveling up and down the $\hat{x}$-arm versus one traveling up and down the $\hat{y}$-arm. This calculation is simplest to do in the transverse trace-free gauge (introduced in Section 2.2) since the waves take on a very simple form (only $h_{ij} \neq 0$) and the coordinates of the freely falling mirrors and beamsplitter do not change.

First, we will analyze the situation for a plus-polarized gravitational wave propagating in the $\hat{z}$-direction:

$$h_+(t) = h_0 \cos(\omega_{\rm gw} t).$$

Then, the space-time interval in this reference frame is:

$$ds^2 = -c^2 dt^2 + (1 + h_+(t))dx^2 + (1 - h_+(t))dy^2 + dz^2.$$

Thus, for a photon traveling up and down the $\hat{x}$-arm starting at time t_0, we have:

$$\begin{aligned} 0 = ds^2 &= -c^2 dt^2 + (1 + h_+(t))dx^2 \\ dx &= \pm\ cdt\ (1 + h_+(t))^{-1/2} \\ &\approx \pm\ cdt\ (1 - \frac{1}{2}h_+(t)), \end{aligned}$$

which leads to:

$$\begin{aligned} \int_0^{L_x} dx = c\int_{t_0}^{t_1} 1 - \frac{1}{2}h_+(t)dt &= -c\int_{t_2}^{t_1} 1 - \frac{1}{2}h_+(t)dt \\ L_x = c(t_1 - t_0) - \frac{c}{2}\int_{t_0}^{t_1} h_+(t)dt &= c(t_2 - t_1) - \frac{c}{2}\int_{t_1}^{t_2} h_+(t)dt \\ 2L_x = c(t_2 - t_0) - \frac{c}{2}\int_{t_0}^{t_2} h_+(t)dt & \\ t_2 - t_0 = \frac{2L_x}{c} + \frac{1}{2}\int_{t_0}^{t_2} h_+(t)dt & \end{aligned}$$

. Thus, to order $\mathcal{O}(h_0)$ we have:

$$\begin{aligned} t_2 - t_0 &= \frac{2L_x}{c} + \frac{1}{2}\int_{t_0}^{t_0+2L_x/c} h_0 \cos(\omega_{\rm gw} t)dt \\ &= \frac{2L_x}{c} + \frac{h_0}{2\omega_{\rm gw}}\left(\sin(\omega_{\rm gw}(t_0 + 2L_x/c)) - \sin(\omega_{\rm gw} t_0)\right) \\ &= \frac{2L_x}{c} + \frac{L_x}{c}\frac{\sin(\omega_{\rm gw} L_x/c)}{(\omega_{\rm gw} L_x/c)} h_0 \cos\left(\omega_{\rm gw}\left(t_0 + \frac{L_x}{c}\right)\right) \\ &= \frac{2L_x}{c} + \frac{L_x}{c} h(t_0 + L_x/c)\ \mathrm{sinc}(\omega_{\rm gw} L_x/c), \end{aligned}$$

where we have used the identity $\sin(\alpha + 2\beta) - \sin\alpha = 2\sin\beta\cos(\alpha + \beta)$.

The same calculation for the $\hat{y}$-arm gives:

$$t_2 - t_0 = \frac{2L_y}{c} - \frac{L_y}{c} h(t_0 + L_y/c)\ \mathrm{sinc}(\omega_{\mathrm{gw}} L_y/c).$$

Because $\mathrm{sinc}(x)$ goes to 1 as x goes to 0, in the scenario where the frequency of the gravitational wave is small, i.e., the period of gravitational wave is large compared to $t_1 \approx L_x/c \approx L_y/c$, the correction to the roundtrip time becomes adding $L_x h(t_1)/c$ or subtracting $L_y h(t_1)/c$. Likewise, because $\mathrm{sinc}(x)$ goes to 0 as x approaches ∞, if $\omega_{\mathrm{gw}} L_x/c$ or $\omega_{\mathrm{gw}} L_y/c \gg 1$, the correction to the roundtrip time becomes suppressed.

Now, we wish to find the ideal length of the detector arms. To do this, we turn back to the total electric field at the photodetector:

$$\begin{aligned} E_{\mathrm{out}} &= -\frac{i}{2} E_0 e^{i(-\omega_{\mathrm{L}} t + 2k_{\mathrm{L}} L_x) + i\Delta\phi_x(t)} - \frac{i}{2} E_0 e^{i(-\omega_{\mathrm{L}} t + 2k_{\mathrm{L}} L_y) + i\Delta\phi_y(t)} \\ &= -\frac{i}{2} E_0 e^{-i\omega_{\mathrm{L}}(t - 2L_x/c) + i\Delta\phi_x(t)} - \frac{i}{2} E_0 e^{-i\omega_{\mathrm{L}}(t - 2L_y/c) + i\Delta\phi_y(t)} \end{aligned}$$

where $\Delta\phi_x(t)$ and $\Delta\phi_y(t)$ are to order $\mathcal{O}(h_0)$:

$$\begin{aligned} \Delta\phi_x(t) &= \omega_{\mathrm{L}} \frac{L_x}{c}\ \mathrm{sinc}(\omega_{\mathrm{gw}} L_x/c) h_0 \cos\left(\omega_{\mathrm{gw}}\left(t_0 + \frac{L_x}{c}\right)\right) \\ &= \omega_{\mathrm{L}} \frac{L_x}{c}\ \mathrm{sinc}(\omega_{\mathrm{gw}} L_x/c) h_0 \cos\left(\omega_{\mathrm{gw}}\left(t - \frac{L_x}{c}\right)\right) \\ \Delta\phi_y(t) &= -\omega_{\mathrm{L}} \frac{L_y}{c}\ \mathrm{sinc}(\omega_{\mathrm{gw}} L_y/c) h_0 \cos\left(\omega_{\mathrm{gw}}\left(t_0 + \frac{L_y}{c}\right)\right) \\ &= -\omega_{\mathrm{L}} \frac{L_y}{c}\ \mathrm{sinc}(\omega_{\mathrm{gw}} L_y/c) h_0 \cos\left(\omega_{\mathrm{gw}}\left(t - \frac{L_y}{c}\right)\right). \end{aligned}$$

By introducing $L = (L_x + L_y)/2$ and $\phi_0 = k_{\rm L}(L_x - L_y)$, we get:

$$\begin{aligned}
E_{\rm out} &= -\frac{i}{2}E_0 e^{-i\omega_{\rm L}(t-2L_x/c)+i\Delta\phi_x(t)} - \frac{i}{2}E_0 e^{-i\omega_{\rm L}(t-2L_y/c)+i\Delta\phi_y(t)} \\
&= -\frac{i}{2}E_0 e^{-i\omega_{\rm L}(t-(2L+(L_x-L_y))/c)+i\Delta\phi_x(t)} - \frac{i}{2}E_0 e^{-i\omega_{\rm L}(t-(2L-(L_x-L_y))/c)+i\Delta\phi_y(t)} \\
&= -iE_0 e^{-i\omega_{\rm L}(t-2L/c)}\left(\frac{e^{i\phi_0+i\Delta\phi_x(t)} + e^{-i\phi_0+i\Delta\phi_y(t)}}{2}\right) \\
&\approx -iE_0 e^{-i\omega_{\rm L}(t-2L/c)}\left(\frac{e^{i\phi_0+i\Delta\phi(t)} + e^{-i\phi_0-i\Delta\phi(t)}}{2}\right) \\
&= -iE_0 e^{-i\omega_{\rm L}(t-2L/c)}\cos(\phi_0 + \Delta\phi(t))
\end{aligned}$$

where

$$\begin{aligned}
\Delta\phi(t) &= \omega_{\rm L}\frac{L}{c}\ \mathrm{sinc}(\omega_{\rm gw}L/c)h_0\cos\left(\omega_{\rm gw}\left(t-\frac{L}{c}\right)\right) \\
&= |\Delta\phi(t)|\cos(\omega_{\rm gw}t+\alpha).
\end{aligned}$$

To maximize the phase difference in the interferometer, we need to maximize $\Delta\phi(t)$. Thus, we focus on the $\sin(\omega_{\rm gw}L/c)$ term in the $\mathrm{sinc}(\omega_{\rm gw}L/c)$ function. Then, the smallest value that L could be is:

$$\begin{aligned}
L &= \frac{\pi c}{2\omega_{\rm gw}} \\
&= \frac{c}{4f_{\rm gw}} \\
&= 750\ \mathrm{km}\left(\frac{100\ \mathrm{Hz}}{f_{\rm gw}}\right).
\end{aligned}$$

Thus, detector arm lengths $\sim$750 km are ideal for detecting gravitational waves with frequencies $\sim$100 Hz. This is achieved with the use of Fabry-Pérot cavities to make the photons bounce back and forth many times in each arms before recombining. Roughly this equates to $\mathcal{O}(100)$ bounces because Advanced LIGO's and Advanced Virgo's arms are 4 km and 3 km long. For Advanced LIGO, Fabry-Pérot cavities enhance the storage time of light and sensitivity to a phase shift by factors of $\mathcal{F}/(2\pi)$ and $2\mathcal{F}/\pi$, where $\mathcal{F} = 450$ is the finesse.

It is important to note that for each of the reflected electric fields that make up E_{out}, the effect of the gravitational wave (to order h_0) is to create sidebands of frequencies $\omega_{\text{L}} \pm \omega_{\text{gw}}$, where the modulus of the amplitude is $|\Delta\phi(t)|/2$. For instance, if we look at the field in the $\hat{x}$-arm:

$$\begin{aligned} E^{(x)}(t) &\approx -\frac{i}{2} E_0 e^{-i\omega_{\text{L}}(t-2L/c)} e^{i\phi_0 + i\Delta\phi(t)} \\ &= -\frac{i}{2} E_0 e^{-i\omega_{\text{L}}(t-2L/c)+i\phi_0} (1 + i|\Delta\phi(t)| \cos(\omega_{\text{gw}} t + \alpha)) \\ &= -\frac{i}{2} E_0 e^{i\beta} \left[e^{-i\omega_{\text{L}} t} + \frac{i}{2}|\Delta\phi(t)| e^{i\alpha} e^{-i(\omega_{\text{L}}-\omega_{\text{gw}})t} + \frac{i}{2}|\Delta\phi(t)| e^{-i\alpha} e^{-i(\omega_{\text{L}}+\omega_{\text{gw}})t} \right], \end{aligned}$$

where $\beta = \phi_0 + \omega_{\text{L}} 2L/c$ is an irrelevant constant phase.

3.3 Advanced Detectors

Aside from Fabry-Pérot cavities, ground-based interferometric gravitational-wave detectors also use power recycling and signal recycling mirrors to enhance the basic Michelson-Morley setup (Figure 3.2).

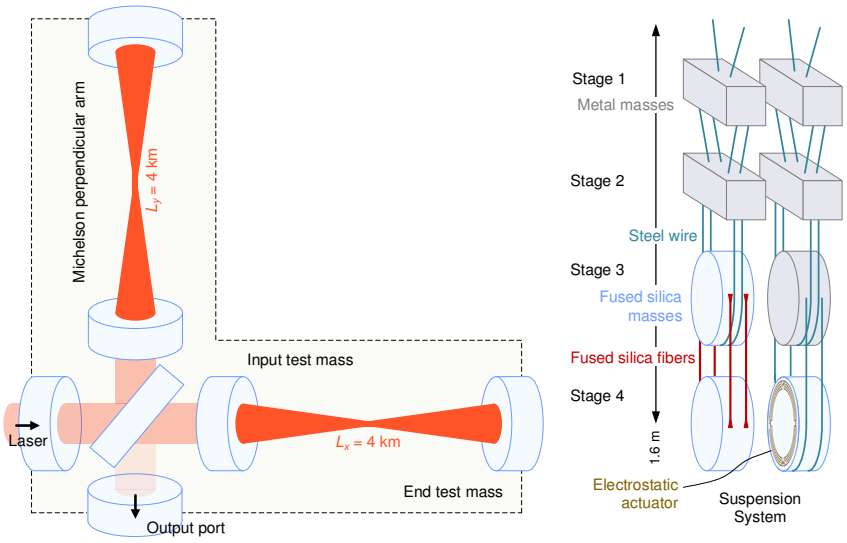

Figure 3.2: Advanced LIGO's Michelson-Morley interferometer with the power recycling mirror (placed between the laser and beamsplitter), Fabry-Pérot cavities making up the 4 km arms, and signal recycling mirror (placed between the beamsplitter and photodetector). The test mass setup shows the main chain side (left) and the reaction chain side (right). (Figure from Abbott et al., 2016)

The signal recycling mirror is placed between the beamsplitter and the photodetector such that the signal recycling cavity is seen only by the signal sidebands and the circulating laser power in the interferometer is not affected. The combination of the signal recycling mirror and each input test mass mirror can be thought of as an "equivalent input test mass mirror" for the Fabry-Pérot cavities. Depending on slight adjustments (of order fractions of λ_L) to the position of the signal-recycling mirror, the reflectivities of the equivalent input test mass mirrors and consequently, the detector response to gravitational waves varies. Thus, the signal recycling tuning, $\phi = k_L l_{SRC} + \pi/4$, determines the detector mode of operation (Figure 3.3). Here, the length of the signal recycling cavity length[2], l_{SRC}, is the sum of the distance from the beamsplitter to the signal recycling mirror plus the average of the distances from the beamsplitter to each Fabry-Pérot cavity.

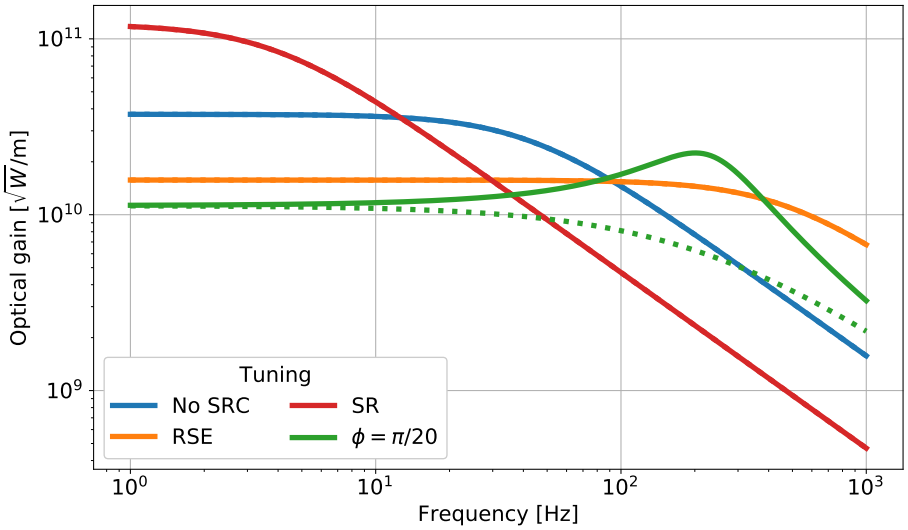

Figure 3.3: Broadband (orange) to narrowband (red) detector responses depending on signal recycling mirror tunings, ϕ. Dashed/solid lines are for lower/upper frequency sidebands. (Figure from Gabriele Vajente, 2018)

When $\phi = 0$, the reflectivity of the equivalent input test mass mirrors is

[2]For Advanced LIGO, $l_{SRC} = 56.0$ m (Izumi & Sigg, 2017).

the lowest possible, i.e., the signal recycling cavity is tuned to anti-resonance, and the Fabry-Pérot cavity bandwidth is increased (the finesse decreased). This technique, known as resonant sideband extraction (RSE), is shown in orange in Figure 3.3. The broadband configuration is well-suited for detecting signals from compact binary coalescences where the gravitational-wave frequencies evolve and are unknown until after they happen.

When $\phi = \pi/2$, the equivalent input test mass mirror reflectivity is high and the signal recycling cavity is in resonance with a sideband for a specific $\omega_{\rm gw}$. The resulting detector bandwidth is decreased (the finesse increased). This is simply known as the signal recycling mode (SR) and is shown in red in Figure 3.3. The narrowband configuration is better suited for detecting periodic signals from pulsars, for example, where the gravitational-wave frequency can be derived from the angular frequency ($\omega_{\rm gw} = 2\omega_{\rm rot}$) and is already known.

Next, the power recycling mirror will be discussed in context of the shot noise. There are two large classes of persistent noise sources for ground-based interferometric gravitational-wave detectors (Figure 3.4): fundamental noise (of which there are two sub-classes: displacement versus sensing) and technical noise (of which there are hundreds). The range referred to in the figure caption is defined as the sky-averaged distance at which the astrophysical event gives a matched filter signal-to-noise ratio of 8 in a single detector. In the next section, we will focus on the fundamental noise sources.

3.4 The Noise Power Spectral Density

The output of Advanced LIGO or Virgo is a time series that describes the phase shift of laser light, $s(t)$, composed of the gravitational-wave signal (when present) and noise. If we think of the GW detector as a linear system black box, an input gravitational-wave signal $h(t)$ produces an output (in the

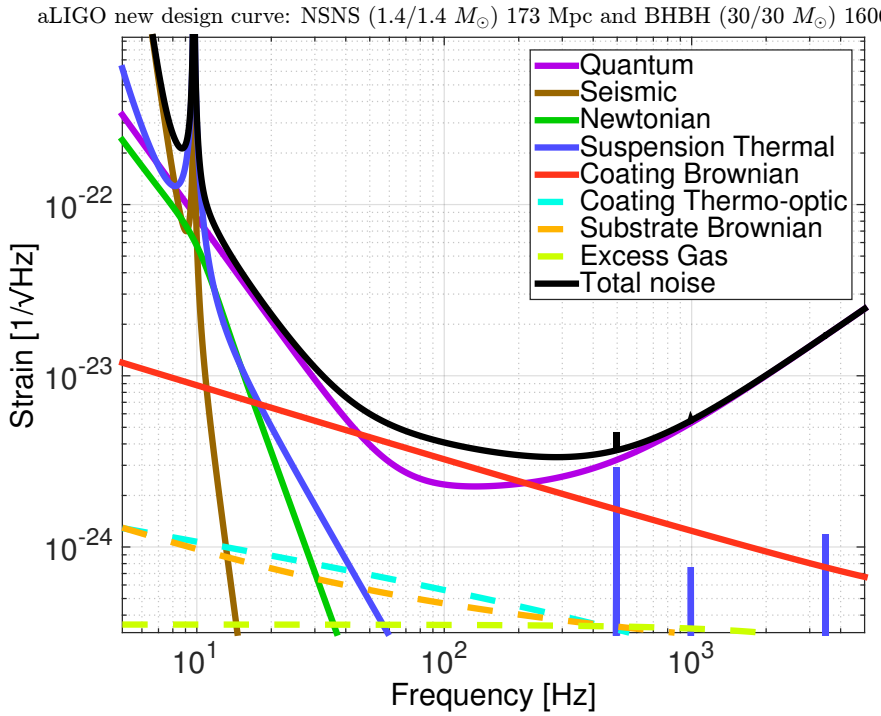

Figure 3.4: Advanced LIGO's design sensitivity curve, $S_n^{1/2}(f)$. The symmetric binary 1.4 $M_\odot$ neutron star and symmetric binary 30 $M_\odot$ black hole coalescence ranges are 173 Mpc and 1606 Mpc, respectively. (Figure from Barsotti et al., 2018)

absence of noise):

$$\tilde{h}_{\rm out}(f) = T(f)\tilde{h}(f)$$

in frequency space, where $T(f)$ is the detector transfer function and tildes represent Fourier transforms.

Similarly, the total noise output is related to a fictitious noise input[3] via:

$$\tilde{n}(f) = T^{-1}(f)\tilde{n}_{\rm out}(f).$$

Because the noise input varies from one realization of the detector to the next, $n(t)$ is a random time series that can be characterized by its auto-

[3] A fictitious noise $n(t)$ injected into the detector black box (with no other noise generated in the detector) would produce an output noise $n_{\rm out}(t)$.

correlation function:

$$n * n(\tau) = \langle n(t)n(t+\tau)\rangle = \int_{-\infty}^{\infty} n(t)n(t+\tau)dt,$$

which measures the relatedness of the noise at various time offsets τ to itself. The Fourier transform of the auto-correlation function gives us the single-sided power spectral density (PSD), $S_n(f)$, via:

$$S_n(f) = \begin{cases} \frac{2}{\sqrt{2\pi}} \int_{-\infty}^{\infty} n * n(\tau) e^{-i2\pi f\tau} d\tau & \text{if f} \geq 0, \\ 0 & \text{otherwise.} \end{cases}$$

The interpretation of the noise power spectral density can then be found by taking the inverse Fourier transform:

$$n * n(\tau) = \langle n(t)n(t+\tau)\rangle = \frac{1}{2}\int_{-\infty}^{\infty} S_n(f) e^{i2\pi f\tau} df$$

and evaluating at zero time offset:

$$\langle n^2(t)\rangle = \int_0^{\infty} df\, S_n(f).$$

Thus, the noise PSD reveals frequency-dependent contributions to the noise.

Optical Read-Out Noise

The general shape of Advanced LIGO's design sensitivity curve, the amplitude spectral density $S_n^{1/2}(f)$, is determined by the optical read-out noise, i.e., the quantum noise depicted by the purple line in Figure 3.4. The optical read-out noise is a fundamental noise source that combines radiation pressure (which dominates at lower gravitational-wave frequencies and manifests as a displacement noise) with shot noise (which is frequency-independent up to a pole frequency and manifests as a sensing noise). Their power spectral densities are combined as follows:

$$S_n(f)|_{\text{opt}} = S_n(f)|_{\text{shot}} + S_n(f)|_{\text{rp}}$$

The shot noise power spectral density for a simple Michelson-Morley interferometer can be derived as follows. The total power arriving at the photodetector depends on the number of photons that arrive, N_γ, during an observation time T:

$$P = \frac{1}{T} N_\gamma \hbar\omega_{\mathrm{L}},$$

where $\hbar\omega_{\mathrm{L}}$ is the energy per photon and N_γ follows the Poisson distribution:

$$p(N_\gamma; \bar{N}_\gamma) = \frac{1}{N_\gamma!} \bar{N}_\gamma{}^{N_\gamma} e^{-\bar{N}_\gamma},$$

where $\bar{N}_\gamma$ is the average value of N_γ. Because $N_\gamma \gg 1$, the Poisson distribution becomes a Gaussian distribution with standard deviation $\sqrt{N_\gamma}$. Then, the fluctuation in the power is given by:

$$\begin{aligned}(\Delta P)_{\mathrm{shot}} &= \frac{1}{T} N_\gamma^{1/2} \hbar\omega_{\mathrm{L}} \\ &= \left(\frac{\hbar\omega_{\mathrm{L}}}{T} P\right)^{1/2}.\end{aligned}$$

If there is no gravitational wave, we can write this as:

$$(\Delta P)_{\mathrm{shot}} = \left(\frac{\hbar\omega_{\mathrm{L}}}{T} P_0\right)^{1/2} |\cos\phi_0|,$$

where the output power, P, is related to the input power, P_0, by $P = P_0 \cos^2\phi_0$ (Section 3.1). However, in the presence of a purely plus-polarized gravitational wave, the phase is shifted by a factor $2\Delta\phi(t)$ (Section 3.2), which in the limit $\omega_{\mathrm{gw}} L/c \ll 1$, is:

$$2\Delta\phi(t) = \frac{4\pi L}{\lambda_{\mathrm{L}}} h_0,$$

giving us a fluctuation in the output power:

$$\begin{aligned}(\Delta P)_{\mathrm{gw}} &\approx P_0 \sin(2\phi_0) \Delta\phi(t) \\ &= P_0 \sin(2\phi_0) \frac{2\pi L}{\lambda_{\mathrm{L}}} h_0.\end{aligned}$$

Then, the signal-to-noise ratio (SNR) can be calculated:

$$\begin{aligned}\mathrm{SNR} &= \frac{(\Delta P)_{\mathrm{gw}}}{(\Delta P)_{\mathrm{shot}}} \\ &= P_0 \sin(2\phi_0)\frac{2\pi L}{\lambda_{\mathrm{L}}} h_0 \left(\frac{\hbar\omega_{\mathrm{L}}}{T}P_0\right)^{-1/2} |\cos\phi_0|^{-1} \\ &= \left(\frac{P_0 T}{\hbar\omega_{\mathrm{L}}}\right)^{1/2} \frac{4\pi L}{\lambda_{\mathrm{L}}} h_0 |\sin\phi_0|,\end{aligned}$$

and written in terms of the amplitude spectral density using the relation:

$$\mathrm{SNR} = \left(\frac{T}{S_n(f)}\right)^{1/2} h_0,$$

which applies for optimally oriented periodic signals.

Thus, we arrive at the strain sensitivity due to the shot noise:

$$S_n^{1/2}(f)\big|_{\mathrm{shot}} = \frac{\lambda_{\mathrm{L}}}{4\pi L}\left(\frac{\hbar\omega_L}{P_0}\right)^{1/2} \frac{1}{|\sin\phi_0|},$$

and see that for a simple Michelson-Morley interferometer, indeed, it is independent of the frequency of the gravitational waves[4]. Thus, to lower the shot noise, we need to increase the input laser power. This is achieved with a power recycling mirror which is placed between the laser and the beamsplitter to reflect light back towards the beamsplitter, increasing the circulating laser power in the Fabry-Pérot cavities[5]. During the first Advanced LIGO Observing Run, O1, only 20 W were injected into the interferometer, which was amplified up to 100 kW with the use of power recycling mirrors (Abbott et al.,

[4]In reality, the shot noise amplitude spectral density is frequency-independent up to the pole frequency, $f_p = 1/4\pi\tau_s$ (where τ_s is the storage time of the Fabry-Pérot cavities), and then rises linearly. This frequency dependence arises from the interferometer with Fabry-Pérot cavities transfer function:

$$T_{\mathrm{FP}} \simeq \frac{8\mathcal{F}L}{\lambda_{\mathrm{L}}} \frac{1}{\sqrt{1+(f_{\mathrm{gw}}/f_p)^2}},$$

which alters the SNR.

[5]The power recycling cavity length, l_{p}, is the sum of the distance from the beamsplitter to the power recycling mirror plus the average of the distances from the beamsplitter to each Fabry-Pérot cavity. For Advanced LIGO, $l_{\mathrm{p}} = 57.65$ m (Izumi & Sigg, 2017).

2016). At design sensitivity, the goal is to inject 125 W into the interferometer and increase the circulating power up to ∼750 kW, lowering the shot noise by a factor of ∼2.7.

The other contribution to the optical read-out noise is radiation pressure, a displacement noise from photons pushing on the mirrors during each reflection. A photon of energy $E_\gamma = |\mathbf{p}|c$ changes its momentum from $+\mathbf{p}$ to $-\mathbf{p}$, transferring a total momentum $2|\mathbf{p}| = 2E_\gamma/c$ to the mirrors. Thus, the force exerted on the mirrors is $F = 2P/c$. However, due to fluctuations in the number of photon arrivals in a laser beam, there is also a fluctuation in the overall force in a time T, given by:

$$\begin{aligned}\Delta F &= 2\Delta P/c \\ &= 2\sqrt{\frac{\hbar\omega_{\mathrm{L}}P}{c^2T}},\end{aligned}$$

which is independent of the gravitational-wave frequency.

The power spectral density of the fluctuations in this force, $S_{\Delta F}$, can be calculated from the general relation:

$$\langle \Delta F(t)\Delta F(t')\rangle = \frac{1}{2}\int_{-\infty}^{\infty} S_{\Delta F}(f)e^{i2\pi f(t-t')}df,$$

where we already know that it must be independent of the gravitational-wave frequency. Thus, in a time T we have:

$$\langle \Delta F^2(t)\rangle = \frac{1}{2T}S_{\Delta F},$$

resulting in the amplitude spectral density of the fluctuations in the force:

$$S_{\Delta F}^{1/2} = 2\sqrt{\frac{2\hbar\omega_{\mathrm{L}}P}{c^2}}.$$

However, because we are ultimately interested in the displacements, x, in the mirror, we use the relations:

$$F(t) = M\ddot{x},$$
$$\widetilde{F}(f) = -M(2\pi f)^2\widetilde{x},$$

giving us:

$$S_x^{1/2}(f) = \frac{2}{M(2\pi f)^2}\sqrt{\frac{2\hbar\omega_{\rm L}P}{c^2}}.$$

For a simple Michelson-Morley interferometer[6], the transfer function that relates ΔL to the gravitational-wave amplitude, h, is just L, thus the amplitude spectral density from radiation pressure is:

$$S_n^{1/2}(f)\big|_{\rm rp} = \frac{2}{ML(2\pi f)^2}\sqrt{\frac{2\hbar\omega_{\rm L}P}{c^2}},$$

which dominates at lower frequencies. As can be seen, there is a trade-off in increasing the laser power to lower the shot noise ($\propto 1/\sqrt{P}$) at lower frequencies, because radiation pressure noise is proportional to $\sqrt{P}$.

Seismic Noise

The seismic noise is a displacement noise caused by the continuous motion of the Earth's ground. This could be due to natural phenomena (e.g., winds, earthquakes, waves crashing on the shore, etc.) or human activity (e.g., nearby traffic, trains, commercial logging, and more). To keep the test mass mirrors as still as possible, there are both passive and active vibration isolation systems in place.

The passive isolation system consists of suspending the test mass mirror within a quadruple pendulum system[7]. The idea here is that at each stage of

[6]For Fabry-Pérot cavities, the equivalent length of the detector arms as a simple Michelson-Morley interferometer is $2\mathcal{F}L/\pi$.

[7]Advanced LIGO uses 40 kg test mass mirrors suspended within a 360 kg quadruple pendulum system using both steel and fused silica fibers (Figure 3.2).

suspension, the motion of the suspended mass is smaller than the motion of the suspension point above the pendulum resonant frequency. More formally, a mass suspended from a pendulum with a resonant frequency f_0 shaking at frequencies $f \gg f_0$, experiences an attenuation in its displacement of factor $(f/f_0)^2$, compared to if it were not suspended from the pendulum. We are only hoping to target signals at frequencies above 10 Hz because most of the Earth's seismic noise occurs between $1-10$ Hz. If each pendulum has a resonant frequency of 1 Hz, using a quadruple pendulum system isolates the vibration in the xy-plane of the test mass mirror $\sim 10^8$ times at 10 Hz. Consequently, the seismic noise drops off dramatically above 10 Hz (Figure 3.4).

The active isolation system consists of two parts: an internal seismic isolation platform (ISI) from which the quadruple pendulum system is hung and the reaction chain side to the test mass setup (Figure 3.2). At low frequencies, pendulums do not help with vibration isolation and therefore, the seismic isolation platform acts as the first line of defense. Vertical motion is controlled via springs made with steel cantilevers in the seismic isolation platform. Finally, electrostatic or coil/magnet actuators on the reaction chain side push and pull on the test mass mirrors to counteract other ground motions.

Newtonian Noise

The Newtonian noise, also known as the gravity gradient noise, dominates at lower frequencies ($\lesssim 30$ Hz) and is caused by the coupling of Earth's changing gravitational field with the test mass mirrors. Motion from all nearby objects, even atmospheric turbulence, creates a non-negligible contribution to the Newtonian noise.

Suspension Thermal Noise

Suspension thermal noise is caused by thermodynamic interactions between the pendulums and their surroundings. These interactions cause thermal fluctuations which induce horizontal and vertical motions in the test mass mirrors, affecting the sensitivity of the detectors up to ∼60 Hz. There are also the violin modes, depicted by blue spikes starting around 500 Hz in Figure 3.4. These violin modes are due to fluctuations in the normal modes of the fused silica fiber wires used to suspend the mirrors.

Coating Thermo-Optic and Brownian/Substrate Brownian Noise

Each test mass mirror has a multi-layered dielectric coating, alternating between low and high refractive index materials[8] to make the mirrors highly reflective. When the temperature of the mirrors or their surrounding environment fluctuates, the coating materials expand or contract, altering their refractive indices. Thus, thermal noise due to thermal dissipation is known as the coating thermo-optic noise.

Temperature fluctuations also alter the thickness of the coating material layers and substrate[9], resulting in their shear and bulk losses. Thermal noise due to mechanical loss is called the coating and substrate Brownian noise.

Excess Gas Noise

Excess gas noise, also known as the residual gas noise, is caused by photons scattering off any residual gas molecules in the ultra-high vacuum (∼10^{-7} Pa) pipes that make up the detector arms. Furthermore, the residual gas must be free of hydrocarbons in order to keep the optical surfaces clean.

[8] Advanced LIGO uses silica (SiO_2), tantala (Ta_2O_5), and titania-doped tantala (Ta_2O_5-TiO_2), with refractive indices 1.45, 2.03, and 2.07.

[9] The substrate is the material beneath the coating that makes up the test mass mirrors. Advanced LIGO mirror substrates are fused silica; KAGRA will use sapphire.

3.5 Interferometer Antenna Response

All gravitational-wave detectors are more like microphones rather than telescopes, where detector sensitivities depend on propagation directions and polarizations of incident gravitational waves. Typically, the sensitivity of a single detector is measured by its horizon distance (i.e., the maximum distance at which a compact binary GW source creates a maximum fiducial single-detector SNR, ρ, of 8[10]):

$$d_{\rm horizon} \approx \frac{G^{5/6} M^{1/3} \mu^{1/2}}{c^{3/2} \pi^{2/3} \rho} \sqrt{\frac{5}{6} \int_{f_1}^{f_2} \frac{f^{-7/3}}{S_n(f)} df},$$

where G is Newton's gravitational constant, c is the speed of light, M is $m_1 + m_2$ (the sum of the component masses), μ is the reduced mass, $f^{-7/3}$ is the approximate PSD of the inspiral signal, and the integral takes place from f_1 being the low-frequency limit of the detector's frequency band. However, the sensitivity of a detector can also be measured by its range, (i.e., the volume and orientation averaged distance of the source detected with SNR $= \rho$). It is a factor of $\sim$2.26 smaller than the horizon distance due to the detector's directional sensitivities (Schutz, 2011) which we will now set out to derive.

In the weak-field limit where gravitational waves can be neatly separated from the Minkowski background as metric perturbations (Section 2.2), the waves are solutions to the wave equation:

$$\left(\nabla^2 - \frac{1}{c^2} \frac{\partial^2}{\partial t^2} \right) h_{\mu\nu} = 0,$$

with $h_{\mu\nu}$ as a function of $t - \vec{k}' \cdot \vec{r}/c$ representing plane waves propagating at speed c in the $\hat{k}'$-direction. In general then, we can construct two tensors, $\overleftrightarrow{e}_+$ and $\overleftrightarrow{e}_\times$, from any two unit vectors, $\hat{i}'$ and $\hat{j}'$, that make an orthonormal triple

[10] The maximum single-detector SNR, ρ, is set to 8 to give a root-sum-squared 2-detector GW network SNR of $\rho_{\rm net} = 8\sqrt{2} \approx 11.313$.

with $\hat{k}'$:

$$\overleftrightarrow{e}_+ = \hat{i}' \otimes \hat{i}' - \hat{j}' \otimes \hat{j}'$$
$$\overleftrightarrow{e}_\times = \hat{i}' \otimes \hat{j}' + \hat{j}' \otimes \hat{i}',$$

such that

$$\overleftrightarrow{h} = h_+ \overleftrightarrow{e}_+ + h_\times \overleftrightarrow{e}_\times.$$

Now, there are two coordinate systems that are 'natural' to describe the situation. The first coordinate system is the gravitational-wave propagation frame (x', y', z') with $\hat{k}'$ in the direction of the propagating gravitational wave (from source towards detector), and two unit vectors, $\hat{i}'$ and $\hat{j}'$, that make an orthonormal triple with $\hat{k}'$. The second coordinate system is in the reference frame of the detector, (x, y, z), with two unit vectors, $\hat{i}$ and $\hat{j}$, that lie along the directions of the detector arms with the third unit vector uniquely defined by the cross product. Then, using the right ascension, declination, the orientation angle to identify $\hat{i}'$ and $\hat{j}'$, the coordinates of the detector (latitude, longitude, elevation), and the orientation angle to identify $\hat{i}$ and $\hat{j}$, we can find the Euler angles (Figure 3.5), (φ, θ, ψ), to switch between the two reference frames.

Once the Euler angles are found, the gravitational-wave strain on the detector can be computed in a straightforward fashion, assuming that the light travel time of the photons in the detector arms is short compared to the period of the gravitational wave[11]:

$$\begin{aligned} h &= \overleftrightarrow{h} : \overleftrightarrow{d} \\ &= (h_+ \overleftrightarrow{e}_+ + h_\times \overleftrightarrow{e}_\times) : \overleftrightarrow{d} \\ &= h_+ F_+ + h_\times F_\times, \end{aligned}$$

[11] The : notation is for calculating the trace: $\overleftrightarrow{S} : \overleftrightarrow{T} = S_{ab} T^{ba}$.

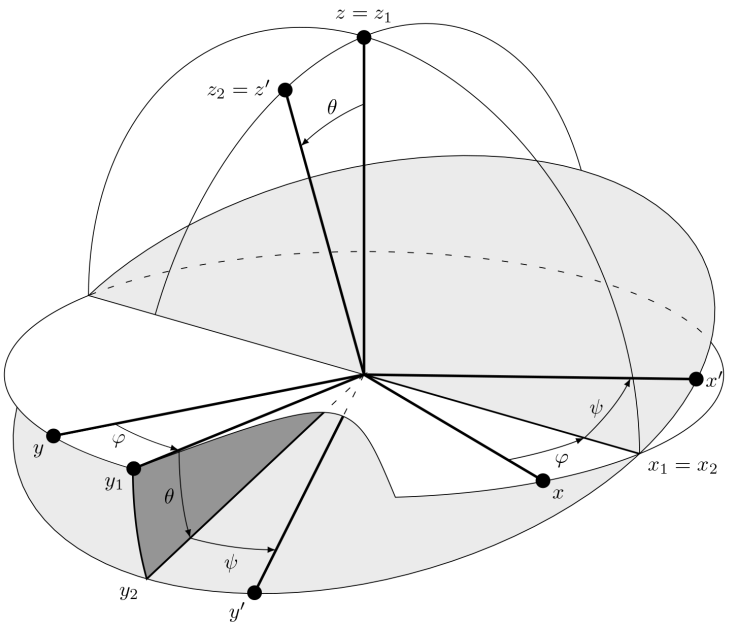

Figure 3.5: The Euler angles $\{\varphi,\, \theta,\, \psi\}$ convert between the detector frame $(x,\, y,\, z)$ and the gravitational-wave propagation frame $(x',\, y',\, z')$. For better visual depiction, the y coordinates have their signs inverted.

where the detector tensor, $\overleftrightarrow{d}$, is defined as:

$$\overleftrightarrow{d} = \frac{\hat{i} \otimes \hat{i} - \hat{j} \otimes \hat{j}}{2},$$

and F_+ and $F_\times$ are the antenna response patterns (Figure 3.6):

$$F_+ = \overleftrightarrow{e}_+ : \overleftrightarrow{d} = \frac{1}{2}(1 + \cos^2\theta)\cos 2\varphi \cos 2\psi + \cos\theta \sin 2\varphi \sin 2\psi$$

and

$$F_\times = \overleftrightarrow{e}_\times : \overleftrightarrow{d} = -\frac{1}{2}(1 + \cos^2\theta)\cos 2\varphi \sin 2\psi - \cos\theta \sin 2\varphi \cos 2\psi.$$

To see why this is true, we calculate the time it takes for a photon to travel (in the detector reference frame) from the beam splitter located spatially at $(0,\, 0,\, 0)$ to a freely-falling mirror at $(L_0,\, 0,\, 0)$ and back. This requires solving the equation:

$$ds^2 = -c^2 dt^2 + (1 + h_{11})(dx^1)^2 = 0,$$

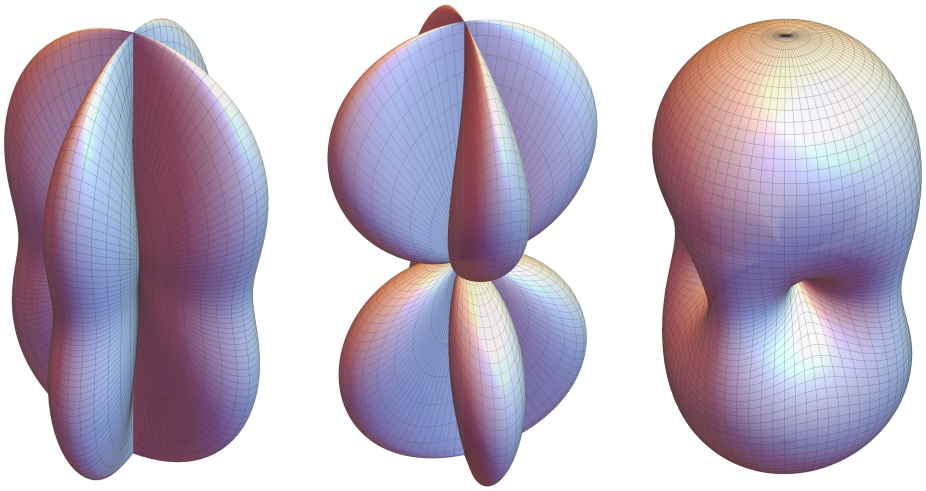

Figure 3.6: Antenna response patterns for an interferometric detector of the + (left), × (center), and RMS (right) polarizations, computed with polarization angle $\psi = 0$.

which in the limit that the light travel time of the photons is short compared to the gravitational-wave period (i.e., $L_0 \ll \lambda_{\mathrm{GW}}$), gives us:

$$\begin{aligned} dt &= \frac{\sqrt{1+h_{11}}}{c}\left|dx^1\right| \\ &\approx \left(1+\frac{1}{2}h_{11}\right)\frac{|dx^1|}{c} \end{aligned}$$

such that

$$\begin{aligned} T_{\mathrm{roundtrip}} &= \left(1+\frac{1}{2}h_{11}\right)\frac{2L_0}{c} \\ &= \frac{2L_1}{c}. \end{aligned}$$

In other words:

$$L_1 = L_0\left(1+\frac{1}{2}h_{11}\right),$$

or written more generally:

$$L_{\hat{u}} = L_0\left(1+\frac{1}{2}\hat{i}\cdot\overleftrightarrow{h}\cdot\hat{i}\right),$$

which allows us to calculate the difference in roundtrip times down the two arms. Then, the gravitational-wave strain, h, can be defined as:

$$\begin{aligned} h &= \frac{L_{\hat{i}} - L_{\hat{j}}}{L_0} \\ &= \frac{1}{2}\left(\hat{i}\cdot\overleftrightarrow{h}\cdot\hat{i} - \hat{j}\cdot\overleftrightarrow{h}\cdot\hat{j}\right) \\ &= \frac{1}{2}\left(i^a h_{ab} i^b - j^a h_{ab} j^b\right) = h_{ab}\left(\frac{i^a i^b - j^a j^b}{2}\right) \\ &= \overleftrightarrow{h} : \frac{\hat{i}\otimes\hat{i} - \hat{j}\otimes\hat{j}}{2} \\ &= \overleftrightarrow{h} : \overleftrightarrow{d}, \end{aligned}$$

as shown above.

The derivation of the antenna response patterns, F_+ and $F_\times$, requires use of the rotation matrix constructed from the Euler angles that transform between the two reference frames (Figure 3.5):

$$R^{a'}_{a} = \begin{pmatrix} A & B & C \\ D & E & F \\ G & H & I \end{pmatrix} =$$

$$\begin{pmatrix} \cos\psi\cos\varphi - \cos\theta\sin\varphi\sin\psi & \cos\psi\sin\varphi + \cos\theta\cos\varphi\sin\psi & \sin\psi\sin\theta \\ -\sin\psi\cos\varphi - \cos\theta\sin\phi\cos\psi & -\sin\psi\sin\varphi + \cos\theta\cos\varphi\cos\psi & \cos\psi\sin\theta \\ \sin\theta\sin\phi & -\sin\theta\cos\varphi & \cos\theta \end{pmatrix}.$$

Then, the antenna response patterns are:

$$
\begin{aligned}
F_+ &= \overleftrightarrow{e}_+ : \overleftrightarrow{d} = e_{+ab} d^{ab} \\
&= R^{a'}_a R^{b'}_b e_{+a'b'} d^{ab} \\
&= \mathrm{Tr}\left[\frac{1}{2} R^\intercal \begin{pmatrix} 1 & 0 & 0 \\ 0 & -1 & 0 \\ 0 & 0 & 0 \end{pmatrix} R \begin{pmatrix} 1 & 0 & 0 \\ 0 & -1 & 0 \\ 0 & 0 & 0 \end{pmatrix} \right] \\
&= \frac{A^2 - D^2 - B^2 + E^2}{2} \\
&= \frac{1}{2}(1 + \cos^2\theta)\cos 2\varphi \cos 2\psi + \cos\theta \sin 2\varphi \sin 2\psi
\end{aligned}
$$

and

$$
\begin{aligned}
F_\times &= \overleftrightarrow{e}_\times : \overleftrightarrow{d} = e_{\times ab} d^{ab} \\
&= R^{a'}_a R^{b'}_b e_{\times a'b'} d^{ab} \\
&= \mathrm{Tr}\left[\frac{1}{2} R^\intercal \begin{pmatrix} 0 & 1 & 0 \\ 1 & 0 & 0 \\ 0 & 0 & 0 \end{pmatrix} R \begin{pmatrix} 1 & 0 & 0 \\ 0 & -1 & 0 \\ 0 & 0 & 0 \end{pmatrix} \right] \\
&= AD - EB \\
&= -\frac{1}{2}(1 + \cos^2\theta)\cos 2\varphi \sin 2\psi - \cos\theta \sin 2\varphi \cos 2\psi.
\end{aligned}
$$

In Figure 3.7, the root mean square (RMS) combination of F_+ and $F_\times$ when $\psi = 0$ is shown enlarged with the L-shaped arms of the detector drawn in for reference. Thus, the detectors are most sensitive to gravitational waves coming from directly above and below, forming the two antipodal regions of the peanut-shaped antenna pattern. In Figure 3.8, this explains the two bright yellow regions in each sky localization probability map (skymap).

Next, the detectors are least sensitive to gravitational waves coming from directions within the plane of the detector arms, especially along the diagonals.

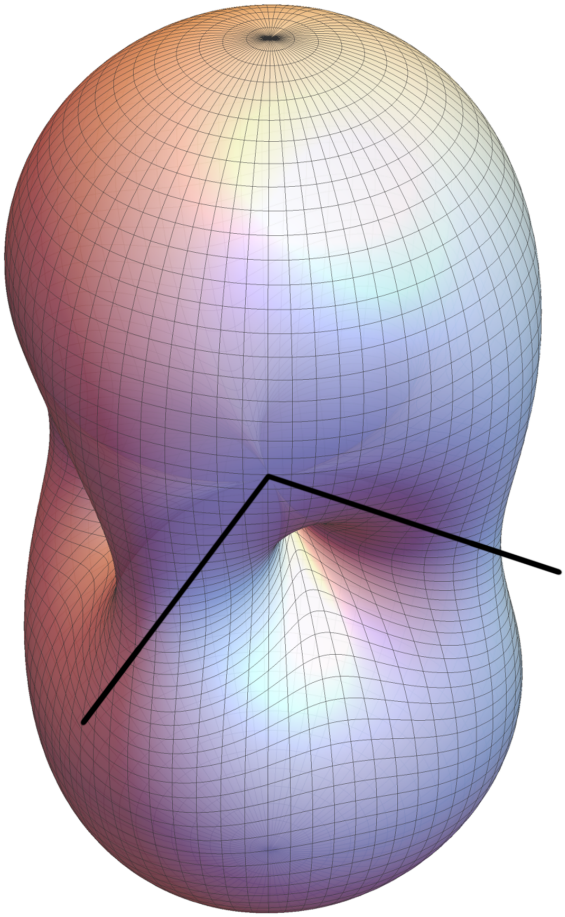

Figure 3.7: The RMS combination of the + and × polarization antenna response patterns when the polarization angle, $\psi = 0$. The detector arms are drawn in for reference.

This is because the arms would be stretched and squeezed equally by passing gravitational waves from these directions, creating zero strain. This explains the four indentations (i.e., nodes) in the RMS antenna pattern and the four black islands of ∼0 probability in each skymap of Figure 3.8.

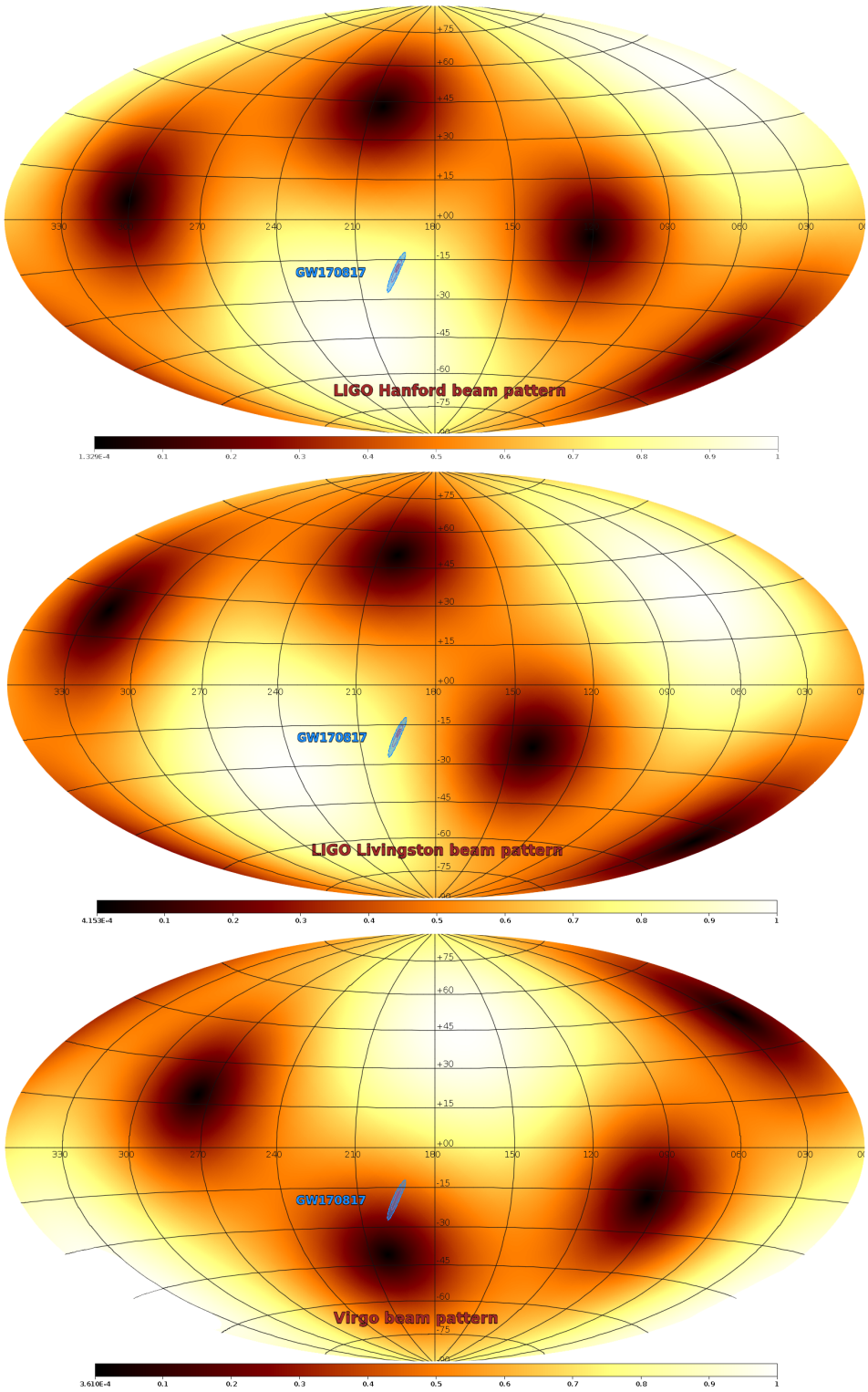

Figure 3.8: A three-detector (Advanced LIGO and Virgo) `BAYESTAR` sky localization of GW170817 in ICRS coordinates (Aitoff projection) overlaid on top of antenna patterns for each detector; see Chapter 6. (Figures from Giuseppe Greco, 2018)

Chapter 4

Low-Latency Searches for Gravitational-Wave Candidate Events

Of the many different kinds of gravitational-wave signals Advanced LIGO and Virgo can detect (bursts, periodic signals, coalescing binaries, and stochastic backgrounds), we focus on low-latency searches for gravitational-wave transients (i.e., bursts and coalescing binaries). We will introduce the two types of searches in place (modeled and unmodeled) which produce gravitational-wave triggers that enter the online Gravitational Wave Candidate Event Database (GraceDb). Then, we will walk through the automated and human data-quality vetting procedures to select the gravitational-wave trigger (now elevated to gravitational-wave candidate event status) to report for electromagnetic/neutrino follow-up.

Portions of this chapter will resemble the section on online gravitational-wave analysis I wrote for the LIGO Scientific Collaboration and Virgo Collaboration paper, *Low-Latency Gravitational Wave Alerts for Multi-Messenger Astronomy During the Second Advanced LIGO and Virgo Observing Run* (Abbott et al., 2019).

4.1 Compact Binary Coalescence Searches

Compact binary systems involving neutron stars and stellar mass black holes, (i.e., binary neutron star, neutron star-black hole, and binary black hole systems) merge in the sensitive frequency band of advanced ground-based in-

terferometric GW detectors. The modeled compact binary coalescence (CBC) searches specifically look for signals from these systems.

The waveform, $h(t)$, is the collected history of the stretching and squeezing of space by the coalescing binary. It requires solving the two-body problem with different tools of attack depending on the masses and compactness that are involved (Figure 4.1). Because the General Theory of Relativity dictates that the binary loses energy and angular momentum via gravitational radiation, the waveform features three general phases: an inspiral phase while the binary shrinks, a merger phase while the remnant object is formed, and a ringdown phase if the remnant object is a perturbed black hole. More specifically, during the inspiral, the binary 'chirps' (i.e., the gravitational-wave frequency and amplitude both increase) and during the merger, the peak frequency and amplitude are reached. Lastly, during the ringdown, the perturbed remnant black hole quickly settles into its final state by emitting gravitational waves with characteristic quasinormal modes.

The waveforms vary depending on the binary's intrinsic parameters such as the masses and spins that are involved, and also on extrinsic parameters such as orientation and distance with respect to the detectors (Table 4.1). A specific combination of the two individual masses (m_1 and m_2, $m_1 \geq m_2$) known as the chirp mass, $\mathcal{M}_c$, largely determines the binary's observed frequency (f) and frequency evolution ($\dot{f}$) at lower frequencies before the merger:

$$\mathcal{M}_c = \frac{(m_1 m_2)^{3/5}}{(m_1 + m_2)^{1/5}} = \frac{c^3}{G}\left(\frac{5}{96}\pi^{-8/3} f^{-11/3}\dot{f}\right)^{3/5},$$

where c is the vacuum speed of light and G is Newton's gravitational constant. Unfortunately, the chirp mass alone does not reveal the two individual masses or their spins. Instead, we need more information such as the mass ratio, m_1/m_2, which can be found by knowing the binary's waveform to higher

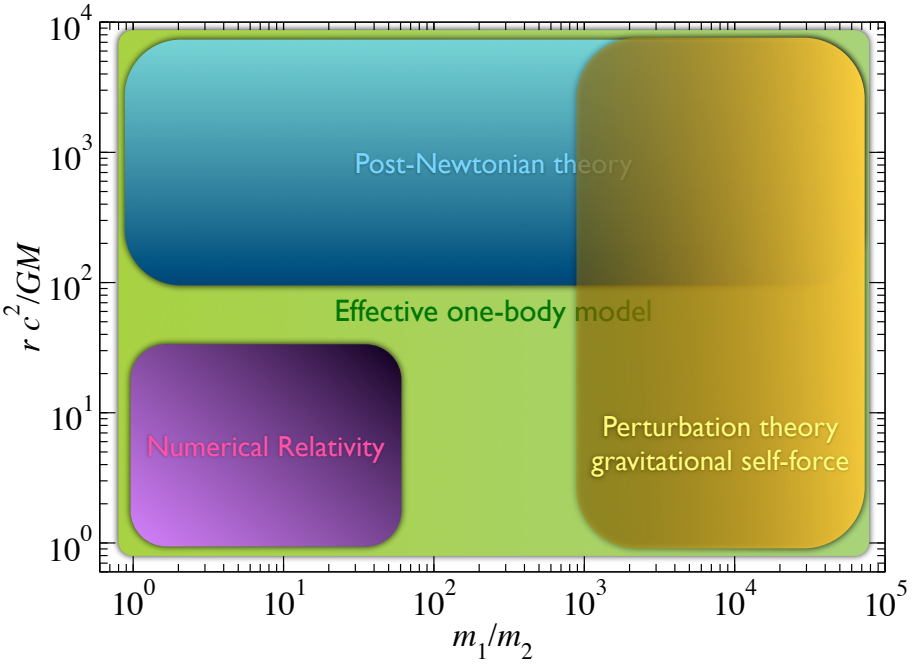

Figure 4.1: Main analytical and numerical methods for solving the two-body problem depends on the masses and compactness involved. Here, m_1 and m_2 ($m_1 \geq m_2$) are the two individual masses and rc^2/GM is a measure of the separation distance. (Figure from Buonanno & Sathyaprakash, 2014)

precision. Thus, the modeled CBC searches require knowing the waveforms from the last few orbits to very high precision.

Intrinsic Parameters $\vartheta_{\rm in}$		**Extrinsic Parameters** $\vartheta_{\rm ex}$	
m_1	mass of primary object	α	right ascension
m_2	mass of secondary object	δ	declination
$\vec{S}_1$	spin of primary object	r	distance
$\vec{S}_2$	spin of secondary object	$t_\oplus$	arrival time at detector
		ι	inclination angle
		ψ	polarization angle
		$\phi_{\rm c}$	coalescence phase

Table 4.1: Intrinsic and extrinsic parameters, ϑ, of a compact binary coalescence gravitational-wave waveform.

We can then solve for thousands upon thousands of these waveforms to construct a waveform template bank that suitably covers the parameter

space of compact binary systems. To determine the best-fit waveform (i.e., the matched template) that describes the gravitational-wave signal buried in the noisy detector output, we use a process known as matched filtering.

First, imagine a filter function $k(t)$ applied to our noisy detector output $s(t) = h(t) + n(t)$:

$$\hat{s} = \int_{-\infty}^{\infty} s(t)k(t)dt.$$

The signal (S) is the expected value of $\hat{s}$ when the gravitational-wave signal, $h(t)$, is present. The noise (N) is the RMS value of $\hat{s}$ when $h(t)$ is absent. Then, the matched template is determined by the filter function that optimizes the signal-to-noise ratio (SNR, S/N).

The exact solution is as follows. If we already know the waveform $h(t)$ of the gravitational-wave signal, we can construct the Wiener filter (i.e., the matched filter/template):

$$\tilde{k}(f) = \frac{\tilde{h}(f)}{S_n(f)},$$

to optimize the signal-to-noise ratio (i.e., the template's auto-correlation):

$$\left(\frac{S}{N}\right)^2 = 4\int_0^{\infty} \frac{\tilde{h}^*(f)\tilde{h}(f)}{S_n(f)}df.$$

However, in practice, we don't know $h(t)$, and instead have in place discrete waveform template banks with templates $h_i(t)$ that cover the target parameter space of compact binary systems (Table 4.3). Then, the SNR time series is determined by using the Wiener filter to compute the inner product of the whitened templates and the whitened detector output (i.e., the cross-correlation sequence between the data output and template):

$$\left(\frac{S}{N}\right)_i^2 = 4\int_0^{\infty} \frac{\tilde{h}_i^*(f)}{S_n^{1/2}(f)} \frac{\tilde{s}(f)}{S_n^{1/2}(f)} e^{i2\pi ft}df.$$

When the SNR peaks above a predetermined threshold set by the low-latency search pipeline, a single-detector gravitational-wave trigger with time of arrival

and coalescence phase information is produced for that detector's output data stream.

Sufficiently high SNR thresholds prevent Gaussian noise from being identified as a trigger because its Gaussian probability distribution drops off very quickly away from the mean. However, non-Gaussian noise is handled differently, by performing χ^2 waveform consistency tests and computing sine-Gaussian noise correlation statistics (using signal-based vetoes, (Nitz, 2018)), explicitly zeroing out loud and short instrumental noise transients (gating the data), and vetoing triggers occurring during times flagged as contaminated by known noise sources (applying the low-latency data quality vector).

Once pipeline-specific vetoes have been applied to the single-detector trigger lists (Table 4.2), the lists are then combined to search for coincident triggers across the detector network. Consistencies in the SNR, coalescence phase, trigger time, and template parameters determine the ranking statistic for the coincident trigger which can then be converted into a false alarm rate.

Triggers of high significance (low false alarm rates) are then elevated to gravitational-wave candidate event status if they pass scrutiny under automated and human data-quality checks. By this point, the `BAYESTAR` algorithm has already generated and uploaded a sky localization probability map for the candidate. Two things happen in parallel next. One, we do a more thorough job determining the source parameters, relaxing assumptions made by the low-latency pipelines: all low-latency CBC pipelines assume that the compact objects are aligned or anti-aligned with the orbital angular momentum and that the orbital eccentricity is negligible. Two, we report the candidate event to our observing partners for electromagnetic/neutrino follow-up.

Currently, with a few months before the advent of the third observing

run, O3, we have 4 low-latency modeled CBC searches in place: `GstLAL`, `MBTAOnline`, `PyCBC Live` (which all produced triggers during the first and second observing runs), and a new low-latency search pipeline called `SPIIR`. Pipeline-specific matched filtering technique and background estimation are outlined next.

	`PyCBC Live`	`GstLAL`	`MBTAOnline`	`SPIIR`*
Signal-based vetoes	✓	✓	✓	✓
Low-latency data quality vector	✓		✓	✓
Gated data		✓		✓

Table 4.2: Pipeline-specific measures (marked with a ✓) to identify non-Gaussian noise sources in single-detector trigger lists during the second observing run, O2.

* Alerts for triggers from `SPIIR` were not sent to observing partners during O2. However, this is subject to change for the third observing run, O3.

GstLAL

The GStreamer LIGO Algorithm Library (`GstLAL`) low-latency search pipeline performs matched filtering in the time domain with real template waveforms (Messick et al., 2017). Trigger significance is calculated by constructing a likelihood-ratio ranking statistic that models the distribution of trigger properties for noise and GW events (Cannon et al., 2015). The background is computed by synthesizing likelihood ratios from a random sampling of a probability density that is estimated using non-coincident triggers accumulated over the course of an observing run, which are taken to be noise.

MBTAOnline

The Multi-Band Template Analysis (`MBTAOnline`) low-latency search pipeline performs matched filtering in the frequency-domain with complex template

waveforms. It uses several matched filters to cover the detector bandwidth, i.e., the matched filter is split across multiple frequency bands (Adams et al., 2016). This allows for shorter templates to be used in each frequency band and GW candidate events to be identified with sub-minute latencies. The SNR is defined to be the modulus of the complex matched filter response and is evaluated at its maximum value to extract the signal time of arrival and coalescence phase.

The background distribution of the ranking statistic is constructed by making every possible coincidence from single-detector triggers over few hours of recent data. It then folds in the probability of a pair of triggers passing the temporal coincidence test.

PyCBC Live

The Python CBC (`PyCBC Live`) low-latency search pipeline performs matched filtering in the frequency-domain with complex template waveforms (Nitz et al., 2018). It estimates the background of accidental coincidences by using time slides between triggers from different detectors generated within the 5 most recent hours of live time data. This choice limits the online inverse false alarm rate to $\sim$100 yr.

SPIIR

The Summed Parallel Infinite Impulse Response (`SPIIR`) low-latency search pipeline performs matched filtering in the frequency-domain using a set of infinite impulse response (IIR) filters to approximate the template waveforms (Chu, 2017). It produces gravitational-wave candidate events with sub-minute latencies where the significance is evaluated by the distribution of background events. To estimate this background, `SPIIR` uses time slides of live time data from the past week.

	PyCBC Live	GstLAL	MBTAOnline
Total mass $m_1 + m_2$	$2{-}500^{a} M_\odot$	$2{-}150^{a} M_\odot$	$2{-}100 M_\odot$
Mass ratio m_1/m_2	1−98	1−98	1−99
Minimum component mass m_2	$1 M_\odot$	$1 M_\odot$	$1 M_\odot$
Spin magnitude[b] ($m < 2M_\odot$)	0−0.05	0−0.05	0−0.05
Spin magnitude[b] ($m > 2M_\odot$)	0−0.998	0−0.999	0−0.9899
SNR threshold for triggering	5.5	4 (L), 3 (V)[c]	5.5[d]

Table 4.3: Template bank parameters and SNR threshold for triggering used by the low-latency CBC search pipelines during the second observing run, O2. (Table from Abbott et al., 2019)

[a] The maximum total mass for `PyCBC Live` and `GstLAL` is in fact a function of mass ratio and component spins (Dal Canton & Harry, 2017; Mukherjee et al., 2017). In this table, we indicate the highest total mass limit over all mass ratios and spins.

[b] For detection, the component spins, $\vec{S}_1$ and $\vec{S}_2$, are often assumed to be non-precessing and aligned with the binary's total angular momentum.

[c] `GstLAL` requires an SNR threshold of 4 for triggers from Advanced LIGO versus 3 for triggers from Virgo.

[d] `MBTAOnline` uses a higher SNR threshold of 6 for triggers from Advanced LIGO to form coincidences with triggers from Virgo.

4.2 Burst Searches

There are also two unmodeled "Burst" searches, `cWB` and `oLIB`, that are capable of detecting gravitational waves from a wide variety of astrophysical sources in addition to compact binary coalescences. This includes (but is not limited to) core-collapse supernovae, magnetar starquakes, and more speculative sources such as intersecting cosmic strings.

The Burst searches work by looking for excess power in the time-frequency (TF) domain of the GW strain data (Klimenko et al., 2016; Lynch et al., 2017). To understand the time-frequency domain, first let's take the Fourier transform of a function $s(t)$ defined on the real axis $-\infty < t < \infty$. The power spectrum of the transform, $|\tilde{s}(f)|^2$, reveals the dominant Fourier components but tells us nothing about the phase relations between the components (i.e., we do not know when things happened). Thus, the simplest way to recover temporal

information is to transform segments of length δt on the real axis.

The power spectrum of the Fourier transform of $s(t)$ on the interval $0 < t < \delta t$ reveals the dominant Fourier components for that interval with resolution $1/\delta t$. We can repeat this process for $\delta t < t < 2\delta t$, and so on. Thus, working in the TF plane we can determine a reasonable estimate of the total duration of the signal along with its dominant frequency range.

The excess power method works as follows. Advanced LIGO and Virgo's strain data are available using a sampling rate of either 16384 Hz or 4096 Hz. Thus, a detector output data segment of duration $\delta t = N\Delta t$ (Δt equal to 1/16384 s or 1/4096 s) consists of a discrete set of $N + 1$ values:

$$s_j = s[t_{\rm start} + j\Delta t],$$

where $t_{\rm start}$ is the start time of the segment and $j = 0, 1, \ldots, N$.

In Fourier space, these values become:

$$\tilde{s}_k = \sum_{j=0}^{N-1} s_j e^{-i2\pi jk/N},$$

which can be re-written as:

$$\tilde{s}_k = \sum_{j=0}^{N-1} s[t_j] e^{-i2\pi(t_j - t_{\rm start})f_k},$$

with $t_j = t_{\rm start} + j\Delta t$ and $f_k = k/\delta t$. Thus, the frequency resolution is $1/\delta t$ and the maximum frequency is $N/\delta t$ since $\tilde{s}_k = \tilde{s}_{k+N}$.

However, the detector output is the sum of the noise and a potential signal, $\tilde{s}_k = \tilde{n}_k + \tilde{h}_k$. Thus,

$$\tilde{n}_k = \sum_{j=0}^{N-1} n[t_j] e^{-i2\pi(t_j - t_{\rm start})f_k} \text{ and}$$
$$\tilde{h}_k = \sum_{j=0}^{N-1} h[t_j] e^{-i2\pi(t_j - t_{\rm start})f_k}.$$

If we assume the different Fourier components of noise are uncorrelated (i.e., the noise is stationary and the detector is stable), we also have:

$$\langle \tilde{n}_k^* \tilde{n}'_k \rangle = \delta_{kk'} \frac{1}{2} S_n[f_k],$$

where $S_n(f_k)$ is the single-sided noise power spectral density and $\delta_{kk'}$ is the Kronecker delta function.

Then, minimal assumptions about the gravitational-wave signal allow us to calculate its excess power statistic. For simplicity, let's say that the signal is of duration δt with its power concentrated in the frequency band $f_1 < f < f_2$, where $f_1 = k_1/\delta t$ and $f_2 = k_2/\delta t$. The excess power statistic is defined as:

$$\mathcal{E} = 4 \sum_{k=k_1}^{k_2} \frac{|\tilde{s}_k|^2}{S_n[f_k]},$$

thus we compute values of $\mathcal{E}$ over all possible start times. Segments with excess power above a predetermined threshold indicate potential triggers.

cWB

The coherent WaveBurst (`cWB`) low-latency search algorithm uses Wilson-Daubechies-Meyer (WDM) transform to convert detector output from a network of M GW detectors into the TF plane at different frequency resolutions. These transforms are generalizations of the Fourier transform:

$$S_{m;k,l} = \sum_{j=0}^{N-1} f_{k,l}[t_j] s_m[t_j],$$

where $f_{k,l}$ are WDM filter functions and s_m is output from the m^{th} detector (Necula et al., 2012; Klimenko et al., 2016). Then, `cWB` identifies clusters of TF pixels with excess power above the baseline detector noise. Clusters that overlap in time and frequency at different frequency resolutions indicate the presence of a GW trigger.

Using a maximum likelihood approach, principal components of the WDM transform from different resolutions are maximized over all possible time-of-flight delays in the network of GW detectors for the purpose of selecting pixels from the cluster that describe the GW signal completely and without overlapping information. The contribution from the trigger energy which is coherent among the involved detectors is used to calculate the detection statistic, which is compared to the background to estimate the trigger's significance. Triggers of high significance are followed-up with waveform reconstruction and the creation of sky localization probability maps (skymaps) since they could be elevated to candidate event status.

oLIB

For the Omicron LALInferenceBurst (`oLIB`) low-latency search algorithm, we define a central time ($t_{\rm c}$), central frequency ($f_{\rm c}$), duration ($\sigma_{\rm t}$), and bandwidth ($\sigma_{\rm f}$) for gravitational-wave transients that are well localized in both time and frequency:

$$
\begin{aligned}
t_{\rm c} &= \int_{-\infty}^{\infty} t \frac{|h(t)|^2}{||h||^2} dt, \\
f_{\rm c} &= 2\int_{0}^{\infty} f \frac{|\tilde{h}(f)|^2}{||h||^2} df, \\
\sigma_{\rm t}^2 &= \int_{-\infty}^{\infty} (t-t_{\rm c})^2 \frac{|h(t)|^2}{||h||^2} dt, \\
\sigma_{\rm f}^2 &= 2\int_{0}^{\infty} (f-f_{\rm c})^2 \frac{|\tilde{h}(f)|^2}{||h||^2} df,
\end{aligned}
$$

where

$$
||h||^2 = \int_{-\infty}^{\infty} |h(t)|^2 dt = \int_{-\infty}^{\infty} |\tilde{h}(f)|^2 df.
$$

The dimensionless quality factor $Q = f_{\rm c}/\sigma_{\rm f}$ is a measure of this transient's aspect ratio in the TF plane.

Then, `oLIB` uses Q transform to decompose single detector data output into several TF planes of constant quality factors $Q \sim \tau f_0$, where τ and f_0 are the time resolution and central frequency of the transform's filter/wavelet (Chatterji et al., 2004; Lynch et al., 2017):

$$s_{f_0}[t_m] = \sum_{j=0}^{N-1} s[t_j] w_{f_0}[t_j - t_m] e^{-i2\pi j f_0/N}.$$

Above, $w_{f_0}[t_j - t_m]$ is the time-domain window function centered around t_m with a duration that is inversely proportional to the frequency under consideration.

Then, the `Omicron` software in `oLIB` clusters data segments of excess power with identical f_0 and Q spaced within 100 ms of each other. Searches for coincidences are performed in two stages: first with $\pm$ 50 ms and second with $\pm$ $\sim$10 ms. Finally, `Omicron` clusters the coincident triggers such that only one trigger for each analysis window of 100 ms is analyzed.

The `LALInferenceBurst` software in `oLIB` then coherently analyzes the coincident triggers to produce two Bayes factors: $\mathcal{B}_{\rm SN}$ and $\mathcal{B}_{\rm CI}$. $\mathcal{B}_{\rm SN}$ compares a signal model (S) to a Gaussian noise model (N) to roughly measure the loudness of the signals and $\mathcal{B}_{\rm CI}$ compares a 'coherent', i.e., correlated signal model (C) to an 'incoherent', i.e., uncorrelated signal model (I) to roughly measure how similar the signals look in each detector. A likelihood ratio test uses both of these statistics to compute the significance of the gravitational-wave trigger which is then submitted into GraceDb if above a set threshold.

4.3 GraceDb

All triggers produced by the low-latency search pipelines enter an interactive database known as GraceDb[1] (the Gravitational Wave Candidate Event

[1] https://gracedb.ligo.org/

Database), the centralized hub for aggregating and disseminating information about GW candidate events. It features a human-friendly web interface for displaying information as well as a RESTful API (representational state transfer application program interface) for programmatic interaction with the service. Tools provided by GraceDb's Python-based client package allow users to add new events to the database, annotate existing events, perform searches, upload files, and more. GraceDb also alerts follow-up advocates (humans on duty who analyze and decide whether or not a GW trigger is appropriate for electromagnetic/neutrino follow-up) via text messaging and phone calls using Twilio.

Automated follow-up processes of GW candidate events that perform tasks such as parameter estimation or detector characterization are alerted of new event creation and updates to events in GraceDb via push notifications using the LIGO-Virgo Alert System (`LVAlert`). Users and listeners of the LVAlert notification service based on the extensible messaging and presence protocol (XMPP) create and subscribe to specific messaging nodes to receive target notifications (e.g., from a specific low-latency search pipeline or heartbeat process for debugging).

4.4 Supervised Electromagnetic/Neutrino Follow-Up Process

For O1 and O2, several follow-up processes responded to the entry of a GW trigger into GraceDb, notified by the receipt of an LVAlert message. Three of these processes were of immediate relevance to the electromagnetic/neutrino follow-up effort: the low-latency skymap generator for CBC candidate events (`BAYESTAR`, the BAYESian TriAngulation and Rapid localization pipeline for O1 and O2), the tracker of candidate event status/updates and alert generator/sender (`approval_processor` for O1, upgraded to `approval_processorMP`

for O2), and the tracker of other follow-up processes starting and ending on time (`eventSupervisor` for O2 only).

In particular for O1 and O2, I wrote the majority of the software responsible for making the decision to send alerts based on incoming state information about the GW triggers, `approval_processor`/`approval_processorMP` (Chapter 5).

4.5 Online Automated Data Vetting

Low-latency gravitational-wave search pipelines receive detector state information indicating when the detectors' data are suitable for use in astrophysical analysis. This includes times when the detectors are operating in a nominal state and data calibration is accurate. However, additional information is required to deal with non-Gaussian transient noise artifacts known as glitches, which can mimic true gravitational-wave signals and often plague the detectors' data.

In Table 4.2, we see that some known forms of instrumental noise are passed to the low-latency search pipelines through the 'low-latency data quality vector'. This vector produces data quality vetoes which flag times of known data quality issues with 1/16 s resolution. They are generated in real time using sensors that measure the behavior of the instruments and their environment. If a GW trigger occurs during a time that is vetoed, it is not reported for electromagnetic/neutrino follow-up. Because of this feature, data quality vetoes are reserved for severe noise sources.

There are also low-latency glitch detection algorithms which search detector data for correlations between witness sensors and GW strain data. In the case of the streaming machine learning pipeline, `iDQ`, which houses several of these algorithms, i.e., 'classifiers', a glitch false alarm probability (FAP) is

reported around the time of a GW trigger which measures the probability that the detector was in a nominal state based on the presence of glitches in witness sensors (Essick et al., 2013; Biswas et al., 2013).

For O1 and O2, `approval_processor` and `approval_processorMP` collected `iDQ` glitch FAP information produced by the `ovl` classifer to define an `iDQ`-based veto:

$$\text{joint glitch FAP} = \prod_{i=1}^{N} \text{glitch FAP}_i \Rightarrow \begin{cases} \text{veto if joint glitch FAP} \leq 0.01 \\ \text{pass if joint glitch FAP} > 0.01, \end{cases}$$

where $i = 1, \ldots, N$ are all relevant detectors in a GW trigger detection. This veto was applied to triggers from Burst low-latency search pipelines only. During O1, I found that CBC triggers did not benefit from using glitch FAP information generated using time windows comparable to waveform template durations because of the large deadtimes that were introduced.

4.6 Human Vetting

During O1 and O2, GW triggers required human approval to be elevated to candidate event status, i.e., to officially be released to our observing partners via the LIGO/Virgo Initial Notice (a machine-readable alert containing the GW candidate event's basic properties plus a sky localization probability map (skymap)). For O3, we will enter the era of public alerts, where LIGO/Virgo Preliminary Notices will be released to the public without human vetting. (By definition, Preliminary Notices contain preliminary information with zero human vetting. In O1 and O2, we kept these alerts internal to the LIGO Scientific Collaboration and Virgo Collaboration.) However, in O3, LIGO/Virgo Initial Notices will still require human vetting and the process will be as follows.

For humans to become involved in the mix, GW triggers must pass all the previous major hurdles: have a low enough false alarm rate, not occur

during a data quality vetoed time, not be a hardware injection, and have a high enough `iDQ` joint glitch false alarm probability (for Burst triggers only). At this point for O1 and O2, `approval_processor`/`approval_processorMP` requested sign-offs from the appropriate mix of LIGO/Hanford, LIGO/Livingston, and Virgo (near the end of O2[2]) detector operators by triggering an alarm in the observatory control rooms. Essentially, detector operators were to qualitatively answer the question, "At the time of the trigger, were things running normally?", as OK or NOT OK. This way, we could ensure unusual events such as thunderstorms, trucks driving close the buildings, etc. did not occur at the time of the GW trigger and that the interferometers were running optimally.

The OK response from operators generated two actions. One, the Rapid Response Teams (RRTs) consisting of commissioning, computing, and calibration experts at each detector site documented the state of the detectors and two, `approval_processor`/`approval_processorMP` applied the special GraceDb label, ADVREQ (advocate required), to generate texts, emails, and phone calls from GraceDb to the electromagnetic/neutrino (EM) follow-up advocates.

Thus, many different groups of persons from the collaborations were involved in the decision-making process: detector operators, RRTs, low-latency search pipeline experts, detector characterization (data quality) experts, and EM follow-up advocates. We all met at our designated TeamSpeak channel for the on-call validation process within minutes of being notified of the GW trigger.

First, the EM follow-up advocates on duty perform non-stationary noise

[2]Advanced Virgo joined the Advanced LIGO GW detector network in August 2017 for the last month of O2 data acquisition.

checks and daily/weekly event rate checks. For the non-stationary noise check, if there are 2 or more CBC GW triggers more than 1 second apart from the same low-latency search pipeline in a given time frame, the pipeline is likely responding to non-stationary noise which affected the false alarm rate estimates and we reject all triggers. Likewise, if there are two or more Burst triggers more than 5 seconds apart from the same Burst pipeline, we reject all triggers. However, it is of course okay to have different search pipelines produce triggers close in time; this is what we want! For the event rate check, if too many viable candidate events appear to be occurring too close together, this suggests a problem with the background estimation. In this case, the advocate on duty would double check with the search pipeline expert to see if anything could be wrong with the analysis.

Next, all previously mentioned data vetting products (Section 4.5) and additional data quality information (e.g., `Omega` and `Omicron` scans) not accessible at low-latency timescales are considered. The `Omega` and `Omicron` scans are spectrograms, i.e., power scans, that help us visualize witness sensor data in the TF domain around the time of the GW trigger (Chatterji et al., 2004; Robinet, 2016) when we ask two essential questions regarding data quality:

1. Could transient noise account for the trigger that we see? If yes, veto. If no, proceed to next question.

2. Could transient noise bias the estimate of the source parameter and properties? If yes, mitigate. If no, proceed with the vetting process.

This is because the same type of noise might in one case be vetoed, and in another case, be mitigated. For example, in Figure 4.2, spectrograms featuring similar type overflows but requiring different types of response actions are presented.

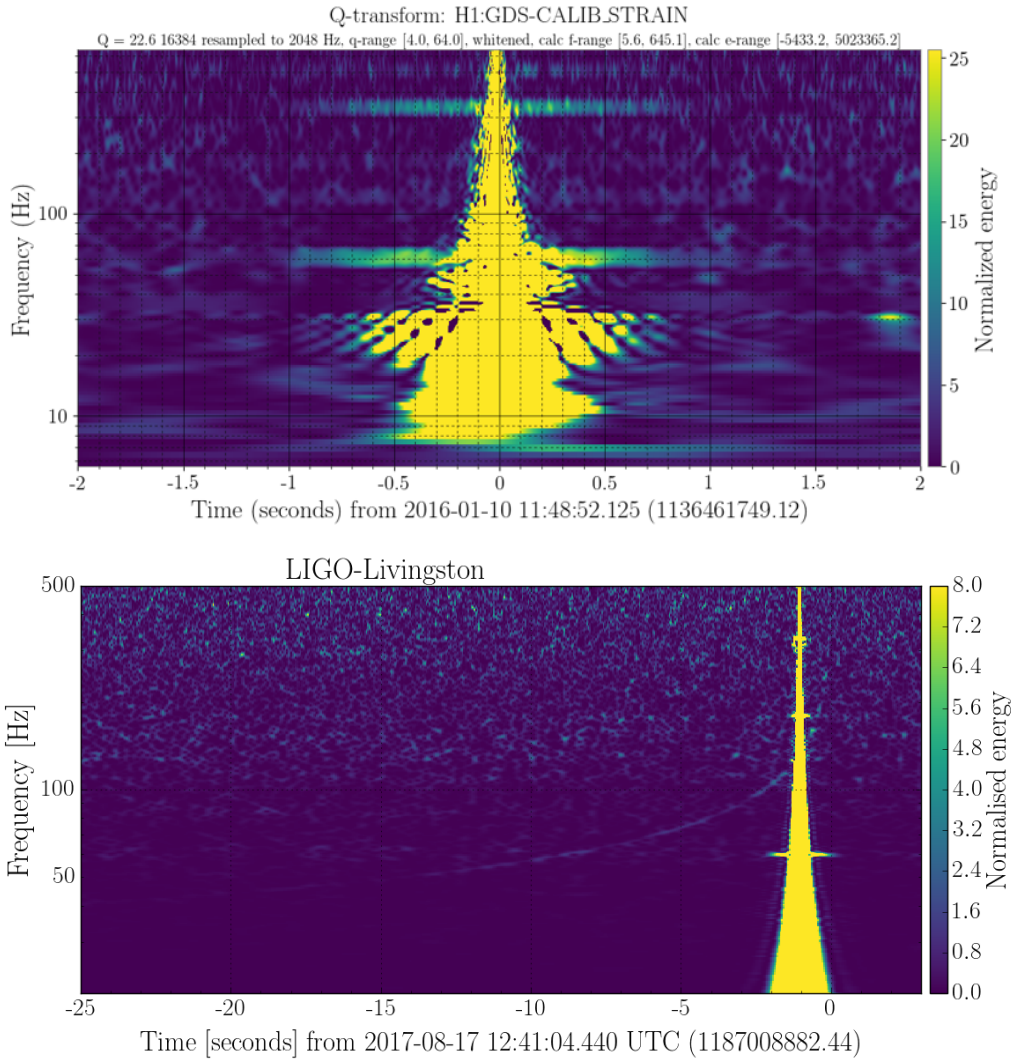

Figure 4.2: Spectrograms of an overflow glitch that requires a veto for the corresponding GW trigger (top) and mitigation (bottom). The bottom figure is from the Advanced LIGO/Livingston C00 "online calibrated" data for GW170817 (https://dcc.ligo.org/P1700337/public). The faint but characteristic trace of the BNS chirp can be seen in the background; thus, the noise was modeled and subtracted. (Figure from Abbott et al., 2017a)

The low-latency search pipeline experts also have to defend or clarify the significance of their triggers. In the past, when we had more than one viable GW trigger ((declared as neighbors if their event times were contained within ± 5 seconds of each other), the EM follow-up advocates selected the most promising candidate based on pre-established criteria (e.g., lowest FAR, choosing CBC over Burst triggers for compact binary events). For O3, the grouping of neighbor triggers is handled automatically through the creation of 'Superevents' in GraceDb.

Finally, the EM follow-up advocates select the skymap to include in the Initial Notice depending on the validation done at different instrument sites. For O2, a priority was given to the two Advanced LIGO detectors since they were more sensitive. At this point, we are ready to send the Initial Notice for the GW trigger (for O1 and O2 to our MOU observing partners) or Superevent (for O3 to the public), and compose to corresponding Initial Circular.

When necessary, search pipeline experts and the data quality team with the help of the RRTs recommended LIGO/Virgo Retraction Notices after days or weeks, using extended data investigation and/or updated FAR calculation based on additional background data. For example, during O2, GW candidate event G275404 originally detected by `PyCBC Live` and `GstLAL` did not appear in the offline analysis by either search pipeline and its 50%/90% credible regions in the skymaps increased from 460/2100 deg^2 for `BAYESTAR` to 2000/17000 deg^2 for `LALInference`. Thus, a LIGO/Virgo Retraction Circular was sent stating: "Neither search produced a significant trigger at the time of G275404. We conclude that G275404 is not a trigger of interest and does not warrant further follow-up." (LIGO Scientific Collaboration & Virgo Collaboration, 2017).

Chapter 5

O1: The First Observing Run

The first observing run (O1) from September 12, 2015 to January 19, 2016 involved only the two Advanced LIGO detectors in the United States. During the course of O1, there were 2 confident gravitational-wave events and 1 LIGO-Virgo trigger (LVT), later named GW150914 ("The First Monday Event"), GW151226 ("The Boxing Day Event"), and LVT151012 ("The Second Monday Event").

The confident GW detections were both stellar mass binary black hole mergers, and they revealed that there exists a class of heavier stellar mass black holes than those deduced previously from electromagnetic (X-ray binary) observations. LVT151012, was also recently declared a true gravitational-wave event (GW151012) as stated in the post-O2 CBC "catalog" paper, *GWTC-1: A Gravitational-Wave Transient Catalog of Compact Binary Mergers Observed by LIGO and Virgo during the First and Second Observing Runs* (Abbott et al., 2018).

In this chapter, I detail work I began before O1 started. Namely, I wrote a Python-based information-checking and decision-making software program named `approval_processor` to prepare for the event we might have a serendipitous gravitational-wave candidate requiring electromagnetic/neutrino follow-up.

5.1 approval_processor: The First of the Advanced Detector Era Gravitational-Wave Candidate Event Annotators

The first low-latency search for EM counterparts was conducted by the Locating and Observing Optical Counterparts to Unmodeled GW Pulses (LOOC UP) Project between December 2009 and October 2010, during the Initial LIGO era (2005 to 2010). LOOC UP provided sky localization estimates for potential GW events with latencies on the order of thirty minutes to radio, optical, and X-ray telescopes (Kanner et al., 2008; Kanner, 2011).

For the Advanced Detector era, the EM follow-up program was largely orchestrated by the `approval_processor` software program. The primary role of `approval_processor` was to internally alert humans within the LIGO Scientific Collaboration and Virgo Collaboration of significant GW triggers entering GraceDb that required more thorough (i.e., human) vetting, before taking on its secondary role of sending alerts for vetted candidates to our observing partners via the Gamma-ray Coordinates Network[1] (GCN). Basic trigger properties from the pipelines (false alarm rate, trigger time-of-arrival on Earth, detectors involved with the trigger), data quality and data products, detector operator and advocate signoffs determining the result of human vetting, and other labels identifying temporally correlated external triggers or signal injections performed in hardware at the sites[2] were considered.

Although updates to `approval_processor` were made during the course of the first observing run, it successfully sent LIGO/Virgo Notices to our observing partners to generate EM/neutrino follow-up for the first binary black hole merger detections and candidate events in history (see Figure 5.1 to view the alerts/follow-up timeline for GW150914, the first ever observed binary

[1] https://gcn.gsfc.nasa.gov

[2] Hardware signal injections are simulated GW signals created by physically displacing the detectors' test masses (Biwer et al., 2017)

black hole merger).

Below are the information included by `approval_processor` in its alerts.

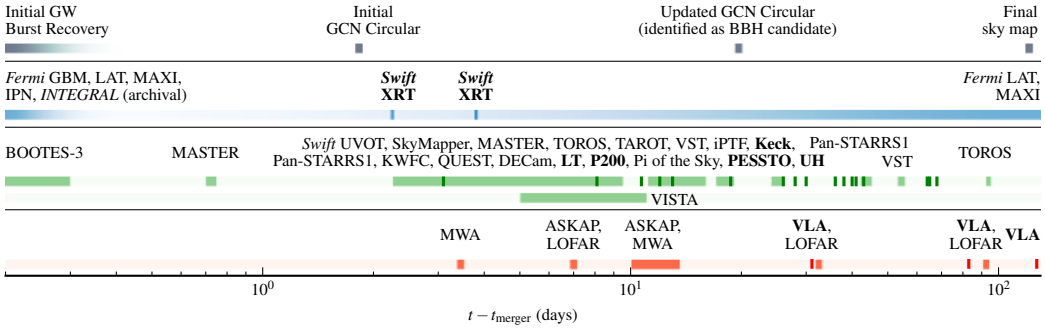

Figure 5.1: Timeline of LIGO/Virgo Notices and Circulars sent to our MOU partners for GW150914 and its electromagnetic follow-up. (Figure from Abbott et al., 2016a)

5.2 Information Sent to MOU Partners

False Alarm Rate

The measure of significance for a gravitational-wave trigger is the estimated false alarm rate (FAR), which quantifies the rate at which noise events with as high a ranking as the foreground trigger are generated. For each of the observing runs, there was a predetermined FAR threshold for sending alerts to our observing partners. For the majority of the first and second observing runs, this FAR threshold was one CBC and one Burst candidate event per month of live-time for O1 (3.8×10^{-7} Hz) and one CBC and one Burst candidate event per two months of live-time for O2 (1.9×10^{-7} Hz).

The FAR estimation method is specific to the low-latency search pipeline that triggers the candidate event (Section 4), although the most common method uses time slides (Figure 5.2). With the method of time slides, data sets from the various GW detectors are time-shifted by a time offset greater than the GW travel time between the detector sites to generate years of ef-

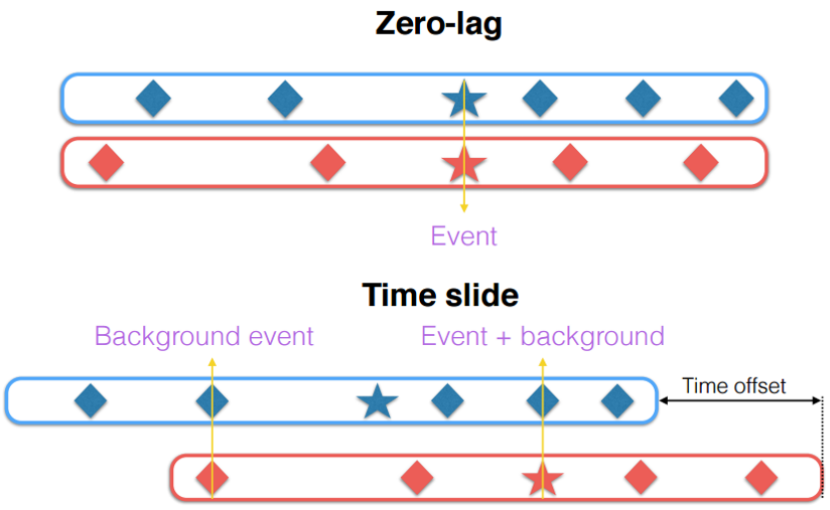

Figure 5.2: Method of time slides for FAR estimation. GW triggers are detected in zero-lag (top) and noise events are detected in time shifted data with offsets greater than the GW travel time between the detectors. (Figure from Laura Nuttall, 2017)

fective background. Then, the search pipeline analyzes this data (which must de facto be void of any real coincident gravitational waves) and the rate of noise events arising from uncorrelated noise sources occurring simultaneously is calculated.

Two-Dimensional Sky Localization Probability Maps

For O1, we wanted to provide our observing partners with prompt and accurate sky localization probability maps (skymaps) in order to increase their chances of finding electromagnetic/neutrino counterparts where time is of the essence (e.g., a rapidly fading X-ray/optical afterglow occurring within minutes to hours of a neutron star merger). Thus, low-latency source localization for CBC candidate events was provided by `BAYESTAR`, the BAYESian TriAngulation and Rapid localization pipeline (a pun on the powerful Cylon Basestar from *Battlestar Galactica*), which produced skymaps for follow-up on the order of ∼30 seconds to minutes (Singer & Price, 2016).

As we can see in Table 4.1, there are 11 total parameters, ϑ, that describe the physical properties of a compact binary coalescence. Given that Advanced LIGO and/or Virgo detects a gravitational-wave candidate in a data set $D_{\rm GW}$, we can write the posterior distribution, $P(\vartheta|D_{\rm GW})$, which describes the probability of the parameters given the data:

$$P(\vartheta|D_{\rm GW}) = \frac{P(D_{\rm GW}|\vartheta)P(\vartheta)}{P(D_{\rm GW})},$$

using Bayes' theorem. For purposes of localization, the only two parameters of interest are the right ascension and declination (α and δ), where all the other parameters are nuisance parameters (λ) that can be marginalized over, i.e., integrated away. Thus, we can write the marginal posterior:

$$P(\alpha, \delta|D_{\rm GW}) = \int P(\vartheta|D_{\rm GW})\ d\lambda = \int \frac{P(D_{\rm GW}|\vartheta)P(\vartheta)}{P(D_{\rm GW})} d\lambda,$$

which involves complicated multi-dimensional integrals that are in practice performed with the Markov chain Monte Carlo (MCMC) integration technique. However, Advanced LIGO and Virgo's source localization pipeline `LALInference` that utilizes a rigorous MCMC analysis takes on the order of hours to days and weeks, rendering it unhelpful for low-latency electromagnetic/neutrino follow-up. Thus, we utilize `BAYESTAR` which works with the maximum likelihood (ML) parameter estimates of the GW amplitude, coalescence phase, and arrival time at each detector as determined by the triggered template of the low-latency CBC search pipeline when producing GW triggers[3]. In this manner, the dimensionality of the original marginal posterior problem is greatly reduced and marginalization can be carried out using various methods of quadratures in a matter of seconds to minutes (e.g., Newton-Cotes for integrating over the polarization angle, Legendre-Gauss for cosine of the inclination angle, etc.) (Singer, 2015).

[3]In other words, for O1, `BAYESTAR` computed the triggered template's auto-correlation sequence to calculate the marginal posterior.

For O1, BAYESTAR produced two-dimensional (direction information only) skymaps packaged into convenient Flexible Image Transport System (FITS) files for CBC candidate events. These skymaps were created via GW triggers produced from the two Advanced LIGO detector network and therefore typically constrained the localization to ∼100 to 1000 deg^2 consisting of two long, thin sections of a great circle, one in the Northern hemisphere and one in the Southern hemisphere. In the event that the orbital plane of the binary is nearly face-on towards the Earth and the GW phases on arrival can be explained by two different binary inclination angles of opposite handedness, each arc-shaped mode features two narrow stripes at the ends resembling a snake's forked-tongue, aptly naming this feature the forked-tongue morphology.

We also sent low-latency two-dimensional (directional information only) skymaps for Burst GW candidate events (Essick et al., 2015). The latency for producing cWB skymaps is on the order of ∼minutes. Because the cWB low-latency search detection statistic is sensitive to the arrival times of the GW signal at different detector sites, it allows us to compute a constrained likelihood functional dependent on the source sky position (i.e., localization comes from a combination of time-delay information (triangulation) and amplitude coupling through the antenna patterns). Thus, the skymap is constructed by maximizing the constrained likelihood functional for all possible GW signals for the candidate event at each point in the sky.

The other low-latency Burst search oLIB uses LALInferenceBurst (LIB) to compute its skymaps. The latency for oLIB skymaps is higher, on the order of ∼hours to days, because LIB is an MCMC parameter estimation algorithm which uses sine-Gaussian templates for filtering. It reports a posterior in nine parameters, of which all parameters apart from sky position must be marginalized away to produce the skymap.

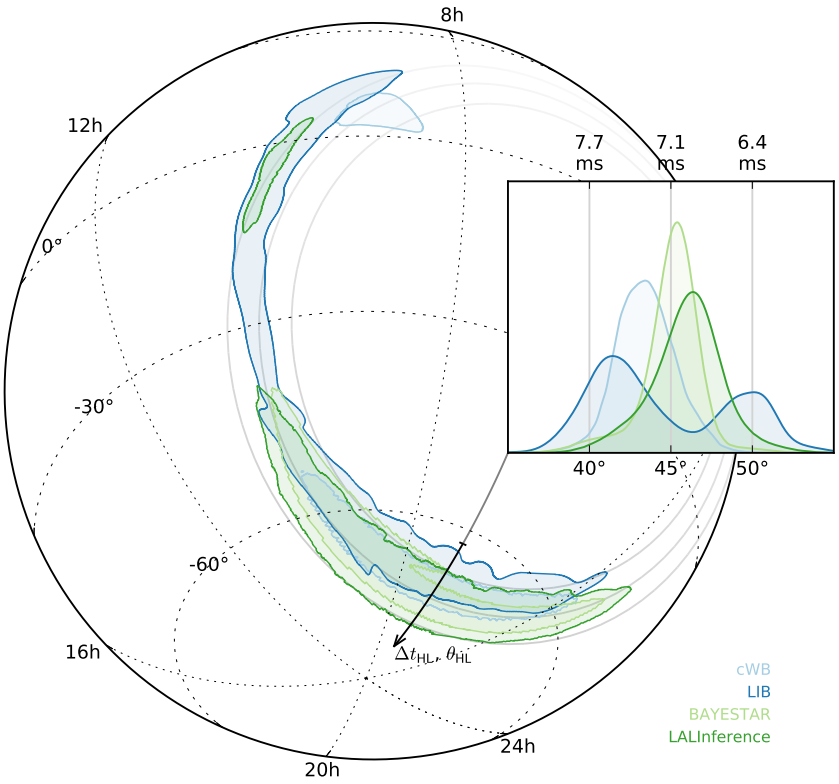

Figure 5.3: Comparison of the 90% credible regions from low-latency skymaps produced by `cWB`, `LIB`, and `BAYESTAR` for GW150914 displayed in an orthographic projection centered around the `LIB` localization. In light green is the offline full parameter estimation skymap produced by `LALInference`. The inset shows the distribution of the arrival time difference, Δt_{HL}, across the two Advanced LIGO detector network. (Figure from Abbott et al., 2016a)

In the case of short-duration compact binary coalescences (i.e., binary black hole mergers like GW150914) where the candidate event is detect by both CBC and Burst low-latency searches, we can compare the low-latency Burst skymaps to `BAYESTAR` (Figure 5.3). In this case, the CBC skymaps have much better localization (smaller credible regions) although most of the probability from both Burst and CBC skymaps will still contain the region around the true GW source location.

Chapter 6

O2: The Second Observing Run

The second observing run (O2) from November 30, 2016 to August 25, 2017 involved the two Advanced LIGO detectors in the United States joined by the Advanced Virgo detector in Italy for the last month of data-taking (starting August 1, 2017). During the course of O2, there were 8 confident gravitational-wave events: 7 of them stellar mass binary black hole mergers and 1 binary neutron star coalescence (Abbott et al., 2018). Of the 8 confident GW events, only 6 were found by the low-latency search pipelines and reported for EM/neutrino follow-up. The remaining 2 events (GW170729 and GW170818) were recovered by the offline search analyses.

Much of the work done to enable successful follow-up of low-latency GW candidates during O2 was documented in a LIGO Scientific Collaboration and Virgo Collaboration paper that I co-chaired with Sarah Antier, *Low-Latency Gravitational Wave Alerts for Multi-Messenger Astronomy During the Second Advanced LIGO and Virgo Observing Run* (Abbott et al., 2019). Our paper writing team included (in alphabetical order) Sarah Antier, Deep Chatterjee, myself, Shaon Ghosh, Giuseppe Greco, Barbara Patricelli, Karelle Siellez, and Koh Ueno. In this chapter, you will find more details on various sections from this paper.

In preparation for O2, I made upgrades (working with Reed Essick) to turn `approval_processor` into a multi-processing information-tracking software, `approval_processorMP`. This upgrade was inspired by the fact that during O1, each incoming LIGO-Virgo Alert (`LVAlert`) from approved low-

latency search pipelines triggered `approval_processor` to run, but it would begin its vetting process each time from scratch by querying GraceDb for GW trigger information. We wanted to cut down the latency of this process by preserving state information about the GW triggers and candidate events in local memory.

Other updates to `approval_processorMP` were planned simultaneously. Again, working with Reed Essick, I wrote additional software to "throttle" low-latency search pipelines if they overproduced GW triggers during a set time duration (as determined by Poisson statistics), signaling misbehavior in the streaming analysis and the need for `approval_processorMP` to ignore that pipeline's incoming GW triggers. This pipeline throttle feature was complete with an option to send commands to the live `approval_processorMP` process to un-throttle misbehaving pipelines, or to just let it run and wait until the pipeline settled down again. We debuted this upgrade during the middle of O2 and it was helpful in a handful of cases.

It was also during O2, I began working on the idea of a "grouper" (with help from Deep Chatterjee, who implemented the feature for O3) that would select the "superevent" out of a group of neighboring GW triggers for performing EM/neutrino follow-up. Although a beta version of this software ran during O2, it ran into problems regarding backlogging for loud GW triggers as described next.

All of these upgrades rendered the former `approval_processor` obsolete, although this came with its own drawbacks. We saw during the course of O2 that there were issues related to memory leakage (holding onto too many GW and external triggers' state information after many days to weeks of continuous live time, even with built-in functionality to expire old triggers), becoming a

zombie process that would stop responding to incoming `LVAlerts`, and (in the event of an interesting GW candidate event) getting backlogged by the untenable number of `LVAlerts` being generated for the group of GW triggers from different low-latency search pipelines (most of them GraceDb log comments that were not useful information to `approval_processorMP` for performing its checks).

Still, with active monitoring of `approval_processorMP`, we were able to successfully send the Initial LIGO/Virgo Notices with tremendously reduced (∼30 minutes to hours) latencies for O2 compared to hours (sometimes days) we saw in O1. Our efforts were well repaid with the first ever detection of a binary neutron star coalescence, GW170817, observed on August 17, 2017 (Abbott et al., 2017a), followed by its short gamma-ray burst counterpart, GRB 170817A, ∼1.7 s later detected by *Fermi*/GBM (the Gamma-ray Burst Monitor) (Goldstein et al., 2017) and *INTEGRAL*/SPI-ACS (the spectrometer anti-coincidence shield) (SPI-ACS) (Savchenko et al., 2017). There was also an unprecedented amount of EM/neutrino follow-up generated for GW170817, that led to the discovery of its kilonova, X-ray, and radio counterparts (Figure 6.3).

Thus, this chapter details additional information `approval_processorMP` sent to our observing partners during O2, to aid EM/neutrino follow-up efforts.

6.1 Information Sent to MOU Partners

EM-Bright Source Classification

For O2, a new low-latency source classification pipeline, `EM-Bright`, was created for CBC triggers. The purpose of `EM-Bright` was to provide our observing partners with two probabilities: one regarding the presence of at least one neutron star in the binary system (ProbHasNS), and the other regarding

the presence of remnant disk mass outside the final black hole (ProbHasRemnant). The motivation for creating `EM-Bright` was to generate more follow-up for compact binaries with neutron stars as they are more likely to be accompanied by an electromagnetic/neutrino counterpart. For instance, neutron star-black hole (NS-BH) mergers and binary neutron star (BNS) mergers are likely progenitors of short gamma-ray bursts if the neutron star tidally disrupts and a hot, massive (∼few percents of 1 $M_{\odot}$) accretion disk is formed around the remnant black hole.

The earliest CBC trigger information available for producing source classification information are the point estimates of the masses (m_1, m_2) and aligned spin components (χ_1, χ_2) of the two objects in the binary, with $m_1 \geq m_2$. The point estimates are provided by the low-latency search pipelines via the waveform template that triggered to give the lowest false alarm rate during the search. However, point estimates have associated uncertainties and are expected to be offset from the true component values. Thus, the `EM-Bright` pipeline constructs an ambiguity ellipsoid around the triggered point estimate using an effective Fisher formalism (Cho et al., 2013). Each ambiguity ellipsoid is constructed in the three-dimensional ($\mathcal{M}_c$, η, χ_1) parameter space where $\mathcal{M}_c = (m_1 m_2)^{3/5}/(m_1 + m_2)^{1/5}$ is the chirp mass and $\eta = m_1 m_2/(m_1 + m_2)^2$ is the symmetric mass ratio (Pannarale & Ohme, 2014). Additionally, the ambiguity ellipsoids are populated with 1000 points, i.e., ellipsoid samples, to enclose a region of 90% match within its boundary for a total of 1001 ellipsoid samples including the original point estimate. The twofold source classification probabilities are computed for each ellipsoid sample.

For the first classifer, ProbHasNS, only the mass of the secondary object, m_2, is required. Simply, `EM-Bright` checks whether $m_2 < 2.83\ M_{\odot}$ where 2.83 $M_{\odot}$ is the maximum neutron star mass allowed by the very stiff equation of

state, 2H EOS (Kyutoku et al., 2010, 2011), to err on the side of having more counterparts than not. ProbHasNS is the fraction of ellipsoid samples with this property.

The second classifier, ProbHasRemnant, is model-dependent and potentially requires more parameters than just the secondary mass. For instance, if the secondary mass indicates that the system is a BBH, i.e., $m_2 > 2.83\ M_\odot$, the system and all its ellipsoid samples are immediately classified as $\mathrm{EM}_{\mathrm{dark}}$, i.e., ProbHasRemnant is set to 0%. On the other hand, if the primary mass indicates that the system is a BNS, i.e., $m_1 \leq 2.83\ M_\odot$, the system and all its ellipsoid samples are classified as $\mathrm{EM}_{\mathrm{bright}}$, i.e., ProbHasRemnant is set to 100%, and we would highly recommend EM follow-up if the GW trigger is promoted to GW candidate event status.

In the case of NS-BH binaries, the `EM-Bright` pipeline adopted Foucart's fitting formula[1] (Foucart, 2012) to calculate the remnant disk mass, m_{rem}:

$$\frac{m_{\mathrm{rem}}}{m_{2,\mathrm{b}}} \approx 0.228 \left(\frac{3m_1}{m_2}\right)^{1/3} \left(1 - \frac{2m_2}{r_2}\right) - 0.148 \frac{r_{\mathrm{isco}}}{r_2}$$

where $m_{2,\mathrm{b}}$ is the baryon mass of the neutron star, m_1 and m_2 are the masses of the black hole and neutron star, r_2 is the radius of the neutron star calculated using the 2H EOS, and r_{isco} is the innermost stable circular orbit of the black hole which depends on the black hole's dimensionless spin parameter, χ_{bh}[2]:

$$\begin{aligned} Z_1 &= 1 + (1 - \chi_{\mathrm{bh}}^2)^{1/3} \left[(1 + \chi_{\mathrm{bh}})^{1/3} + (1 - \chi_{\mathrm{bh}})^{1/3}\right], \\ Z_2 &= \sqrt{3\chi_{\mathrm{bh}}^2 + Z_1^2}, \\ \frac{r_{\mathrm{isco}}}{m_1} &= 3 + Z_2 - \mathrm{sign}(\chi_{\mathrm{bh}}) \sqrt{(3 - Z_1)(3 + Z_1 + 2Z_2)}. \end{aligned}$$

[1] In Foucart's fitting formula, Newton's gravitational constant G, and the speed of light c, are both equal to 1.

[2] In our implementation of the `EM-Bright` pipeline, we assume that the spin of the black hole, χ_{bh}, is parallel to the orbital angular momentum. Similarly, our waveform models assume that the spins of the compact objects are aligned with the orbital angular momentum. Thus, $\chi_{\mathrm{bh}} = \chi_1$.

Thus, for each ellipsoid sample, $m_{\rm rem}$ is computed and ProbHasRemnant is the fraction of ellipsoid samples for which $m_{\rm rem}$ is greater than zero. This is because although remnant disk masses $\sim$0.03 $M_\odot$ could launch a GRB engine, masses as low as $\sim$0.01 $M_\odot$ are thought to be enough to generate a kilonova. Thus, we take a conservative lower limit of 0 $M_\odot$.

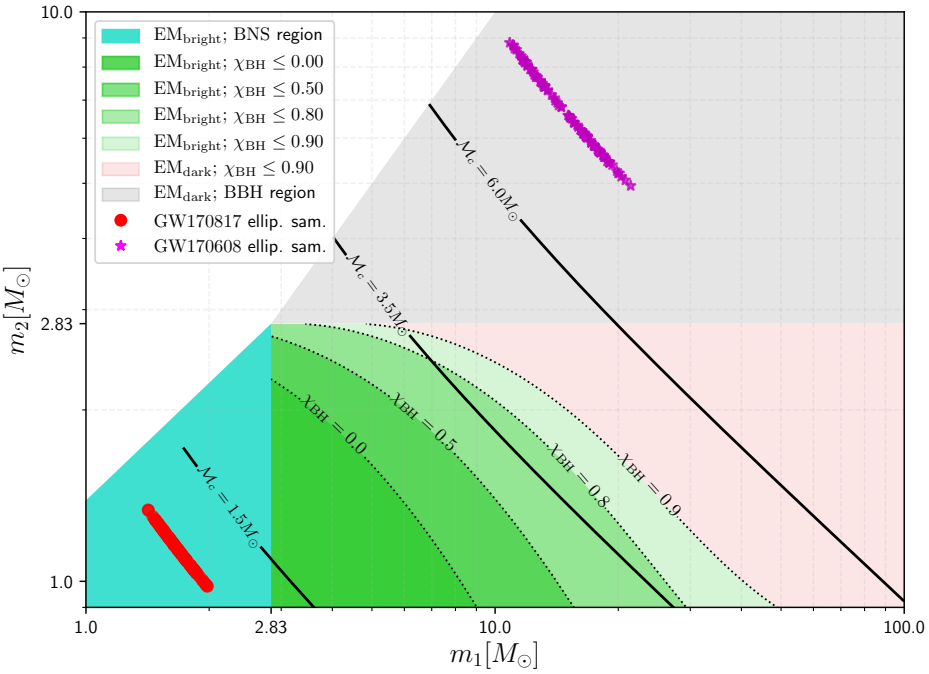

Figure 6.1: Different regions of the ellipsoid sample component mass parameter space. Foucart's fitting formula is applied for ellipsoid samples in the pink and green shaded NS-BH region. In particular, the χ_1-dependent green shaded regions reflect boundaries where ellipsoid samples give non-zero remnant disk mass. Additionally, ellipsoid samples for GW170817 (red dots in the cyan BNS/100% $\mathrm{EM_{bright}}$ parameter space) and GW170618 (purple stars in the grey BBH/0% $\mathrm{EM_{bright}}$ parameter space) are shown. (Figure from Deep Chatterjee/Abbott et al. (2019))

Qualitatively speaking, Foucart's fitting formula shows that the more symmetric the masses are, and the more the black hole spin component (which affects $r_{\rm isco}$) is aligned with the orbital angular momentum (i.e., the higher the

value of χ_1), the more likely it is that the neutron star will be sufficiently tidally disrupted (Figure 6.1). For instance, an ellipsoid sample with masses (7, 2) $M_\odot$ will give non-zero remnant disk mass according to Foucart's fitting formula if the value of χ_1 is slightly greater than 0.5, but no remnant disk mass below this value.

During O2, `EM-Bright` provided ProbHasNS and ProbHasRemnant source classification with a latency of a few minutes for CBC GW candidate events. This information was included in the machine-readable LIGO/Virgo Notices and in the human-prose LIGO/Virgo Circulars with a link to the `EM-Bright` technical document[3].

Three-Dimensional Sky Localization Probability Maps

For O2, we also sent our observing partners distance-resolved three-dimensional `BAYESTAR` skymaps for CBC gravitational-wave candidate events. This requires calculating the marginal posterior:

$$P(r, \alpha, \delta | D_{\rm GW}) = \int P(\vartheta | D_{\rm GW})\ d\lambda = \int \frac{P(D_{\rm GW}|\vartheta)P(\vartheta)}{P(D_{\rm GW})} d\lambda,$$

where λ are all the other parameters, i.e., "nuisance parameters", excluding r, α, and δ in the table of waveform parameters, ϑ (Table 4.1). This marginal posterior distribution can be written as the product of the two-dimensional (direction information only) skymap and the conditional distance distribution:

$$P(r, \alpha, \delta | D_{\rm GW}) = P(r | \alpha, \delta, D_{\rm GW}) P(\alpha, \delta | D_{\rm GW}),$$

which in O2 is computed using the matched-filter SNR time series (the cross-correlation sequence between the detector output and the template) versus the triggered template's auto-correlation sequence used in O1.

[3] https://dcc.ligo.org/public/0139/T1600571/010/Description_Document.pdf

However, the conditional distance distribution can be approximated using our intuition that along a given line of sight, the probability per unit distance (assuming that the GW source is in this direction) will be unimodal[4] and well-fit by a Gaussian ansatz (Singer et al., 2016):

$$P(r|\alpha,\delta,D_{\mathrm{GW}}) \approx \frac{\hat{N}(\alpha,\delta)}{\sqrt{2\pi}\hat{\sigma}(\alpha,\delta)} e^{-\frac{(r-\hat{\mu}(\alpha,\delta))^2}{2\hat{\sigma}^2(\alpha,\delta)}} r^2,$$

where $\hat{N}(\alpha,\delta)$, $\hat{\mu}(\alpha,\delta)$, and $\hat{\sigma}(\alpha,\delta)$ are the direction-dependent normalization coefficient, location parameter, and scale parameter, respectively for $r \geq 0$. (The r^2 at the end ensures that the probability density per unit volume vanishes at the origin.) The location parameter and its scale (i.e., standard deviation) of the ansatz distribution are calculated by fitting the ansatz to the true marginal posterior distribution using the method of moments.

Thus, similarly to O1, the three-dimensional (direction plus distance information) `BAYESTAR` skymaps are packaged into Flexible Image Transport System (FITS) files which are backwards compatible with software that read O1 style two-dimensional skymaps. Each skymap contains four columns in total (Table 6.1) such that the two-dimensional (direction information only) column, ρ_i, and the probabilities along all given lines of sight are normalized:

$$\sum_{i=0}^{N-1} \rho_i = 1, \text{ and}$$
$$\sum_{i=0}^{N-1} \int_0^\infty P(r,\mathbf{n}_i)\, dr = 1,$$

where N is the total number of pixels, $\mathbf{n}_i$ is the direction of the i^{th} pixel, and $P(r,\mathbf{n}_i)$ is the approximate marginal posterior probability distribution in spherical polar coordinates:

$$P(r,\mathbf{n}_i) = \rho_i \frac{\hat{N}_i}{\sqrt{2\pi}\hat{\sigma}_i} e^{-\frac{(r-\hat{\mu}_i)^2}{2\hat{\sigma}_i^2}} r^2.$$

[4]The SNR of the GW candidate event is a degenerate combination of luminosity distance plus binary inclination angle. The unimodality of the distance comes the broad, universal distribution of the binary inclination angle arising from the Malmquist bias.

Column	Information
1. ρ_i	probability contained in pixel i (i.e., the two-dimensional skymap)
2. $\hat{\mu}_i$	mean of location distance in direction of pixel i
3. $\hat{\sigma}_i$	standard deviation of location distance in direction of pixel i
4. $\hat{N}_i$	normalization coefficient for pixel i

Table 6.1: Information columns in three-dimensional `BAYESTAR` skymaps.

When the three-dimensional skymaps are plotted in totality, they have a non-trivial geometry for candidate events from the two Advanced LIGO detector network. The two long, thin sections of a great circle that are typical of two-dimensional skymaps now become two thin, rounded, slightly oblique petals in three dimensions. The forked-tongue morphology that arises from binary inclination angle degeneracy when the binary's orbital plane is nearly face-on towards the Earth now becomes narrow crevices that run along the outer edges of the petals. All in all, these two-detector three-dimensional `BAYESTAR` skymaps end up looking like jacaranda tree seeds or space potato chips. In the three-detector Advanced LIGO plus Advanced Virgo network, one can imagine the two-dimensional islands of directional probabilities turning into spindles when including distance information.

When these three-dimensional skymaps are used to follow-up on binary neutron star candidate events, they are helpful in multiple ways. First, we can reduce the area to be searched over because the nearness of the event to the local Universe allows us to combine the skymap with a galaxy catalog (e.g., the Galaxy List for the Advanced Detector Era[5] (Dálya et al., 2018)). This way, nearby galaxies with consistent redshifts can be targeted for follow-up. Second, expanding on the first idea, we can also minimize the total exposure time required to observe every galaxy in the 90% credible volume by applying a flux limit and taking into consideration the type of instrument used for follow-

[5] http://aquarius.elte.hu/glade

up (e.g., large versus small field of view, etc.) (Singer et al., 2016). Lastly, distance estimates allow us to exclude false positive transient electromagnetic counterpart candidates.

6.2 The Advanced Virgo Detector

Starting August 1, 2017, Advanced Virgo, the European ground-based interferometric GW detector in Cascina, Italy with 3 km-long arms (Acernese et al., 2015), joined the Advanced LIGO detector network for the last month of data acquisition. Because Advanced Virgo was still being commissioned during most of its run for O2, the low-latency search pipelines set lower SNR thresholds for triggering using its data (Table 4.3), or did not use it at all in the case of `PyCBC Live`. However, once a GW trigger made it to the candidate event stage, Advanced Virgo data were used in the post-processing skymap generation. For the real events GW170814 and GW170817, Advanced Virgo played a critical role in improving the localization down to ∼tens of square degrees for the 50% confidence regions. In the case of GW170817, the binary neutron star coalescence came from a direction near a node of the Advanced Virgo detector. The weak signal there was still enough to help constrain the localization and break down the degeneracy using data from the two Advanced LIGO detectors only (Figure 6.2).

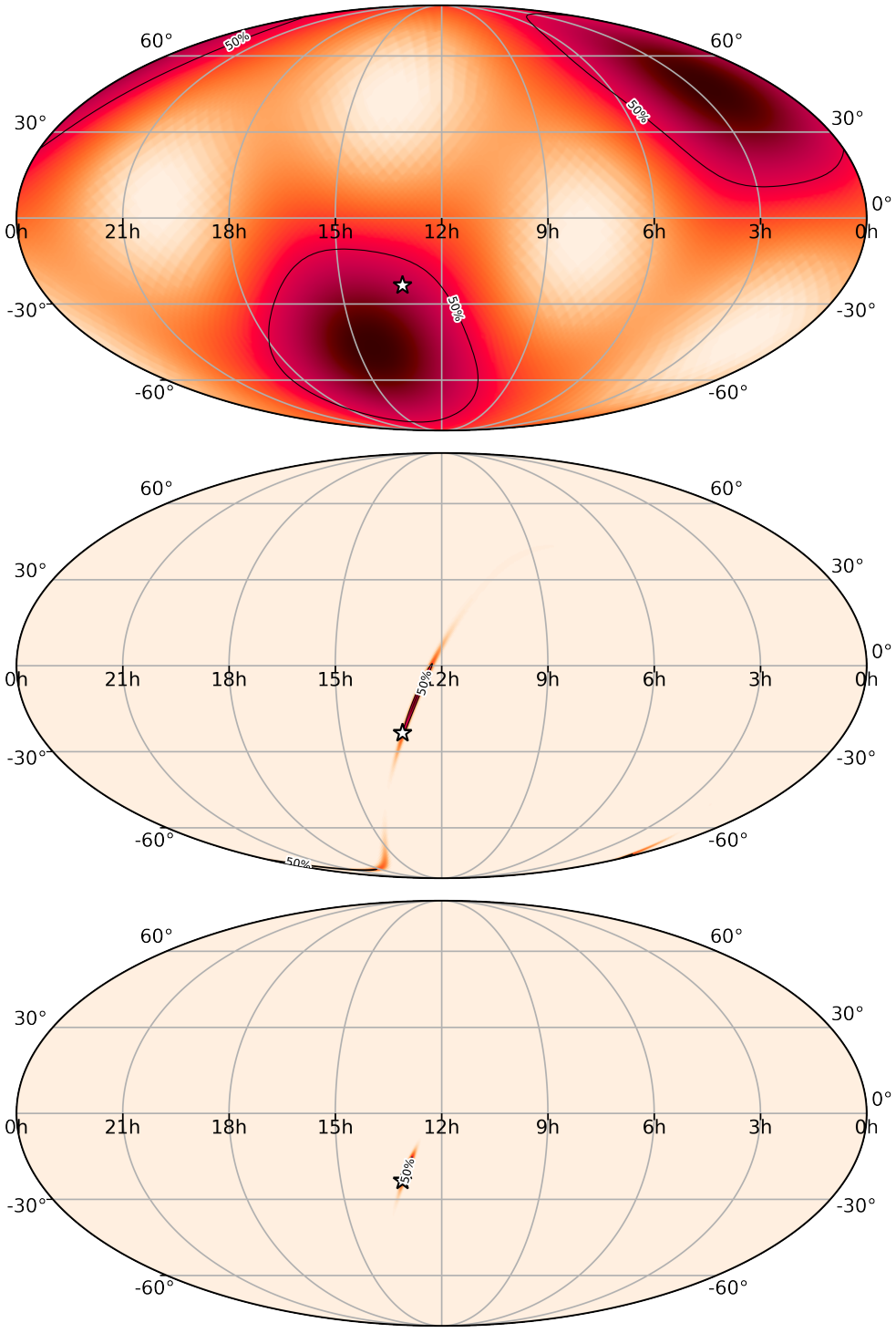

Figure 6.2: `BAYESTAR` skymaps for GW170817 in ICRS coordinates (Mollweide projection) from a 1-detector network (top, Advanced LIGO/Hanford), 2-detector network (center, Advanced LIGO), and 3-detector network (bottom, Advanced LIGO and Advanced Virgo). The 50% confidence region and the location of the host galaxy NGC 4993 (marked with a star) are shown.

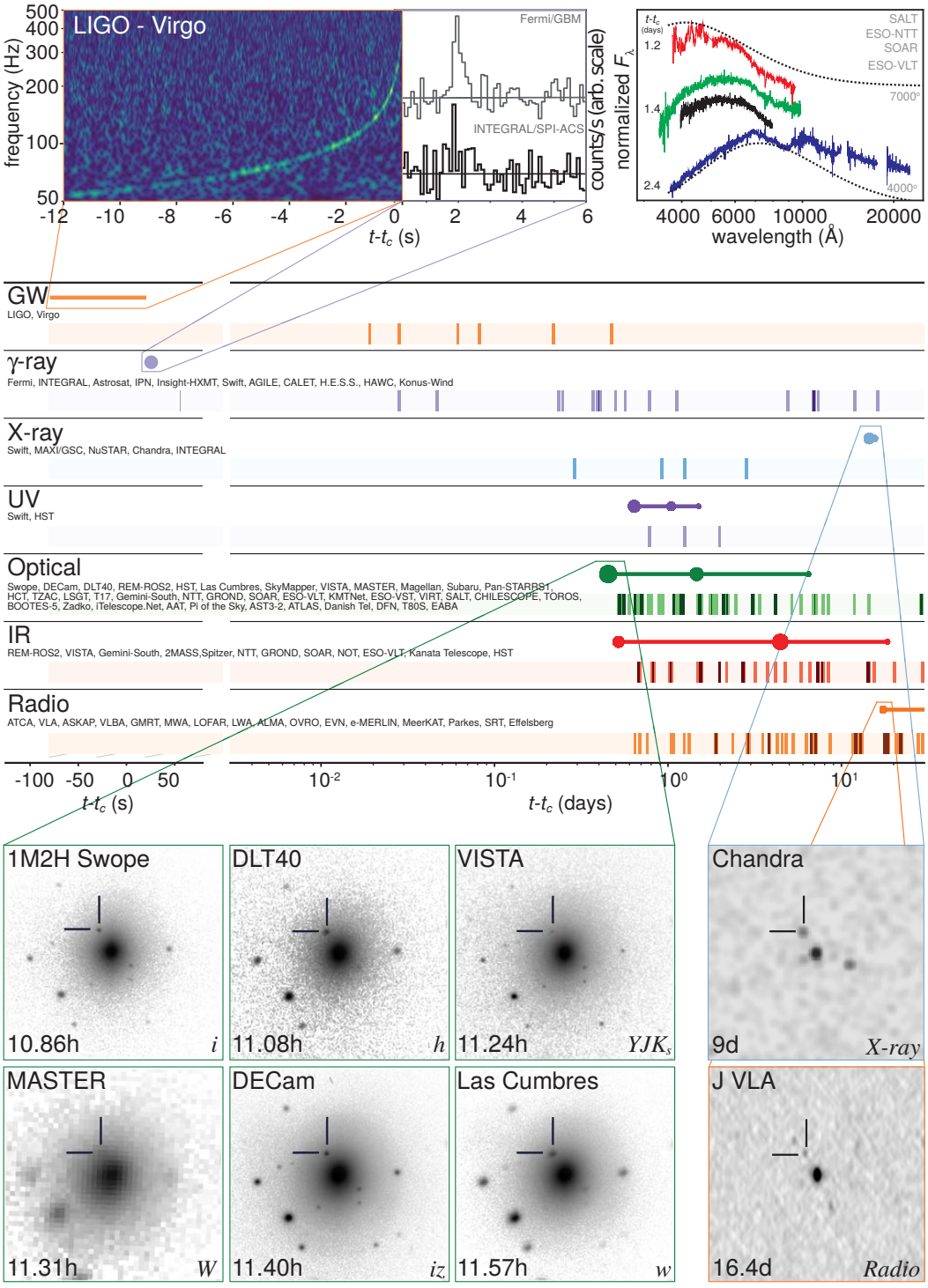

Figure 6.3: Electromagnetic follow-up of the first observed binary neutron star coalescence event, GW170817. This is also the first multi-messenger event involving gravitational waves. (Figure from Abbott et al., 2017b)

Chapter 7

Cosmic Strings

Between the second and third observing runs, I joined LIGO and Virgo's Burst cosmic strings analysis group, consisting of myself, Imène Belahcene, Kipp Cannon, Florent Robinet, and Daichi Tsuna. We performed a matched filter based search looking for GW bursts from cosmic string cusps. In this chapter I present our goals and search methods, and include our results from analyzing O2 data, which are officially included in the "O2 Burst All-Sky Paper" titled *All-sky search for short gravitational-wave bursts in the second Advanced LIGO and Virgo run* (Abbott et al., 2018a).

7.1 Basic Properties

The Universe has gone through several phase transitions since the Big Bang, leaving behind clues such as the Cosmic Microwave Background (CMB), created by photons scattering off hot, dense, ionized matter (i.e., the last scattering surface) before the Universe cooled down sufficiently enough for electrons to recombine into atoms, and for photons to cease scattering and propagate freely. Thus, while the CMB provides a snapshot of the Universe ∼377,000 years after the Big Bang, it is the limit of an electromagnetic probe of the history of the Universe. Gravitational waves, on the other hand, may penetrate through this last scattering surface, to provide clues about large-scale mass and energy transitions and distributions in the early Universe. In this respect, we are motivated to study and search for gravitational waves from a more speculative source known as cosmic strings.

Strings vs. Superstrings

There are two viable contexts in which cosmic strings arise. In the framework of Grand Unification Theories (GUTs), they are linear topological defects (similar to vortex filaments in superfluid helium) formed during the grand unification epoch (or any axial or cylindrical symmetry-breaking phase transition of the early Universe) (Sakellariadou, 2007). In the framework of String Theory, they are called cosmic superstrings, which are coherent macroscopic states of fundamental F-strings and Dirichlet D-strings (Copeland et al., 2004). Strings and superstrings have different intercommutation probabilities, p, which is the probability that a string/superstring will swap partners or chop itself off/form a loop when intersecting with itself or another string/-superstring. Cosmic strings from GUTs have $p = 1$ while cosmic superstrings have $p < 1$.

If they exist, cosmic strings and superstrings are topologically stable objects with finite widths that are less then a trillion times smaller than the radius of a hydrogen atom. Thus, their large-scale dynamics can be described using a zero-width approximation known as the Nambu-Goto action in a low-density (or otherwise empty) Universe (Copeland & Kibble, 2009). However, strings also have a string tension, $G\mu$ ($c = 1$, where μ is the mass per unit length), and due to their cosmological sizes, emit gravitational waves in a number of different ways when they intersect/interact with one another and themselves.

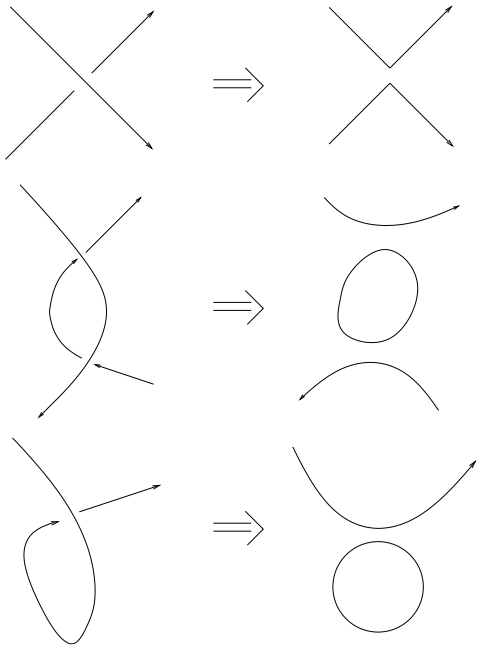

Figure 7.1: Types of cosmic string intersections where the intercommutation probability, p, is assumed to be 1. From top to bottom: string-string intersection at one point (two new long strings are formed via partner exchange), string-string intersection at two points (two new long strings are formed via partner exchange plus one closed loop), and self-string intersection (one long string and a closed loop are formed). (Figure from Sakellariadou, 2007)

Loops, Cusps, and Kinks

Loops are created when strings interact with themselves or each other (Figure 7.1), providing several gravitational-wave signatures (and a way for strings to lose energy/not dominate the energy density of the Universe). During the "looping off" process, discontinuities appear along the tangent vector of the original string(s), which are called kinks. The loops that are created also oscillate periodically under their own tension, typically creating cusps, which are points along the loop that accelerate to momentarily reach the speed of light (Figure 7.2). The density of cusps in a network of strings depends on the strings' intercommutation probability, p. We consider for the O2 Burst cosmic strings analysis, gravitational waves emitted from individual cusps, which are

well-modeled and can be searched for with matched filter templates (Damour & Vilenkin, 2000).

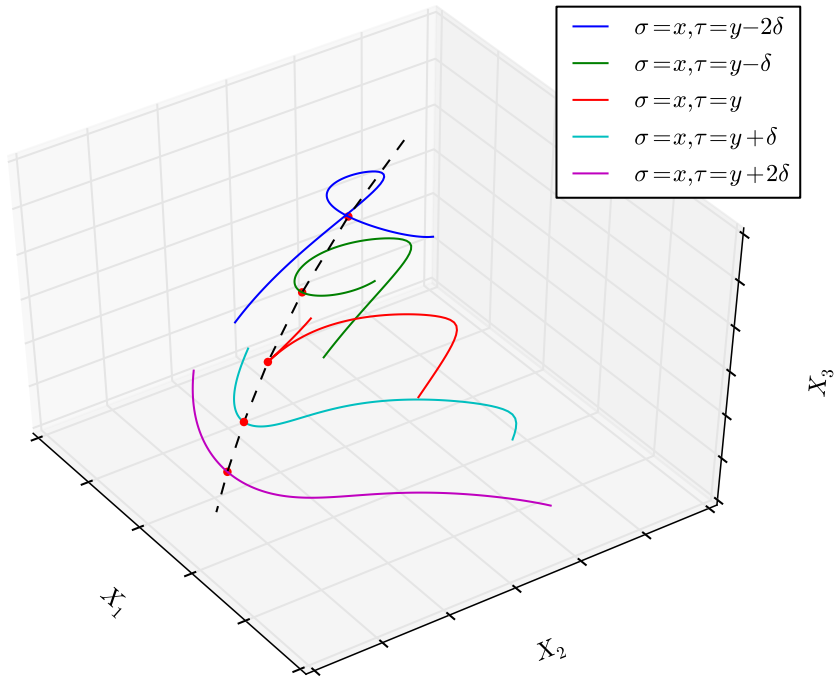

Figure 7.2: Time evolution (dotted black line) of a point along a string (red dot) that becomes a cusp at time $\tau = y$, starting with a string intersecting itself at time $\tau = y - 2\delta$. (Figure from Stott et al., 2017)

7.2 Cosmic String Cusps Search Algorithm

Gravitational waves from cosmic string cusps follow a $f^{-4/3}$ power law at high frequencies:

$$h(f) = A(z, l, G\mu) f^{-4/3} \Theta(f_h - f) \Theta(f - f_l)$$

in the frequency domain, where Θ is the Heaviside function, and f_l/f_h are the low/high frequency cutoffs of the gravitational-wave signal (Stott et al., 2017). In practice, the low frequency cutoff is determined by the sensitivity of the gravitational-wave detectors, $\sim$10 Hz due to seismic noise, and the high frequency cutoff is determined by the angle between the line of sight of the observer and the direction of the beamed gravitational-wave signal. The

amplitude, A, is a function of the redshift-dependent distance to the source $r(z)$, string length l, and string tension $G\mu$.

To perform the analysis, we divided O2 data into 6 separate chunks, each one of duration $1-2$ months, where chunk boundaries were positioned to coincide with significant detector maintenance breaks (Table 7.1). 31 templates with varying high frequency cutoffs, 30 Hz $< f_h <$ 4096 Hz, were used for the matched filtering. The lowest high frequency cutoff of 30 Hz corresponds to the maximum angle between the line of sight and the beamed gravitational-wave signal.

Chunk	**Start**	**End**
28	1164499217	1166486417
29	1167523218	1170547218
30	1170547218	1178323218
31	1179792018	1183420818
32	1183420818	1185580818
33	1185580818	1187740818

Table 7.1: O2 data were divided into 6 chunks for the Burst cosmic strings analysis. All start and end times are in GPS time.

The search detection pipeline works as follows. Single-detector triggers are recovered from each detector data set and then combined when performing the coincidence search. In zero-lag, detector data are shifted temporally within the bounds of the gravitational-wave travel time between detectors, allowing us to find candidate events. When time slides offset the detector data with times greater than the GW travel time between detectors, accidental noise coincidences are found. A multivariate log-likelihood ratio is then computed for each coincident trigger (candidate events and noise events) to be used for ranking.

We ran two parallel analyses twice using O1 reviewed software and O2

updated software. For the first parallel analyses, C00 "raw" data (including data from Virgo in Chunk 33) were used after CAT 1[1] data quality vetoes were removed. The search determined that all 5 loudest events originated from Chunk 33/Virgo, and found four useful data quality flags: two from the `UPV` (Used Percentage Veto) data quality pipeline which uses statistical correlations between witness sensor channels and the GW strain channel (similar to `iDQ`) to determine noisy times, and one data quality flag each for control system glitches and photodiode glitches.

The parallel analyses also showed slight discrepancies in the loudest recovered events from the two pipelines which allowed us to track down bugs that had been fixed by hand during O1, and bugs introduced during updates to the parent software repository `LALsuite` (LIGO Algorithm Library Suite). Once these were fixed, for the second parallel analyses, we used C02 "clean" data (excluding Virgo data) after CAT 1 and CAT 4[2] data quality vetoes were removed.

[1]CAT 1 data quality flags determine times of critical issues with a key detector component not operating in its nominal configuration.

[2]CAT 4 data quality flags exclusively remove transient hardware injections.

7.3 Search Results

From the second parallel analyses, we found a total of 69,554 zero-lag cosmic string cusp candidate events (i.e., coincident triggers) from $\sim 10^7$ s of coincident time between the two Advanced LIGO detector data sets. The highest ranked candidate event had a log-likelihood ratio of ~ 9 ($\lambda_{\max} \sim 8178$), within 1σ of the expected background distribution (Figure 7.4a). To construct the 5.8×10^{10} s $\approx 1,846.7$ yr of effective background, we used 6000 time slides with ~ 3.5 s offsets. We also investigated the three loudest triggers (Table 7.2) with `Omicron` power scans and discovered they were all consistent with tomte blip glitches[3] (Figure 7.3).

Rank	Detector	Peak Time	SNR	Log-Likelihood
1	H1	1185584772.3114	3.82	9.01
	L1	1185584772.31958	9.43	
2	H1	1175720634.21753	3.92	8.03
	L1	117572063.21716	9.01	
3	H1	1175010906.68774	4.79	7.48
	L1	1175010906.68872	7.72	

Table 7.2: The three loudest zero-lag cosmic string cusp candidate events identified during O2. H1 and L1 stand for the Advanced LIGO/Hanford and Advanced LIGO/Livingston detectors respectively.

We also estimate the sensitivity of our search pipeline by injecting a few million random simulated signals of known amplitude A into the data. The detection efficiency, $e(A)$, is defined as the fraction of simulated signals recovered with log-likelihood greater than $\ln \lambda_{\max}$ (Figure 7.4b).

7.4 Constraints

Lastly, even without a confirmed GW detection, we can constrain the ($G\mu$, p) parameter space for two Nambu-Goto large loop distribution models

[3] Tomte blip glitches are a class of glitches with peak frequencies less than 100 Hz, named after the Scandinavian mythological creatures, tomte, whose tall skinny hats resemble the morphology of this glitch class in the TF domain.

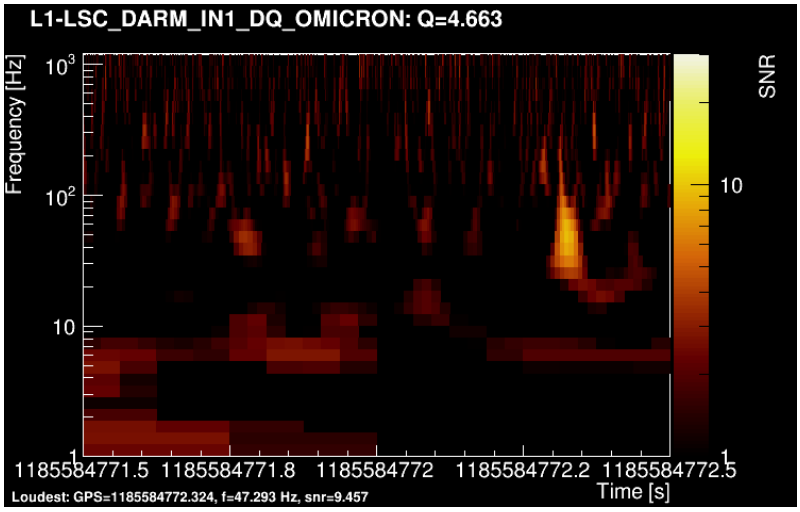

Figure 7.3: An `Omicron` scan of the highest-ranked zero-lag cosmic string cusp candidate event revealed it to be consistent with a tomte blip glitch in Advanced LIGO/Livingston. Because we expect at least one candidate event to have occurred by accident due to noise processes, results of the search are consistent with the hypothesis that there are no signals present.

developed for topological strings (i.e., $p = 1$): the Blanco-Pillado et al. model (Blanco-Pillado et al., 2014) and the Ringeval et al. model (Lorenz et al., 2010), which were studied during the first observing run. Because it is unknown how the loop densities scale with p for cosmic superstrings, we assume for our purposes that they scale as $1/p$.

Then, for each model, M, we can write the effective detection rate:

$$\mathscr{R}^{(\mathrm{M})}(G\mu, p) = \int_0^\infty e(A)\ dA \times \int_0^\infty \frac{d^2\mathcal{R}^{(\mathrm{M})}}{dz dA}(A, z, f^*; G\mu, p)\ dz,$$

where $e(A)$ is the detection efficiency curve using the log-likelihood of the loudest candidate event in the search, $d^2\mathcal{R}^{(\mathrm{M})}/dz\ dA$ (or equivalently, $d^2\mathcal{R}^{(\mathrm{M})}/dz\ dh$, $h = Af^{-4/3}$), is the rate at which cosmic string cusps create GW bursts in a loop distribution model M and f^* is the lowest high-frequency cutoff used in the template searches (i.e., 30 Hz) (Abbott et al., 2018b). We can now constrain the parameter space of model M by excluding regions where cosmic string cusps of a given string tension $G\mu$ and intercommutation probability p

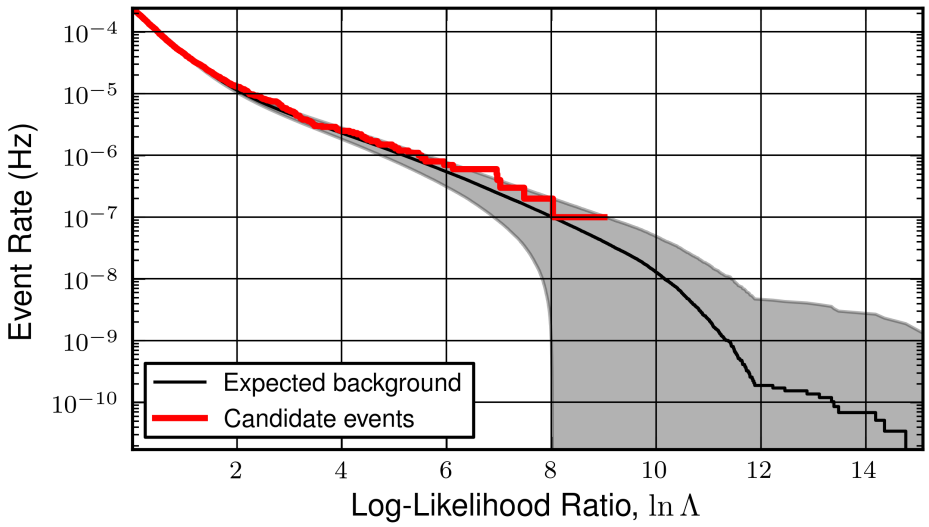

(a) Cumulative event rate as a function of the log-likelihood ratio ranking statistic. The black line and shaded region are the expected background distribution (with $\pm 1\sigma$ statistical error). The upper corners of the steps in the red line are the 69,554 zero-lag candidate events, all consistent with background.

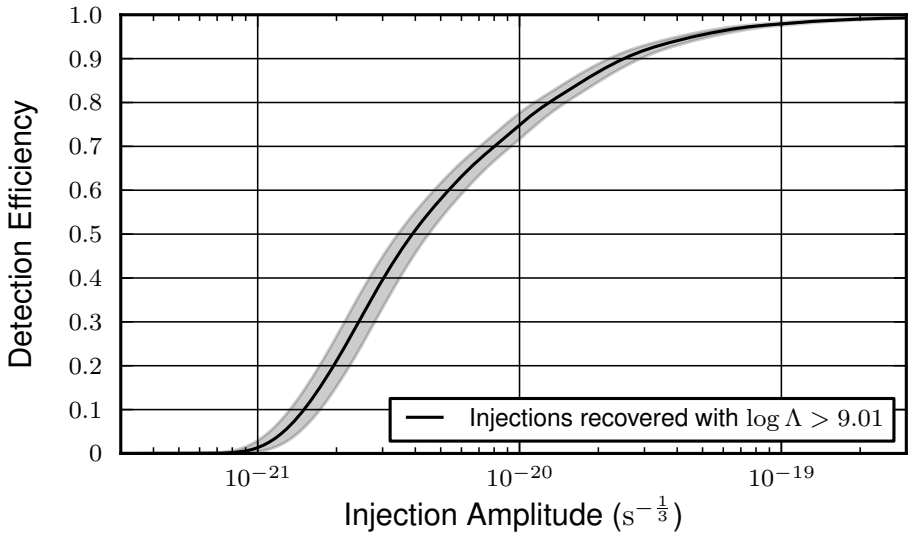

(b) Search detection efficiency as a function of the cosmic string cusp signal amplitude. The detection efficiency is defined as the fraction of simulated cusp events recovered with log-likelihood greater than ∼9.

Figure 7.4: O2 Burst cosmic string cusp search results.

would have registered with our analysis pipeline with log-likelihoods as loud as that of our most significant candidate event. The 95% confidence exclusion

regions are shown in Figure 7.5. It is important to stress that the models studied were derived for topological strings ($p = 1$) and therefore, only the string tension of the Ringeval et al. model was constrained to be less than $\sim 4.2 \times 10^{-10}$.

In the parameter space where we have chosen to report results (the large loop regime), the Stochastic cosmic strings search, which looks for the gravitational-wave background created by the superposition of multiple, unresolved cusps and kinks, is more sensitive and therefore places tighter constraints on the intercommutation probability and string tension.

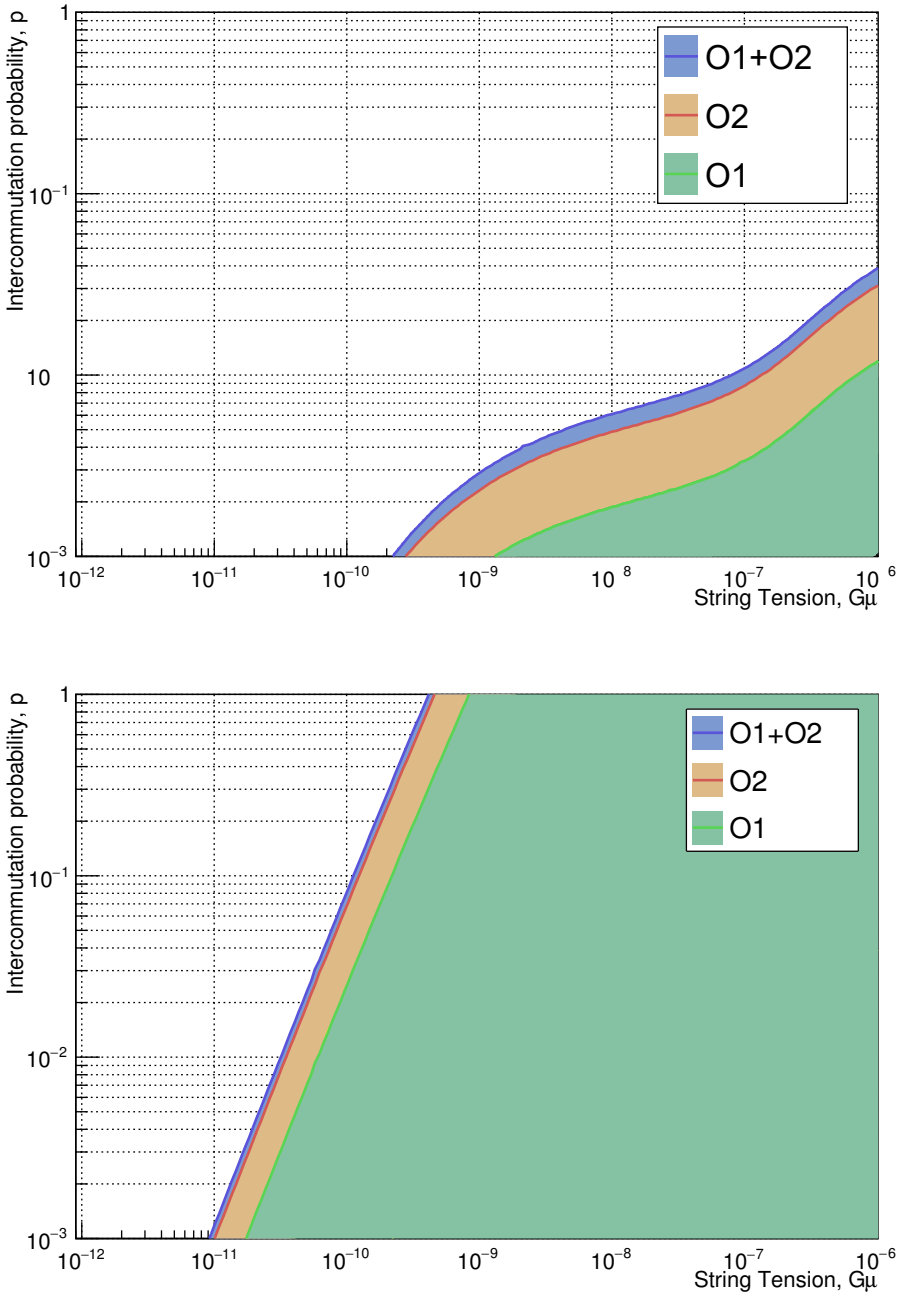

Figure 7.5: 95% confidence exclusion regions for cosmic string tension and intercommutation probability from the LIGO and Virgo Burst cosmic strings analysis group using O1 and O2 data for two large loop Nambu-Goto cosmic string distribution models. The excluded regions are below the respective curves. At $p = 1$ for topological strings, we cannot put a constraint on the string tension for the Blanco-Pillado et al. model (top, Blanco-Pillado et al. (2014)). However, for the Ringeval et al. model (bottom, Lorenz et al. (2010)), the string tension must be less than $\sim 4.2 \times 10^{-10}$. (Figures from Florent Robinet, 2018)

Chapter 8

En Route to O3: The Third Observing Run

8.1 Low-Latency Gravitational Wave-Electromagnetic and Neutrino Counterpart Coincidence Searches

For the third observing run, O3, I updated and built upon an analysis pipeline known as `RAVEN` (the Rapid, on-source VOEvent Coincidence Monitor), created by Alex Urban during the first and second observing runs, O1 and O2. `RAVEN`'s responsibility is to perform low-latency searches for temporally coincident external triggers and gravitational-wave candidate events. When the coincidence involves a gamma-ray burst (GRB), `RAVEN` also computes the false alarm rate (FAR) that this could be due to noise in the gravitational-wave detectors being temporally and/or spatio-temporally coincident with a real GRB.

Temporal Coincidence Searches

During O1 and O2, for each external trigger entering GraceDb, `RAVEN` looked for gravitational waves in two time windows, $[-5, +1]$ s and $[-600, +60]$ s, around the event time of the external trigger. The time windows were selected based off models of compact binary mergers (Metzger & Berger, 2012) and supernova emissions, where time delays could be due to differences in emission times and/or propagation speeds of the gravitational waves and electromagnetic/neutrino counterparts. Reciprocal searches were also performed[1]

[1]Reciprocal searches are necessary because of latencies in reporting either the external trigger or the gravitational-wave candidate event to GraceDb.

for each new gravitational-wave candidate event entering GraceDb. These searches looked for external triggers in time windows, [−1, +5] s and [−60, +600] s, around the gravitational-wave event time.

For O3, I made `RAVEN` discern between the two types of external triggers (GRBs versus supernova (SN) neutrinos) and two types of gravitational-wave events (modeled/compact binary coalescences versus unmodeled/generic transient bursts) entering GraceDb. In general, we expect short GRBs to be coincident with neutron star binary coalescences and SN neutrinos to be coincident with SN gravitational-wave bursts. However, complications arise because long GRBs could be associated with supernovae with rotating progenitors. Thus, the searches are performed as follows: for a GRB external trigger reported by *Swift* or *Fermi*, we look for modeled compact binary coalescences within [−5, +1] s and for unmodeled bursts within [−600, +60] s of the external trigger event time. For a neutrino reported by SNEWS (Supernova Early Warning System), we look for unmodeled bursts within [−600, +60] s of the external trigger event time. The reciprocal searches are as follows: for modeled compact binary coalescences, we look for external triggers within [−1, +5] s of the gravitational-wave event time, and for unmodeled burst transients, we look for external triggers within [−60, +600] of the gravitational-wave event time.

Gravitational Wave-Gamma-Ray Burst Coincidences

In the event that `RAVEN` finds a coincidence involving a GRB, `RAVEN` can compute a corresponding false alarm rate that the coincidence is in fact due to noise in the gravitational-wave (GW) detectors being coincident with a real GRB. The derivation for the FAR computation was first detailed and outlined by Michał Was within a Bayesian framework (à la Ashton et al. (2018)) and is re-derived here.

Suppose *Fermi* or *Swift* detects a GRB candidate in data set $D_{\rm GRB}$ and Advanced LIGO and/or Virgo detects a gravitational-wave (GW) candidate in data set $D_{\rm GW}$. We want to compute the Bayes factor that compares the common-source hypothesis $\mathcal{H}^{\rm C}$ (both GRB and GW detections are real and of a common-source origin) to the signal/noise hypothesis $\mathcal{H}^{\rm SN}$ (GRB is real but GW is noise):

$$\mathcal{B}_{\rm C/SN}(D_{\rm GRB}, D_{\rm GW}) = \frac{P(D_{\rm GRB}, D_{\rm GW}|\mathcal{H}^{\rm C})}{P(D_{\rm GRB}, D_{\rm GW}|\mathcal{H}^{\rm SN})}.$$

In the common-source hypothesis, the GRB and GW share common-source parameters such as source direction/orientation, luminosity distance, characteristic time of the event (emission times related by compact binary merger models), etc. Thus, the likelihood must be computed as follows:

$$\begin{aligned} P(D_{\rm GRB}, D_{\rm GW}|\mathcal{H}^{\rm C}) &= \int_{\Theta} P(D_{\rm GRB}, D_{\rm GW}, \theta|\mathcal{H}^{\rm C}) d\theta \\ &= \int_{\Theta^{\rm S}} P(D_{\rm GRB}, D_{\rm GW}|\theta, \mathcal{H}^{\rm C}) P(\theta|\mathcal{H}^{\rm C}) d\theta, \end{aligned}$$

where $\Theta^{\rm S}$ is the region of parameter space where $P(\theta|\mathcal{H}^{\rm C}) > 0$.

The first part of the integrand, $P(D_{\rm GRB}, D_{\rm GW}|\theta, \mathcal{H}^{\rm C})$, can be rearranged as follows:

$$\begin{aligned} &P(D_{\rm GRB}, D_{\rm GW}|\theta,\mathcal{H}^{\rm C}) \\ &\quad = P(D_{\rm GRB}|D_{\rm GW}, \theta, \mathcal{H}^{\rm C}) P(D_{\rm GW}|\theta, \mathcal{H}^{\rm C}) \\ &\quad = P(D_{\rm GRB}|\theta, \mathcal{H}^{\rm C}) P(D_{\rm GW}|\theta, \mathcal{H}^{\rm C}) \\ &\quad = \frac{P(D_{\rm GRB}|\mathcal{H}^{\rm C}) P(\theta|D_{\rm GRB}, \mathcal{H}^{\rm C})}{P(\theta|\mathcal{H}^{\rm C})} \frac{P(D_{\rm GW}|\mathcal{H}^{\rm C}) P(\theta|D_{\rm GW}, \mathcal{H}^{\rm C})}{P(\theta|\mathcal{H}^{\rm C})}, \end{aligned}$$

where we have just used Bayes' Theorem[2] in the second to third line. Substi-

[2]Bayes' Theorem is:

$$P(A|B) = \frac{P(A \cap B)}{P(B)} = \frac{P(B|A)P(A)}{P(B)}.$$

tuting this into the integral gives us:

$$\begin{aligned}
&P(D_{\rm GRB},D_{\rm GW}|\mathcal{H}^{\rm C}) \\
&\qquad = \int_{\Theta^{\rm S}} P(D_{\rm GRB}, D_{\rm GW}|\theta,\mathcal{H}^{\rm C})P(\theta|\mathcal{H}^{\rm C})d\theta \\
&\qquad = \int_{\Theta^{\rm S}} \frac{P(D_{\rm GRB}|\mathcal{H}^{\rm C})P(\theta|D_{\rm GRB},\mathcal{H}^{\rm C})P(D_{\rm GW}|\mathcal{H}^{\rm C})P(\theta|D_{\rm GW},\mathcal{H}^{\rm C})}{P(\theta|\mathcal{H}^{\rm C})}d\theta \\
&\qquad = P(D_{\rm GRB}|\mathcal{H}^{\rm C})P(D_{\rm GW}|\mathcal{H}^{\rm C})\int_{\Theta^{\rm S}} \frac{P(\theta|D_{\rm GRB},\mathcal{H}^{\rm C})P(\theta|D_{\rm GW},\mathcal{H}^{\rm C})}{P(\theta|\mathcal{H}^{\rm C})}d\theta \\
&\qquad = P(D_{\rm GRB}|\mathcal{H}^{\rm C})P(D_{\rm GW}|\mathcal{H}^{\rm C})\mathcal{I}_\theta(D_{\rm GRB}, D_{\rm GW}),
\end{aligned}$$

where the integral in the last line is the posterior overlap integral which quantifies the agreement in the posterior parameter distributions derived independently from each data set.

Then, the Bayes' factor comparing the common-source hypothesis to the signal/noise hypothesis becomes:

$$\begin{aligned}
\mathcal{B}_{\rm C/SN}(D_{\rm GRB}, D_{\rm GW}) &= \frac{P(D_{\rm GRB}, D_{\rm GW}|\mathcal{H}^{\rm C})}{P(D_{\rm GRB}, D_{\rm GW}|\mathcal{H}^{\rm SN})} \\
&= \frac{P(D_{\rm GRB}|\mathcal{H}^{\rm C})P(D_{\rm GW}|\mathcal{H}^{\rm C})}{P(D_{\rm GRB}|\mathcal{H}^{\rm S}_{\rm GRB})P(D_{\rm GW}|\mathcal{H}^{\rm N}_{\rm GW})}\mathcal{I}_\theta(D_{\rm GRB}, D_{\rm GW}).
\end{aligned}$$

However, in the special case of a true common-source astrophysical event, we expect:

$$P(\theta|\mathcal{H}^{\rm C}) = P(\theta|\mathcal{H}^{\rm S}_{\rm GRB}) = P(\theta|\mathcal{H}^{\rm S}_{\rm GW})$$

to be true, which leads to:

$$\frac{P(D_{\rm GRB/GW}|\mathcal{H}^{\rm C})}{P(D_{\rm GRB/GW}|\mathcal{H}^{\rm N}_{\rm GRB/GW})} = \frac{P(D_{\rm GRB/GW}|\mathcal{H}^{\rm S}_{\rm GRB/GW})}{P(D_{\rm GRB/GW}|\mathcal{H}^{\rm N}_{\rm GRB/GW})} \text{ , i.e.,}$$

$$\mathcal{B}_{\rm C/N}(D_{\rm GRB/GW}) = \mathcal{B}_{\rm S/N}(D_{\rm GRB/GW})$$

and

$$\frac{P(D_{\rm GRB/GW}|\mathcal{H}^{\rm C})}{P(D_{\rm GRB/GW}|\mathcal{H}^{\rm S}_{\rm GRB/GW})} = \frac{P(D_{\rm GRB/GW}|\mathcal{H}^{\rm S}_{\rm GRB/GW})}{P(D_{\rm GRB/GW}|\mathcal{H}^{\rm S}_{\rm GRB/GW})} = 1 \text{ , i.e.,}$$

$$\mathcal{B}_{\rm C/S}(D_{\rm GRB/GW}) = \mathcal{B}_{\rm S/S}(D_{\rm GRB/GW}) = 1.$$

Thus, the Bayes' factor comparing the common-source hypothesis to the signal/noise hypothesis is:

$$\begin{aligned}\mathcal{B}_{\mathrm{C/SN}}(D_{\mathrm{GRB}}, D_{\mathrm{GW}}) &= \frac{P(D_{\mathrm{GW}}|\mathcal{H}^{\mathrm{S}}_{\mathrm{GW}})}{P(D_{\mathrm{GW}}|\mathcal{H}^{\mathrm{N}}_{\mathrm{GW}})}\mathcal{I}_{\theta}(D_{\mathrm{GRB}}, D_{\mathrm{GW}}) \\ &= \mathcal{B}_{\mathrm{S/N}}(D_{\mathrm{GW}})\mathcal{I}_{\theta}(D_{\mathrm{GRB}}, D_{\mathrm{GW}}).\end{aligned}$$

The first part of the right hand side, $\mathcal{B}_{\mathrm{S/N}}(D_{\mathrm{GW}})$, is proportional to $1/\mathrm{FAR}_{\mathrm{GW}}$ (the inverse FAR or IFAR) of the gravitational-wave signal because $P(D_{\mathrm{GW}}|\mathcal{H}^{\mathrm{S}})$ is the rate at which true gravitational-wave astrophysical events occur that are as loud (as determined by the analysis detection statistics) as observed data D_{GW} times some observing time Δt while $P(D_{\mathrm{GW}}|\mathcal{H}^{\mathrm{N}})$ is the rate at which noise events are detected as GW candidate events (as loud as the observed data D_{GW}) times the same observing time Δt.

The $\mathrm{IFAR}_{\mathrm{GW}}$ takes the particular form that its probability density function (PDF) and cumulative distribution function (CDF) take the particular forms:

$$\begin{aligned}P(\mathrm{IFAR}_{\mathrm{GW}}) &= \frac{k}{\mathrm{IFAR}^2_{\mathrm{GW}}} \\ P(\mathrm{IFAR}_{\mathrm{GW}} > \mathrm{IFAR}^*_{\mathrm{GW}}) &= \int_{\mathrm{IFAR}^*_{\mathrm{GW}}}^{\infty} \frac{k}{x^2} dx \\ &= -\frac{k}{x}\Big|_{\mathrm{IFAR}^*_{\mathrm{GW}}}^{\infty} = \frac{k}{\mathrm{IFAR}^*_{\mathrm{GW}}},\end{aligned}$$

for some constant k[3]. This $\mathrm{IFAR}_{\mathrm{GW}}$ PDF has the important property that it is invariant under multiplication by a real, non-negative random variable, $\mathcal{S}$,

[3]By definition, the expected number of triggers below $\mathrm{FAR}^*_{\mathrm{GW}}$ due to background is $\mathrm{FAR}^*_{\mathrm{GW}}$ $\times$ the foreground time analyzed. Thus, the expected number of triggers above $\mathrm{IFAR}^*_{\mathrm{GW}}$ due to background is $k/\mathrm{IFAR}^*_{\mathrm{GW}}$ where k is the foreground time analyzed.

whose expectation value, $\langle \mathcal{S} \rangle$, is 1:

$$\begin{aligned} P(\mathcal{R}) = P(\mathrm{IFAR_{GW}} \times \mathcal{S}) &= \int_{-\infty}^{\infty} P(\mathcal{S}) P(\mathrm{IFAR_{GW}}) \frac{1}{|\mathcal{S}|} d\mathcal{S} \\ &= \int_{-\infty}^{\infty} P(\mathcal{S}) \frac{k}{\mathrm{IFAR_{GW}^2}} \frac{1}{\mathcal{S}} d\mathcal{S} \\ &= \int_{-\infty}^{\infty} P(\mathcal{S}) \frac{k}{(\mathrm{IFAR_{GW}} \times \mathcal{S})^2} \mathcal{S} d\mathcal{S} \\ &= \frac{k}{\mathcal{R}^2} \int_{-\infty}^{\infty} \mathcal{S} P(\mathcal{S}) d\mathcal{S} = \frac{k}{\mathcal{R}^2}. \end{aligned}$$

This gives us the important result that if the expectation value of the overlap integrals, $\langle \mathcal{I}_\theta \rangle$, is 1, the Bayes' factor itself can be thought of as an inverse FAR for the coincidence:

$$\begin{aligned} \mathcal{B}_{\mathrm{C/SN}}(D_{\mathrm{GRB}}, D_{\mathrm{GW}}) &\propto \mathrm{IFAR_{GW}} \mathcal{I}_\theta(D_{\mathrm{GRB}}, D_{\mathrm{GW}}) \\ &\propto \mathrm{IFAR_{coinc}}. \end{aligned}$$

Thus, `RAVEN` can report a FAR for each coincidence it finds, which can be interpreted as the rate at which noise in the GW detectors is coincident with a real GRB:

$$\mathrm{FAR_{coinc}} = \frac{\mathrm{FAR_{GW}}}{\mathcal{I}_\theta(D_{\mathrm{GRB}}, D_{\mathrm{GW}})}.$$

Intuitively, this agrees with common sense. The coincidence becomes more significant (i.e., the value of the coincidence FAR decreases) if parameters describing the astrophysical event from the GRB and GW data streams independently agree (i.e., the overlap integral is large). The following subsections detail exactly how the overlap integral is computed and double-check the condition that its expectation value is 1.

Temporal Coincidence False Alarm Rates

The `RAVEN` temporal coincidence inverse false alarm rate takes the form:

$$\mathrm{IFAR_{coinc}} = \mathrm{IFAR_{GW}} \mathcal{I}_t(D_{\mathrm{GRB}}, D_{\mathrm{GW}})$$

which depends on the temporal posterior overlap integral:

$$\begin{aligned}\mathcal{I}_t &= \int_{\Theta^{\mathrm{S}}} \frac{P(t_{\mathrm{GW}}|D_{\mathrm{GRB}},\mathcal{H}^{\mathrm{C}})P(t_{\mathrm{GW}}|D_{\mathrm{GW}},\mathcal{H}^{\mathrm{C}})}{P(t_{\mathrm{GW}}|\mathcal{H}^{\mathrm{C}})}dt_{\mathrm{GW}} \\ &= \int_{\Theta^{\mathrm{S}}} \frac{P(t_{\mathrm{GW}}|D_{\mathrm{GRB}},\mathcal{H}^{\mathrm{S}}_{\mathrm{GRB}})P(t_{\mathrm{GW}}|D_{\mathrm{GW}},\mathcal{H}^{\mathrm{S}}_{\mathrm{GW}})}{P(t_{\mathrm{GW}}|\mathcal{H}^{\mathrm{S}}_{\mathrm{GRB/GW}})}dt_{\mathrm{GW}}.\end{aligned}$$

The temporal posterior overlap integral can be simplified because all gravitational-wave candidate events entering GraceDb have an observed event time, $\hat{t}_{\mathrm{GW}}$, which gives:

$$P(t_{\mathrm{GW}}|D_{\mathrm{GW}},\mathcal{H}^{\mathrm{S}}_{\mathrm{GW}}) = \delta(t_{\mathrm{GW}} - \hat{t}_{\mathrm{GW}})$$

and

$$\mathcal{I}_t = \frac{P(t_{\mathrm{GW}} = \hat{t}_{\mathrm{GW}}|D_{\mathrm{GRB}},\mathcal{H}^{\mathrm{S}}_{\mathrm{GRB}})}{P(t_{\mathrm{GW}} = \hat{t}_{\mathrm{GW}}|\mathcal{H}^{\mathrm{S}}_{\mathrm{GRB/GW}})}.$$

However, the time of the GRB observation, $\hat{t}_{\mathrm{GRB}}$, does not directly infer $\hat{t}_{\mathrm{GW}}$, the time of the gravitational-wave candidate event. Instead, the two observation times are related by an astrophysical model which gives:

$$\Delta t = t_{\mathrm{GRB}} - t_{\mathrm{GW}}$$

and

$$P(t_{\mathrm{GW}}|D_{\mathrm{GRB}},\mathcal{H}^{\mathrm{S}}_{\mathrm{GRB}}) = \int P(t_{\mathrm{GW}} + \Delta t|D_{\mathrm{GRB}},\mathcal{H}^{\mathrm{S}}_{\mathrm{GRB}})P(\Delta t)d\Delta t.$$

One of the built-in assumptions for `RAVEN` is that the GRB will come in some time within $[\Delta t^{\mathrm{min}}, \Delta t^{\mathrm{max}}]$ s ($[-1, +5]$ s for modeled compact binary coalescences and $[-60, +600]$ s for unmodeled burst transients) of the gravitational-wave event time. Thus, $P(\Delta t)$ is the uniform distribution:

$$P(\Delta t) = U^{\Delta t^{\mathrm{max}}}_{\Delta t^{\mathrm{min}}}(\Delta t).$$

Because the PDF for the GRB event time is also a delta function, we have:

$$P(t_{\rm GW}|D_{\rm GRB},\mathcal{H}^{\rm S}_{\rm GRB}) = \int \delta(\Delta t + t_{\rm GW} - \hat{t}_{\rm GRB}) U^{\Delta t^{\rm max}}_{\Delta t^{\rm min}}(\Delta t) d\Delta t$$
$$= U^{\Delta t^{\rm max}}_{\Delta t^{\rm min}}(\hat{t}_{\rm GRB} - t_{\rm GW}).$$

This gives us:

$$\mathcal{I}_t = \frac{U^{\Delta t^{\rm max}}_{\Delta t^{\rm min}}(\hat{t}_{\rm GRB} - \hat{t}_{\rm GW})}{P(t_{\rm GW} = \hat{t}_{\rm GW}|\mathcal{H}^{\rm S}_{\rm GRB/GW})},$$

where the denominator is the uniform distribution:

$$P(t_{\rm GW}|\mathcal{H}^{\rm S}_{\rm GRB}) = U^{\Delta t^{\rm GRB}}_{0}(t_{\rm GW}),$$

where $\Delta t^{\rm GRB}$ is the time between independent GRB discoveries by *Swift* and *Fermi*[4].

Thus, the temporal posterior overlap integral is:

$$\begin{aligned}\mathcal{I}_t &= \frac{U^{\Delta t^{\rm max}}_{\Delta t^{\rm min}}(\hat{t}_{\rm GRB} - \hat{t}_{\rm GW})}{U^{\Delta t^{\rm GRB}}_{0}(t_{\rm GW})} \\ &= \frac{\Delta t^{\rm GRB}}{\Delta t^{\rm max} - \Delta t^{\rm min}} = \frac{\Delta t^{\rm GRB}}{\Delta t^{\rm search}} \\ &= \frac{1}{{\rm R}^{\rm GRB}\Delta t^{\rm search}}.\end{aligned}$$

If the expectation value of the temporal coincidence statistic is 1, i.e., $\langle\mathcal{S}\rangle = \langle 1/({\rm R}^{\rm GRB}\Delta t^{\rm search})\rangle = 1$, we can safely multiply $\mathcal{I}_t$ with ${\rm IFAR}_{\rm GW}$ and interpret the product as the temporal coincidence IFAR. And indeed it is! There are only two values of $\mathcal{S}$ (0 when there is no coincidence and $1/({\rm R}^{\rm GRB}\Delta t^{\rm search})$ when there is, with a coincidence ocurring with probability ${\rm R}^{\rm GRB}\Delta t^{\rm search}$), giving us:

$$\langle\mathcal{S}\rangle = 0 \cdot (1 - {\rm R}^{\rm GRB}\Delta t^{\rm search}) + \frac{1}{{\rm R}^{\rm GRB}\Delta t^{\rm search}} \cdot {\rm R}^{\rm GRB}\Delta t^{\rm search} = 1.$$

[4]In practice, $\Delta t^{\rm GRB}$ is computed as $1/{\rm R}_{\rm GRB}$, where ${\rm R}_{\rm GRB} = 0.807/(60 \times 60 \times 24$ s) is the empirical combined rate of independent GRB discoveries by *Swift* and *Fermi*.

Thus, the temporal coincidence FAR is:

$$\mathrm{FAR}_{\mathrm{coinc}} = \mathrm{FAR}_{\mathrm{GW}} \mathrm{R}^{\mathrm{GRB}} \Delta t^{\mathrm{search}}.$$

If the O3 `RAVEN` pipeline had been available and running during O2, a coincidence would have been found between the single-detector modeled compact binary coalescence candidate event G298048 (which later became GW170817) and GRB 170817A. The search window would have been 6 seconds. Thus, the reported temporal coincidence FAR would have been:

$$\begin{aligned}\mathrm{FAR}_{\mathrm{coinc}} &= 3.478 \times 10^{-12}\ \mathrm{Hz} \times \frac{0.807}{60 \times 60 \times 24\ \mathrm{s}} \times 6\ \mathrm{s} \\ &\approx 1.95 \times 10^{-16}\ \mathrm{Hz} = 1\ \mathrm{per}\ 1.63 \times 10^{8}\ \mathrm{yr}.\end{aligned}$$

Spatio-Temporal Coincidence False Alarm Rates

When sky localization probability maps (skymaps) are available from both GW and GRB data sets, `RAVEN` can also compute the spatio-temporal coincidence FAR. We start with the inverse false alarm rate which takes the form:

$$\begin{aligned}\mathrm{IFAR}_{\mathrm{coinc}} &= \mathrm{IFAR}_{\mathrm{GW}} \mathcal{I}_{t,\mathbf{\Omega}}(D_{\mathrm{GRB}}, D_{\mathrm{GW}}) \\ &= \mathrm{IFAR}_{\mathrm{GW}} \mathcal{I}_{t}(D_{\mathrm{GRB}}, D_{\mathrm{GW}}) \mathcal{I}_{\mathbf{\Omega}}(D_{\mathrm{GRB}}, D_{\mathrm{GW}}),\end{aligned}$$

where the posterior overlap integral cleanly factorizes into a temporal part and a spatial part. The temporal posterior overlap integral was calculated in Subsection 8.1 and the spatial posterior overlap integral is:

$$\begin{aligned}\mathcal{I}_{\mathbf{\Omega}} &= \int_{\Theta^{\mathrm{S}}} \frac{P(\mathbf{\Omega}|D_{\mathrm{GRB}}, \mathcal{H}^{\mathrm{C}}) P(\mathbf{\Omega}|D_{\mathrm{GW}}, \mathcal{H}^{\mathrm{C}})}{P(\mathbf{\Omega}|\mathcal{H}^{\mathrm{C}})} d\mathbf{\Omega} \\ &= \int_{\Theta^{\mathrm{S}}} \frac{P(\mathbf{\Omega}|D_{\mathrm{GRB}}, \mathcal{H}^{\mathrm{S}}_{\mathrm{GRB}}) P(\mathbf{\Omega}|D_{\mathrm{GW}}, \mathcal{H}^{\mathrm{S}}_{\mathrm{GW}})}{P(\mathbf{\Omega}|\mathcal{H}^{\mathrm{S}}_{\mathrm{GRB/GW}})} d\mathbf{\Omega}.\end{aligned}$$

We assume for the sake of simplicity a uniform all-sky prior, although in reality, this is not strictly true. For instance, instruments aboard *Fermi*

do not take data while transiting the South Atlantic Anomaly (SAA) and the advanced ground-based interferometric GW detectors are sensitive to direction (Section 3.5). Then, the spatial overlap integral takes the continuous and discrete forms:

$$\begin{aligned}\mathcal{I}_{\mathbf{\Omega}} &= 4\pi \int_{\Theta^{\mathrm{S}}} P(\mathbf{\Omega}|D_{\mathrm{GRB}}, \mathcal{H}^{\mathrm{S}}_{\mathrm{GRB}}) P(\mathbf{\Omega}|D_{\mathrm{GW}}, \mathcal{H}^{\mathrm{S}}_{\mathrm{GW}}) d\mathbf{\Omega} \\ &= \mathrm{N_{pix}} \sum_{i=1}^{\mathrm{N_{pix}}} \mathrm{skymap_{GRB}}[i] \times \mathrm{skymap_{GW}}[i],\end{aligned}$$

where the GRB and GW skymaps are assumed to have the same pixel resolution[5].

Now, the value of $\mathcal{I}_{\mathbf{\Omega}}$ can range from 0 to infinitely high depending on how well the GRB and GW spatial posteriors overlap and are localized. It is not obvious a priori that the expectation value of $\mathcal{I}_{\mathbf{\Omega}}$ will be 1, and until this is checked, we cannot report the spatio-temporal coincidence FAR. Thus, for each low-latency GW search pipeline (`GstLAL`, `PyCBC Live`, `MBTAOnline`, `cWB`, and `oLIB`), 100 low-latency GW skymaps produced from its candidate events were combined with 100 *Fermi* Gamma-ray Burst Monitor (GBM) skymaps to produce 10,000 overlap integrals (Table 8.1).

As can be seen, all pipelines are within $\sim 1\sigma$ of a mean value approximately equal to 1, except for `GstLAL` which is $\sim 3.5\sigma$ away. However, even this systematic shift in the spatial overlap integrals using `GstLAL` GW candidate event skymaps is contained at $\sim 8.5\%$.

Thus, because $\langle \mathcal{I}_{\mathbf{\Omega}} \rangle \approx 1$, the spatio-temporal coincidence FAR is:

$$\mathrm{FAR_{coinc}} = \frac{\mathrm{FAR_{GW}} \mathrm{R}^{\mathrm{GRB}} \Delta t^{\mathrm{search}}}{\mathcal{I}_{\mathbf{\Omega}}}.$$

[5] $\mathrm{N_{pix}}$ is the total number of pixels in a skymap. When the pixel resolutions differ, we match the GRB skymap resolution to the GW skymap and normalize its probabilities:

$$\mathcal{I}_{\mathbf{\Omega}} = \mathrm{N_{pix}} \frac{\sum_{i=1}^{\mathrm{N_{pix}}} \mathrm{skymap_{GRB}}[i] \times \mathrm{skymap_{GW}}[i]}{\sum_{i=1}^{\mathrm{N_{pix}}} \mathrm{skymap_{GRB}}[i]}.$$

Pipeline	$\overline{\mathcal{I}_{\mathbf{\Omega}}}$	$\sigma(\mathcal{I}_{\mathbf{\Omega}})/\sqrt{10^4}$
GstLAL	1.085	0.024
PyCBC Live	1.017	0.033
MBTAOnline	0.995	0.025
cWB	1.019	0.027
oLIB	0.949	0.049

Table 8.1: Summary of 50,000 spatial overlap integrals, $\mathcal{I}_{\mathbf{\Omega}}$, reporting the mean and standard deviation of the mean for 100 low-latency GW skymaps per pipeline combined with 100 *Fermi*/GBM GRB skymaps.

To continue our example of the single-detector GW candidate event G298048 coincidence with GRB 170817A, we compute the spatial overlap integral. Using the skymap from *Fermi*/GBM[6] and the low-latency skymap produced by BAYESTAR with only LIGO/Hanford data, we compute:

$$\begin{aligned}\mathrm{FAR}_{\mathrm{coinc}} &= 3.478 \times 10^{-12}\ \mathrm{Hz} \times \frac{0.807}{60 \times 60 \times 24\ \mathrm{s}} \times 6\ \mathrm{s} \times \frac{1}{2.243} \\ &\approx 8.69 \times 10^{-17}\ \mathrm{Hz} = 1\ \mathrm{per}\ 3.66 \times 10^{8}\ \mathrm{yr}.\end{aligned}$$

Joint GW-GRB Sky Localization Probability Maps

We calculate the spatial overlap integral, $\mathcal{I}_{\mathbf{\Omega}}$, in Subsection 8.1 using two skymaps: one from *Fermi*/GBM for the GRB localization and one from Advanced LIGO and Advanced Virgo for the GW candidate event localization. For O3, these same two skymaps are used to provide our astronomer partners with a combined skymap.

As an example, in Figure 8.1, the low-latency localization pipeline BAYESTAR used data from both Advanced LIGO detectors to localize GW170817[7]. Then, *Fermi*/GBM provided localization for GRB 170817A. In this case, $\mathcal{I}_{\mathbf{\Omega}} = 10.39$, which is greater than one, but not significantly large due to uncertainties in

[6] https://gammaray.nsstc.nasa.gov/gbm/science/grbs/grb170817a/gbuts_healpix_systematic.fit

[7] https://dcc.ligo.org/public/0146/G1701985/001/BAYESTAR_no_virgo.fits.gz

both skymaps. The normalized product of these two skymaps reveals that although the GW170817 `BAYESTAR` skymap is bimodal with two long, thin islands of probability, the overlap involves only the island from the Northern antenna pattern.

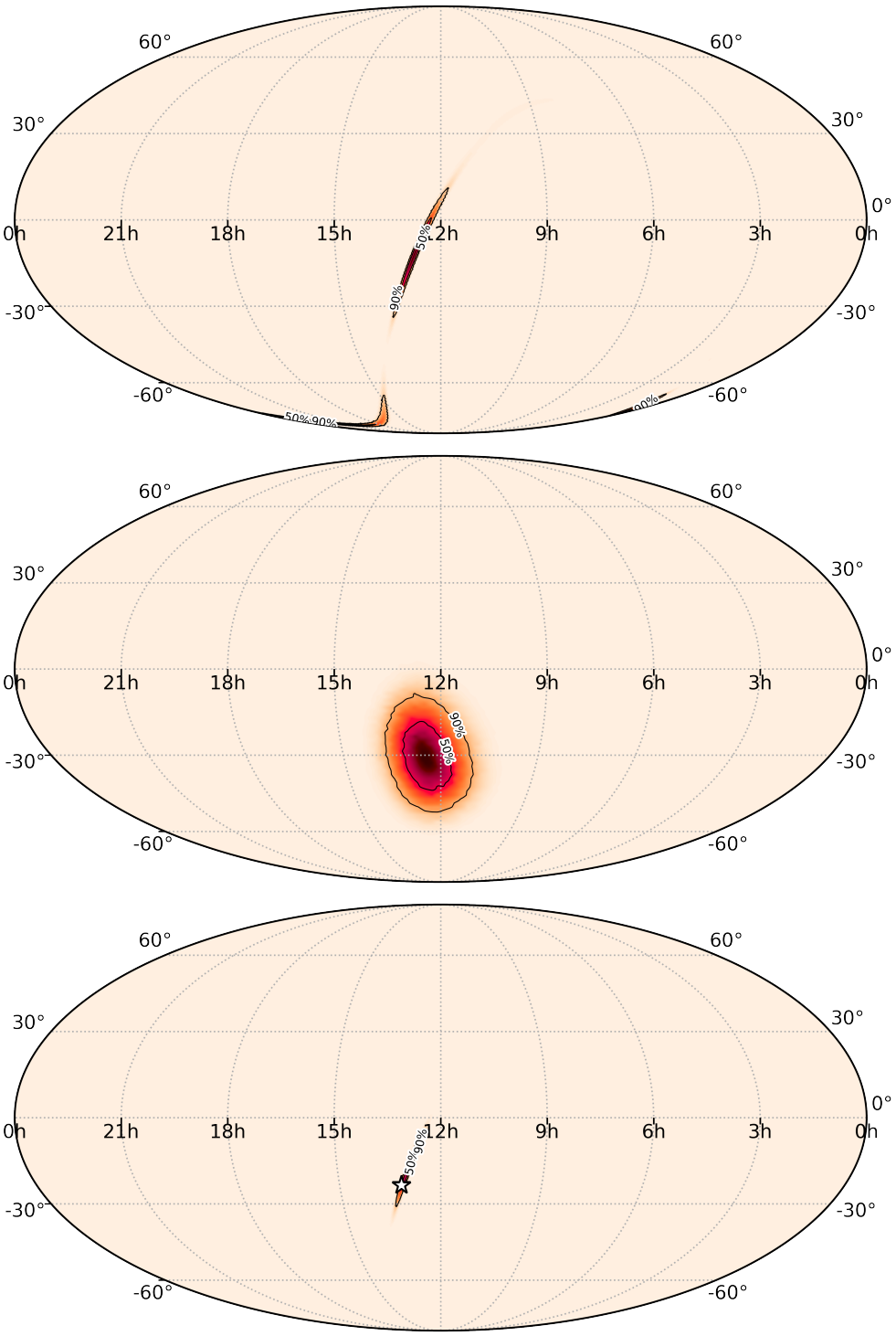

Figure 8.1: From top to bottom, skymaps in ICRS coordinates (Mollweide projection) with 90% and 50% credible regions for GW170817 (computed by `BAYESTAR` using Advanced LIGO data only), GRB 170817A from *Fermi*/GBM, and their normalized product. The location of the apparent host galaxy NGC 4993 is marked with a star in the joint GW-GRB skymap.

8.2 P_astro: The Probability of Astrophysical Origin

Currently, there is an effort to provide our observing partners with a new data product from the `P_astro` pipeline, which computes the probability that a CBC GW candidate event is of astrophysical origin, accounting for both foreground GW trigger rate distribution and background trigger rate distribution. It uses a multicomponent/extended FGMC (Farr-Gair-Mandel-Cutler) method (Kapadia et al., 2018), explained below. Specifically, the pipeline looks at four astrophysical regions, α, of a low-latency search pipeline's template bank parameter space: regions of binary neutron stars (BNS), neutron star-black holes (NS-BH), binary black holes (BBH), and mass-gap binaries (binaries involving at least one compact object of masses between $3M_{\odot}$ and $5M_{\odot}$).

The original FGMC method applies Poisson counting statistics to construct a two-component posterior on expected trigger counts from astrophysical (Λ_1) and terrestrial (Λ_0) sources during a set observing time (Farr et al., 2015). There is a built-in assumption that the search pipeline's ranking statistic/SNR threshold for triggering is set low such that the number of background triggers vastly exceeds the number of astrophysical triggers, and the expected trigger counts, $\Lambda_{0,1}$, for each type of trigger follows counting statistics:

$$P(k|\Lambda_{0,1}) \propto \Lambda_{0,1}^{k} e^{-\Lambda_{0,1}}.$$

Then, the two-component posterior can be written as:

$$P(\Lambda_0, \Lambda_1|\{x_1, x_2, \ldots, x_N\}) \propto P(\Lambda_0, \Lambda_1) \prod_{j=1}^{N} (\Lambda_0 b(x_j) + \Lambda_1 f(x_j)) e^{-\Lambda_0 - \Lambda_1},$$

where N is the observed number of candidate events above threshold, x_i are the ranking statistic/SNR of the candidate events, $P(\Lambda_0, \Lambda_1)$ is the prior on the expected counts, and $b(x_i)$ and $f(x_i)$ are the background and foreground

probability density functions (i.e., models) evaluated at the observed x_i (i.e., $b(x_i) = P(x_i|\text{noise})$ and $f(x_i) = P(x_i|\text{signal})$).

In the multicomponent/extended FGMC method, the foreground triggers are split into their α categories such that there are multiple, source-specific foreground trigger distributions, $\vec{f}(x) = f_\alpha(x)$, where x is generalized to contain more information about the trigger's properties than just the ranking statistic/SNR (now denoted as L). The corresponding astrophysical origin expected trigger count is also split into source-specific categories, $\vec{\Lambda}_1 = \Lambda_\alpha$. Then, the multicomponent posterior can be written as:

$$P(\Lambda_0, \vec{\Lambda}_1|\{x_1, x_2, \ldots, x_N\}) \propto P(\Lambda_0, \vec{\Lambda}_1) \prod_{j=1}^{N} (\Lambda_0 b(x_j) + \vec{\Lambda}_1 \cdot \vec{f}(x_j)) e^{-\Lambda_0 - \vec{\Lambda}_1 \cdot \vec{u}},$$

where $\vec{u}$ is the corresponding unit vector for each source-specific class we are interested in (i.e., for 4 astrophysical categories of interest, the multiplicative factor at the end must be $e^{-\Lambda_0 - \Lambda_1 - \ldots - \Lambda_4}$).

In practice, for the `GstLAL` low-latency search pipeline where `P_astro` has been implemented, the foreground trigger distributions, $\vec{f}_\alpha(x)$, can be approximated using conditional probability and by dividing the search pipeline's template bank parameter space into multiple bins (denoted as m):

$$\vec{f}(x) = f_\alpha(x) = P(L, m|\alpha) = P(L|m, \alpha)P(m|\alpha) \approx P(L|m, \text{signal})P(m|\alpha),$$

where L is `GstLAL`'s ranking statistic (the likelihood ratio), m is the template bin number, $P(m|\alpha)$ are the template weights (i.e., $W_\alpha(m)$), and $P(L|m, \text{signal})$ are the bin-dependent foreground trigger probabilities. Likewise, the background trigger distribution also has a bin-dependent form:

$$b(x) = P(L, m|\text{noise}) = P(L|m, \text{noise})P(m|\text{noise}),$$

where $P(m|\text{noise})$ are the noise template weights (i.e., $W_0(m)$).

This allows us to re-write the multicomponent posterior more compactly, using source-specific Bayes factors for a trigger that registers with x's ranking statistic value L:

$$\begin{aligned}\vec{K}_1(x) &= \frac{\vec{f}(x)}{b(x)} = \frac{P(L|m,\text{signal})}{P(L|m,\text{noise})}\frac{\vec{W}_1(m)}{W_0(m)},\\ P(\Lambda_0,\vec{\Lambda}_1)|\vec{x}) &= P(\Lambda_0,\vec{\Lambda}_1|\{x_1,x_2,\text{ and}\ldots,x_N\})\\ &\propto P(\Lambda_0,\vec{\Lambda}_1)\prod_{j=1}^{N}(\Lambda_0+\vec{\Lambda}_1\cdot\vec{K}_1(x_j))e^{-\Lambda_0-\vec{\Lambda}_1\cdot\vec{u}}.\end{aligned}$$

The conditional probability that an event with properties x comes from the α^{th} astrophysical source category is given by:

$$P(\Lambda_\alpha,x|\Lambda_0,\vec{\Lambda}_1) = \frac{\Lambda_\alpha f_\alpha(x)}{\Lambda_0 b(x)+\vec{\Lambda}_1\cdot\vec{f}_1(x)} = \frac{\Lambda_\alpha K_\alpha(x)}{\Lambda_0+\vec{\Lambda}_1\cdot\vec{K}_1(x)}.$$

Then, marginalizing over the posterior for the expected counts gives us:

$$\begin{aligned}P(\Lambda_\alpha,x|\vec{x}) &= \int_0^\infty P(\Lambda_\alpha,x|\Lambda_0,\vec{\Lambda}_1)P(\Lambda_0,\vec{\Lambda}_1|\vec{x})\ d\Lambda_0\ d\vec{\Lambda}_1\\ &= \int_0^\infty \frac{\Lambda_\alpha f_\alpha(x)}{\Lambda_0 b(x)+\vec{\Lambda}_1\cdot\vec{f}_1(x)}P(\Lambda_0,\vec{\Lambda}_1|\vec{x})\ d\Lambda_0\ d\vec{\Lambda}_1\\ &= \int_0^\infty \frac{\Lambda_\alpha K_\alpha(x)}{\Lambda_0+\vec{\Lambda}_1\cdot\vec{K}_1(x)}P(\Lambda_0,\vec{\Lambda}_1|\vec{x})\ d\Lambda_0\ d\vec{\Lambda}_1.\end{aligned}$$

With low-latencies in mind, the sub-second `P_astro` pipeline in fact computes the astrophysical probability that the $N{+}1^{\text{th}}$ candidate event (i.e., the new candidate event) is in the α^{th} astrophysical source category by working with mean values of the background and source-specific astrophysical Poisson expected counts, $\langle\Lambda_0\rangle_N$ and $\langle\vec{\Lambda}_1\rangle_N$, which are pre-computed on a weekly cadence during maintenance[8]:

$$\begin{aligned}\langle\Lambda_\alpha\rangle &= \int_0^\infty \Lambda_\alpha P(\Lambda_0,\vec{\Lambda}_1|\vec{x})\ d\Lambda_0\ d\vec{\Lambda}_1,\ \text{and}\\ P(\Lambda_\alpha,x_{N+1}|\vec{x}_{N+1}) &= \frac{\langle\Lambda_\alpha\rangle_N K_\alpha(x_{N+1})}{\langle\Lambda_0\rangle_N+\langle\vec{\Lambda}_1\rangle_N\cdot\vec{K}_1(x_{N+1})}.\end{aligned}$$

[8]The computation of the mean values themselves during maintenance is on the order of $\sim$minutes.

To continuously update the template weights, injection campaigns are conducted on a weekly basis to see which parts of the template banks are triggered, i.e., activated. Lastly, as of yet, the probabilities produced by the `P_astro` pipeline are not used for candidate event vetting. They will, however, be included in the LIGO/Virgo Circulars if available.

8.3 Public Alerts

For Advanced LIGO and Virgo's upcoming third observing run, O3, we enter the era of public alerts, where LIGO/Virgo Preliminary Notices will be sent fully autonomously within ∼1 to 10 minutes of a promising GW trigger entering GraceDb. Much of the low-latency follow-up processes for annotating and orchestrating LVAlerts will be triggered under `GWCelery`[9], an umbrella Python-based package based on the asynchronous task queue, `Celery`. The most up-to-date information regarding alert content, including instructions for signing up to receive these alerts, can be found at the *LIGO/Virgo Public Alerts User Guide*: https://emfollow.docs.ligo.org/userguide/.

During the few minutes' latency for sending the Preliminary Notice, several automated processes will occur for incoming GW triggers. Most importantly, there is a new notion of a "Superevent", which unifies a group of GW triggers from multiple low-latency search pipelines that correspond to the same physical event. Each Superevent has a so-called preferred_event (whose FAR and trigger properties are reported in the outgoing Notices and Circulars) and a GW_events list (which includes all the other related GW triggers). The Superevents follow a naming convention, Syymmdd{abc}, where S stands for Superevent, yymmdd is the UTC date, and letters at the end increment as a, b, . . . , aa, . . . , to allow for the possibility of many time-separated GW triggers

[9] https://gwcelery.readthedocs.io/

being recovered on a given day.

The Superevent's preferred_event is selected to preference GW triggers recovered with data from multiple detectors versus a single detector for improved localization. For compact binary coalescence events, a CBC low-latency search trigger is preferred over a Burst low-latency search trigger for improved waveform reconstruction and parameter estimation. If at this point, there still hasn't been a down-selection to one GW trigger, the Superevent algorithm selects for its preferred_event the GW trigger with the lowest reported FAR for Burst triggers, but highest SNR for CBC triggers. There is also a preference for CBC triggers over Burst, and multi-interferometer triggers over single-detector triggers.

Once the preferred_event has been set, we check its FAR to see if it falls below the threshold for reporting ($\sim$1/2 months for CBC Superevents using a trials factor of 5 and $\sim$1/yr for Burst Superevents using a trials factor of 4)[10]. In this scenario, the first LIGO/Virgo Preliminary Notice is sent (with reference to a skymap if available), with the possibility of a second Preliminary Notice if a skymap becomes available before the Superevent has been vetted for its data quality. All Superevents that have been released to the public will have GraceDb pages that are viewable by persons outside the LIGO Scientific Collaboration and Virgo Collaboration.

The turnaround for sending the LIGO/Virgo Initial Notice and Circular is within 24 hours, (with the goal of $\sim$30 minutes for BNS and NS-BH Superevents). During this time, human vetting procedures similar to those that occurred during O1 and O2 will be performed, and all Initial Notices and Circulars will be distributed with an update for the sky localization.

[10]The trials factors correspond to the number of pipelines for CBC and Burst low-latency searches. The CBC pipelines are `GstLAL`, `PyCBC Live`, `MBTAOnline`, `SPIIR-HighMass`, and `SPIIR-LowMass`. The Burst searches are `cWB-AllSky`, `cWB-BBH`, `cWB-IMBH` and `oLIB-AllSky`.

In the case of CBC Superevents, we will also release `EM-Bright` source classification and `P_astro` data products through the Initial Notice and Circular, although quantitative estimates of the masses and spins, GW strain data, and the waveform regressed from the data will be kept inside the Collaborations.

For publications related to LIGO/Virgo Superevents that become confirmed events, the LIGO/Virgo Initial Circular should be cited as the first formal publication of the candidate event. If data quality inspections determine the Superevent to be a noise event, a LIGO/Virgo Retraction Notice will be sent, indicating that the Superevent is no longer a GW candidate event.

Chapter 9

Conclusions and Outlook

The science of gravitational-wave (GW) astronomy is maximized when we have joint detections by instruments of traditional astronomy. A joint detection can serve to confirm the astrophysical origin of the signal, to determine the host galaxy (and therefore distance to the event), to discern viable models concerning the central engine and event environment, and much more. Thus, the majority of my time as a graduate student was devoted to enabling electromagnetic/neutrino follow-up of Advanced LIGO and Virgo's GW candidate events.

A collaboration-wide goal for the first observing run (O1) was to enable joint detections in the event that we saw something interesting—a possible GW signal. Thus, for O1 I created the first GW candidate event annotator during the Advanced Detector era, `approval_processor`. The software that I wrote served to (1) select the candidate events for follow-up and (2) send the alerts out to the traditional astronomy community. Looking back, I remember the excitement and almost-palpable tension in the air when we had our first viable GW trigger (the one we would later name GW150914, the first ever observed binary black hole merger). The rest (to be honest) is a blur; we were all so busy with the prospect of our first discovery.

In the months leading up to the second observing run (O2), we determined within the LIGO/Virgo follow-up group that `approval_processor` would require an upgrade to deal with increased rates of GW triggers expected during O2. We needed to design the software to avoid race conditions and backlogging

in how it processed incoming streams of information from various pipelines (e.g., data quality products, sky localization probability maps, labels, etc.). Therefore, I worked with Reed Essick to create the second GW candidate event annotator during the Advanced Detector era, `approval_processorMP`. Our responsibilities were divided so that he created the programming objects for the annotator's multi-processing infrastructure, and I created the canvas that utilized these objects to make logical decisions in selecting candidate events and sending alerts for follow-up.

As a result of these efforts, we successfully sent alerts out to the wider astronomy community during both O1 and O2. We even had a few confirmed GW detections along the way (11 of them to date!), and at least one highly-confident joint detection, GW170817, the first ever observed binary neutron star merger. The other less-confident (possible) joint detection occurred with a *Fermi*/GBM weak transient at the time of GW150914 (Connaughton et al., 2016).

To summarize, when I first started my graduate research in GW astronomy, we had not yet detected any GW events. It had still been an open question whether or not we would see anything during O1. Fast-forward a couple of years and the current landscape is very different. The question has evolved from, "Will we see anything?" to now, "Will we have enough follow-up advocates on duty? And what will we see? What counterparts will be found? What will joint detections tell us about the event?"

Advanced LIGO and Virgo's third observing run (O3) has already officially started as of April 1, 2019. KAGRA, the cryogenic underground GW detector in Japan, will also join for O3. In less than 4 years since the detection of GW150914 (which admittedly had a more improvised vetting and EM/neu-

trino follow-up alert process), we have streamlined the follow-up procedure to best facilitate our observing partners and increase our science returns.

There will be an uptick in the number of alerts sent during O3 for two reasons. One, the sensitivities of our detectors improve with each observing run (Table 9.1) and two, we enter the era of public alerts.

We expect numerous compact binary coalescence (CBC) GW events, with BBH candidates occurring ∼1 per week and BNS candidates occurring up to ∼1 per month (for a total of 1 to 10 for the totality of the observing run). The NS-BH coalescence event rate remains uncertain (Pankow, 2018). For each CBC candidate event, low-latency sky localization probability maps that are both rapid and accurate are generated, source classification and astrophysical origin probabilities for four source categories (BNS, NS-BH, BBH, and mass-gap binaries) are provided, and human-vetted alerts are sent/composed within hours of a promising candidate event.

Detector	**BNS Range (Mpc)**
Advanced LIGO	120 to 170
Advanced Virgo	65 to 85
KAGRA	8 to 25

Table 9.1: Expected detector sensitivities to BNS coalescences during O3.

For Burst candidate events, we let our imagination wander. What unexpected GW sources await our detection? What does the Universe have in store for us? Perhaps cosmic strings exist and are intersecting, emitting bursts of GW radiation. Even an "expected" GW source such as a Galactic supernova or magnetar starquake will be a boon for new scientific discovery and inquiry.

If anything, history has shown unforeseen fundamental discoveries accompany each new window of observation. Radio astronomy, for instance, led to the discovery of the cosmic microwave background (the earliest electromagnetic

relic of the Big Bang) and also quasi-stellar objects (i.e., quasars—accretion disks surrounding supermassive black holes at cosmological distances). Using Type Ia supernovae as standard candles, we also learned to our surprise that the Universe is expanding and accelerating, powered by dark energy, the dominant energy/mass component of the Universe... Thus, we have much to look forward to with the relatively new fields of GW and multi-messenger astronomy.

Appendix A

Appendix A: LIGO/Virgo Notices for GW150914

The following are the machine-readable LIGO/Virgo Notices (i.e., VOEvents) sent to GCN for the gravitational-wave candidate event G184098, later known as GW150914, the first ever observed binary black hole merger (Abbott et al., 2016b). VOEvent information is repackaged by GCN before being sent to our observing partners. The skymap sent with the LIGO/Virgo Update Notice was computed with the `LIB` parameter estimation algorithm.

```
<?xml version="1.0" ?>
<voe:VOEvent xmlns:xsi="http://www.w3.org/2001/XMLSchema-instance"
xmlns:voe="http://www.ivoa.net/xml/VOEvent/v2.0"
xsi:schemaLocation="http://www.ivoa.net/xml/VOEvent/v2.0 http://www.ivoa.net/xml/VOEvent/VOEvent-v2.0.xsd"
 version="2.0" role="observation" ivorn="ivo://gwnet/gcn_sender#G184098-7-Initial">
    <Who>
        <Date>2015-09-16T03:11:58</Date>
        <Author>
            <contactName>LIGO Scientific Collaboration and Virgo Collaboration</contactName>
        </Author>
    </Who>
    <What>
        <Param name="internal" dataType="string" value="0">
            <Description>Indicates that this event should be distributed to LSC/Virgo members only</Description>
        </Param>
        <Param name="Pkt_Ser_Num" dataType="string" value="7"/>
        <Param name="GraceID" dataType="string" value="G184098" ucd="meta.id">
            <Description>Identifier in GraceDB</Description>
        </Param>
        <Param name="AlertType" dataType="string" value="Initial" ucd="meta.version" unit="">
            <Description>VOEvent alert type</Description>
        </Param>
        <Param name="EventPage" dataType="string" value="https://gracedb.ligo.org/events/G184098" ucd="meta.ref.url">
            <Description>Web page for evolving status of this candidate event</Description>
        </Param>
```

```
26          <Param name="Instruments" dataType="string" value="H1,L1" ucd="meta.
                code">
27              <Description>List of instruments used in analysis to identify this event
                    </Description>
28          </Param>
29          <Param name="FAR" dataType="float" value="1.17786e-08" ucd="arith.rate;
                stat.falsealarm" unit="Hz">
30              <Description>False alarm rate for GW candidates with this strength or
                    greater</Description>
31          </Param>
32          <Param name="Group" dataType="string" value="Burst" ucd="meta.code"
                unit="">
33              <Description>Data analysis working group</Description>
34          </Param>
35          <Param name="Pipeline" dataType="string" value="CWB" ucd="meta.code"
                unit="">
36              <Description>Low-latency data analysis pipeline</Description>
37          </Param>
38          <Param name="Search" dataType="string" value="AllSky" ucd="meta.code"
                unit="">
39              <Description>Specific low-latency search</Description>
40          </Param>
41          <Param name="CentralFreq" dataType="float" value="123.828491" ucd="gw.
                frequency" unit="Hz">
42              <Description>Central frequency of GW burst signal</Description>
43          </Param>
44          <Param name="Duration" dataType="float" value="0.024773" ucd="time.
                duration" unit="s">
45              <Description>Measured duration of GW burst signal</Description>
46          </Param>
47          <Param name="Fluence" dataType="float" value="122.840988205" ucd="gw.
                fluence" unit="erg/cm^2">
48              <Description>Estimated fluence of GW burst signal</Description>
49          </Param>
50          <Group type="GW_SKYMAP" name="skyprobcc_cWB_complete-BurstAllSky">
51              <Param name="skymap_fits_shib" dataType="string" value="
                    https://gracedb.ligo.
                    org/events/G184098/files/skyprobcc_cWB_complete.fits" ucd="meta.
                    ref.url" unit="">
52                  <Description>Sky Map FITS Shibboleth protected</Description>
53              </Param>
54              <Param name="skymap_fits_x509" dataType="string" value="
                    https://gracedb.ligo.
                    org/api/events/G184098/files/skyprobcc_cWB_complete.fits" ucd="
                    meta.ref.url" unit="">
55                  <Description>Sky Map FITS X509 protected</Description>
56              </Param>
57              <Param name="skymap_fits_basic" dataType="string" value="
                    https://gracedb.ligo.
                    org/apibasic/events/G184098/files/skyprobcc_cWB_complete.fits"
                    ucd="meta.ref.url" unit="">
58                  <Description>Sky Map FITS basic auth protected</Description>
59              </Param>
60              <Param name="skymap_png_shib" dataType="string" value="
                    https://gracedb.ligo.
                    org/events/G184098/files/skyprobcc_cWB_complete.png" ucd="meta.
                    ref.url" unit="">
61                  <Description>Sky Map image Shibboleth protected</Description>
62              </Param>
63              <Param name="skymap_png_x509" dataType="string" value="
                    https://gracedb.ligo.
```

```
                org/api/events/G184098/files/skyprobcc_cWB_complete.png" ucd="
                meta.ref.url" unit="">
64              <Description>Sky Map image X509 protected</Description>
65          </Param>
66          <Param name="skymap_png_basic" dataType="string" value="
                https://gracedb.ligo.
                org/apibasic/events/G184098/files/skyprobcc_cWB_complete.png" ucd
                ="meta.ref.url" unit="">
67              <Description>Sky Map image basic auth protected</Description>
68          </Param>
69      </Group>
70  </What>
71  <WhereWhen>
72      <ObsDataLocation>
73          <ObservatoryLocation id="LIGO Virgo"/>
74          <ObservationLocation>
75              <AstroCoordSystem id="UTC-FK5-GEO"/>
76              <AstroCoords coord_system_id="UTC-FK5-GEO">
77                  <Time>
78                      <TimeInstant>
79                          <ISOTime>2015-09-14T09:50:45.391000</ISOTime>
80                      </TimeInstant>
81                  </Time>
82              </AstroCoords>
83          </ObservationLocation>
84      </ObsDataLocation>
85  </WhereWhen>
86  <How>
87      <Description>Candidate gravitational wave event identified by low-latency
            analysis</Description>
88      <Description>H1: LIGO Hanford 4 km gravitational wave detector</Description>
89      <Description>L1: LIGO Livingston 4 km gravitational wave detector<
            /Description>
90  </How>
91  <Citations>
92      <EventIVORN cite="supersedes">ivo://gwnet/gcn_sender#G184098-6-
            Preliminary</EventIVORN>
93      <EventIVORN cite="supersedes">ivo://gwnet/gcn_sender#G184098-5-Update
            </EventIVORN>
94      <EventIVORN cite="supersedes">ivo://gwnet/gcn_sender#G184098-4-
            Initial</EventIVORN>
95      <EventIVORN cite="supersedes">ivo://gwnet/gcn_sender#G184098-3-
            Preliminary</EventIVORN>
96      <EventIVORN cite="supersedes">ivo://gwnet/gcn_sender#G184098-2-
            Retraction</EventIVORN>
97      <EventIVORN cite="supersedes">ivo://gwnet/gcn_sender#G184098-1-
            Preliminary</EventIVORN>
98      <Description>Initial localization is now available</Description>
99  </Citations>
100 <Description>Report of a candidate gravitational wave event</Description>
101 </voe:VOEvent>
```

```
<?xml version="1.0" ?>
<voe:VOEvent xmlns:xsi="http://www.w3.org/2001/XMLSchema-instance"
xmlns:voe="http://www.ivoa.net/xml/VOEvent/v2.0"
xsi:schemaLocation="http://www.ivoa.net/xml/VOEvent/v2.0 http://www.ivoa.
    net/xml/VOEvent/VOEvent-v2.0.xsd"
 version="2.0" role="observation" ivorn="ivo://gwnet/gcn_sender#G184098-8-Update"
     >
    <Who>
        <Date>2015-09-16T03:14:30</Date>
        <Author>
            <contactName>LIGO Scientific Collaboration and Virgo Collaboration<
                /contactName>
        </Author>
    </Who>
    <What>
        <Param name="internal" dataType="string" value="0">
            <Description>Indicates that this event should be distributed to
                LSC/Virgo members only</Description>
        </Param>
        <Param name="Pkt_Ser_Num" dataType="string" value="8"/>
        <Param name="GraceID" dataType="string" value="G184098" ucd="meta.id">
            <Description>Identifier in GraceDB</Description>
        </Param>
        <Param name="AlertType" dataType="string" value="Update" ucd="meta.
            version" unit="">
            <Description>VOEvent alert type</Description>
        </Param>
        <Param name="EventPage" dataType="string" value="https://gracedb.ligo.
            org/events/G184098" ucd="meta.ref.url">
            <Description>Web page for evolving status of this candidate event<
                /Description>
        </Param>
        <Param name="Instruments" dataType="string" value="H1,L1" ucd="meta.
            code">
            <Description>List of instruments used in analysis to identify this event
                </Description>
        </Param>
        <Param name="FAR" dataType="float" value="1.17786e-08" ucd="arith.rate;
            stat.falsealarm" unit="Hz">
            <Description>False alarm rate for GW candidates with this strength or
                greater</Description>
        </Param>
        <Param name="Group" dataType="string" value="Burst" ucd="meta.code"
            unit="">
            <Description>Data analysis working group</Description>
        </Param>
        <Param name="Pipeline" dataType="string" value="CWB" ucd="meta.code"
            unit="">
            <Description>Low-latency data analysis pipeline</Description>
        </Param>
        <Param name="Search" dataType="string" value="AllSky" ucd="meta.code"
            unit="">
            <Description>Specific low-latency search</Description>
        </Param>
        <Param name="CentralFreq" dataType="float" value="123.828491" ucd="gw.
            frequency" unit="Hz">
            <Description>Central frequency of GW burst signal</Description>
        </Param>
        <Param name="Duration" dataType="float" value="0.024773" ucd="time.
            duration" unit="s">
            <Description>Measured duration of GW burst signal</Description>
```

```
46          </Param>
47          <Param name="Fluence" dataType="float" value="122.840988205" ucd="gw.
                fluence" unit="erg/cm^2">
48              <Description>Estimated fluence of GW burst signal</Description>
49          </Param>
50          <Group type="GW_SKYMAP" name="LIB_skymap-BurstAllSky">
51              <Param name="skymap_fits_shib" dataType="string" value="
                    https://gracedb.ligo.org/events/G184098/files/LIB_skymap.fits.gz"
                     ucd="meta.ref.url" unit="">
52                  <Description>Sky Map FITS Shibboleth protected</Description>
53              </Param>
54              <Param name="skymap_fits_x509" dataType="string" value="
                    https://gracedb.ligo.org/api/events/G184098/files/LIB_skymap.fits
                    .gz" ucd="meta.ref.url" unit="">
55                  <Description>Sky Map FITS X509 protected</Description>
56              </Param>
57              <Param name="skymap_fits_basic" dataType="string" value="
                    https://gracedb.ligo.org/apibasic/events/G184098/files/LIB_skymap
                    .fits.gz" ucd="meta.ref.url" unit="">
58                  <Description>Sky Map FITS basic auth protected</Description>
59              </Param>
60              <Param name="skymap_png_shib" dataType="string" value="
                    https://gracedb.ligo.org/events/G184098/files/LIB_skymap.png" ucd
                    ="meta.ref.url" unit="">
61                  <Description>Sky Map image Shibboleth protected</Description>
62              </Param>
63              <Param name="skymap_png_x509" dataType="string" value="
                    https://gracedb.ligo.org/api/events/G184098/files/LIB_skymap.png"
                     ucd="meta.ref.url" unit="">
64                  <Description>Sky Map image X509 protected</Description>
65              </Param>
66              <Param name="skymap_png_basic" dataType="string" value="
                    https://gracedb.ligo.org/apibasic/events/G184098/files/LIB_skymap
                    .png" ucd="meta.ref.url" unit="">
67                  <Description>Sky Map image basic auth protected</Description>
68              </Param>
69          </Group>
70      </What>
71      <WhereWhen>
72          <ObsDataLocation>
73              <ObservatoryLocation id="LIGO Virgo"/>
74              <ObservationLocation>
75                  <AstroCoordSystem id="UTC-FK5-GEO"/>
76                  <AstroCoords coord_system_id="UTC-FK5-GEO">
77                      <Time>
78                          <TimeInstant>
79                              <ISOTime>2015-09-14T09:50:45.391000</ISOTime>
80                          </TimeInstant>
81                      </Time>
82                  </AstroCoords>
83              </ObservationLocation>
84          </ObsDataLocation>
85      </WhereWhen>
86      <How>
87          <Description>Candidate gravitational wave event identified by low-latency
                analysis</Description>
88          <Description>H1: LIGO Hanford 4 km gravitational wave detector</Description>
89          <Description>L1: LIGO Livingston 4 km gravitational wave detector<
                /Description>
90      </How>
91      <Citations>
```

```
92          <EventIVORN cite="supersedes">ivo://gwnet/gcn_sender#G184098-7-
                Initial</EventIVORN>
93          <EventIVORN cite="supersedes">ivo://gwnet/gcn_sender#G184098-6-
                Preliminary</EventIVORN>
94          <EventIVORN cite="supersedes">ivo://gwnet/gcn_sender#G184098-5-Update
                </EventIVORN>
95          <EventIVORN cite="supersedes">ivo://gwnet/gcn_sender#G184098-4-
                Initial</EventIVORN>
96          <EventIVORN cite="supersedes">ivo://gwnet/gcn_sender#G184098-3-
                Preliminary</EventIVORN>
97          <EventIVORN cite="supersedes">ivo://gwnet/gcn_sender#G184098-2-
                Retraction</EventIVORN>
98          <EventIVORN cite="supersedes">ivo://gwnet/gcn_sender#G184098-1-
                Preliminary</EventIVORN>
99          <Description>Updated localization is now available</Description>
100     </Citations>
101     <Description>Report of a candidate gravitational wave event</Description>
102 </voe:VOEvent>
```

Appendix B

Appendix B: LIGO/Virgo Notices for GW170817

The following are the machine-readable LIGO/Virgo Notices (i.e., VOEvents) sent to GCN for the gravitational-wave candidate event G298048, later known as GW170817, the first ever observed binary neutron star coalescence (Abbott et al., 2017a). VOEvent information is repackaged by GCN before being sent to our observing partners. As can be seen, for O2, we provided our observing partners with `EM-Bright` information, in this case giving both ProbHasNS and ProbHasRemnant equal to 1 for GW170817. The three-detector skymap available with the LIGO/Virgo Update Notice sent nearly 5 hours later aided the follow-up efforts that led to the detection of the afterglow counterparts.

```
<?xml version="1.0" ?>
<voe:VOEvent xmlns:xsi="http://www.w3.org/2001/XMLSchema-instance"
xmlns:voe="http://www.ivoa.net/xml/VOEvent/v2.0"
xsi:schemaLocation="http://www.ivoa.net/xml/VOEvent/v2.0 http://www.ivoa.
    net/xml/VOEvent/VOEvent-v2.0.xsd"
 version="2.0" role="observation" ivorn="ivo://gwnet/gcn_sender#G298048-1-Initial
     ">
    <Who>
        <Date>2017-08-17T13:08:15</Date>
        <Author>
            <contactName>LIGO Scientific Collaboration and Virgo Collaboration<
                /contactName>
        </Author>
    </Who>
    <What>
        <Param name="internal" dataType="int" value="0">
            <Description>Indicates whether this event should be distributed to
                LSC/Virgo members only</Description>
        </Param>
        <Param name="Pkt_Ser_Num" dataType="string" value="1"/>
        <Param name="GraceID" dataType="string" value="G298048" ucd="meta.id">
            <Description>Identifier in GraceDB</Description>
        </Param>
        <Param name="AlertType" dataType="string" value="Initial" ucd="meta.
            version" unit="">
```

```
21          <Description>VOEvent alert type</Description>
22      </Param>
23      <Param name="Retraction" dataType="string" value="false" ucd="meta.code
            " unit="">
24          <Description>Set to true if the event is retracted.</Description>
25      </Param>
26      <Param name="HardwareInj" dataType="int" value="0" ucd="meta.number"
            unit="">
27          <Description>Indicates that this event is a hardware injection if 1, no
                if 0</Description>
28      </Param>
29      <Param name="Vetted" dataType="int" value="1" ucd="meta.number" unit="
            ">
30          <Description>Indicates whether this candidate has undergone basic
                vetting by humans</Description>
31      </Param>
32      <Param name="OpenAlert" dataType="int" value="0" ucd="meta.number" unit
            ="">
33          <Description>Indicates that this event is an open alert if 1, no if 0<
                /Description>
34      </Param>
35      <Param name="EventPage" dataType="string" value="https://gracedb.ligo.
            org/events/G298048" ucd="meta.ref.url">
36          <Description>Web page for evolving status of this candidate event<
                /Description>
37      </Param>
38      <Param name="Instruments" dataType="string" value="H1" ucd="meta.code"
            >
39          <Description>List of instruments used in analysis to identify this event
                </Description>
40      </Param>
41      <Param name="FAR" dataType="float" value="3.47773444765e-12" ucd="arith
            .rate;stat.falsealarm" unit="Hz">
42          <Description>False alarm rate for GW candidates with this strength or
                greater</Description>
43      </Param>
44      <Param name="Group" dataType="string" value="CBC" ucd="meta.code" unit=
            "">
45          <Description>Data analysis working group</Description>
46      </Param>
47      <Param name="Pipeline" dataType="string" value="gstlal" ucd="meta.code"
             unit="">
48          <Description>Low-latency data analysis pipeline</Description>
49      </Param>
50      <Param name="Search" dataType="string" value="O2VirgoTest" ucd="meta.
            code" unit="">
51          <Description>Specific low-latency search</Description>
52      </Param>
53      <Param name="ProbHasNS" dataType="float" value="1.0" ucd="stat.
            probability" unit="">
54          <Description>Probability that at least one object in the binary is less
                than 3 solar masses</Description>
55      </Param>
56      <Param name="ProbHasRemnant" dataType="float" value="1.0" ucd="stat.
            probability" unit="">
57          <Description>Probability that there is matter in the surroundings of the
                central object</Description>
58      </Param>
59      <Group type="GW_SKYMAP" name="bayestar-CBCO2VirgoTest">
60          <Param name="skymap_fits_shib" dataType="string" value="
                https://gracedb.ligo.org/events/G298048/files/bayestar.fits.gz"
```

```
                ucd="meta.ref.url" unit="">
61              <Description>Sky Map FITS Shibboleth protected</Description>
62          </Param>
63          <Param name="skymap_fits_x509" dataType="string" value="
                https://gracedb.ligo.org/api/events/G298048/files/bayestar.fits.
                gz" ucd="meta.ref.url" unit="">
64              <Description>Sky Map FITS X509 protected</Description>
65          </Param>
66          <Param name="skymap_fits_basic" dataType="string" value="
                https://gracedb.ligo.org/apibasic/events/G298048/files/bayestar.
                fits.gz" ucd="meta.ref.url" unit="">
67              <Description>Sky Map FITS basic auth protected</Description>
68          </Param>
69          <Param name="skymap_png_shib" dataType="string" value="
                https://gracedb.ligo.org/events/G298048/files/bayestar.png" ucd="
                meta.ref.url" unit="">
70              <Description>Sky Map image Shibboleth protected</Description>
71          </Param>
72          <Param name="skymap_png_x509" dataType="string" value="
                https://gracedb.ligo.org/api/events/G298048/files/bayestar.png"
                ucd="meta.ref.url" unit="">
73              <Description>Sky Map image X509 protected</Description>
74          </Param>
75          <Param name="skymap_png_basic" dataType="string" value="
                https://gracedb.ligo.org/apibasic/events/G298048/files/bayestar.
                png" ucd="meta.ref.url" unit="">
76              <Description>Sky Map image basic auth protected</Description>
77          </Param>
78      </Group>
79  </What>
80  <WhereWhen>
81      <ObsDataLocation>
82          <ObservatoryLocation id="LIGO Virgo"/>
83          <ObservationLocation>
84              <AstroCoordSystem id="UTC-FK5-GEO"/>
85              <AstroCoords coord_system_id="UTC-FK5-GEO">
86                  <Time>
87                      <TimeInstant>
88                          <ISOTime>2017-08-17T12:41:04.445710</ISOTime>
89                      </TimeInstant>
90                  </Time>
91              </AstroCoords>
92          </ObservationLocation>
93      </ObsDataLocation>
94  </WhereWhen>
95  <How>
96      <Description>Candidate gravitational wave event identified by low-latency
            analysis</Description>
97      <Description>H1: LIGO Hanford 4 km gravitational wave detector</Description>
98  </How>
99  <Description>Report of a candidate gravitational wave event</Description>
100 </voe:VOEvent>
```

```
<?xml version="1.0" ?>
<voe:VOEvent xmlns:xsi="http://www.w3.org/2001/XMLSchema-instance"
xmlns:voe="http://www.ivoa.net/xml/VOEvent/v2.0"
xsi:schemaLocation="http://www.ivoa.net/xml/VOEvent/v2.0 http://www.ivoa.
    net/xml/VOEvent/VOEvent-v2.0.xsd"
 version="2.0" role="observation" ivorn="ivo://gwnet/gcn_sender#G298048-2-Update"
     >
    <Who>
        <Date>2017-08-17T17:49:40</Date>
        <Author>
            <contactName>LIGO Scientific Collaboration and Virgo Collaboration<
                /contactName>
        </Author>
    </Who>
    <What>
        <Param name="internal" dataType="int" value="0">
            <Description>Indicates whether this event should be distributed to
                LSC/Virgo members only</Description>
        </Param>
        <Param name="Pkt_Ser_Num" dataType="string" value="2"/>
        <Param name="GraceID" dataType="string" value="G298048" ucd="meta.id">
            <Description>Identifier in GraceDB</Description>
        </Param>
        <Param name="AlertType" dataType="string" value="Update" ucd="meta.
            version" unit="">
            <Description>VOEvent alert type</Description>
        </Param>
        <Param name="Retraction" dataType="string" value="false" ucd="meta.code
            " unit="">
            <Description>Set to true if the event is retracted.</Description>
        </Param>
        <Param name="HardwareInj" dataType="int" value="0" ucd="meta.number"
            unit="">
            <Description>Indicates that this event is a hardware injection if 1, no
                if 0</Description>
        </Param>
        <Param name="Vetted" dataType="int" value="1" ucd="meta.number" unit=""
            >
            <Description>Indicates whether this candidate has undergone basic
                vetting by humans</Description>
        </Param>
        <Param name="OpenAlert" dataType="int" value="0" ucd="meta.number" unit
            ="">
            <Description>Indicates that this event is an open alert if 1, no if 0<
                /Description>
        </Param>
        <Param name="EventPage" dataType="string" value="https://gracedb.ligo.
            org/events/G298048" ucd="meta.ref.url">
            <Description>Web page for evolving status of this candidate event<
                /Description>
        </Param>
        <Param name="Instruments" dataType="string" value="H1" ucd="meta.code"
            >
            <Description>List of instruments used in analysis to identify this event
                </Description>
        </Param>
        <Param name="FAR" dataType="float" value="3.47773444765e-12" ucd="arith
            .rate;stat.falsealarm" unit="Hz">
            <Description>False alarm rate for GW candidates with this strength or
                greater</Description>
        </Param>
```

```
44          <Param name="Group" dataType="string" value="CBC" ucd="meta.code" unit=
                """>
45              <Description>Data analysis working group</Description>
46          </Param>
47          <Param name="Pipeline" dataType="string" value="gstlal" ucd="meta.code"
                 unit="">
48              <Description>Low-latency data analysis pipeline</Description>
49          </Param>
50          <Param name="Search" dataType="string" value="O2VirgoTest" ucd="meta.
                code" unit="">
51              <Description>Specific low-latency search</Description>
52          </Param>
53          <Param name="ProbHasNS" dataType="float" value="1.0" ucd="stat.
                probability" unit="">
54              <Description>Probability that at least one object in the binary is less
                    than 3 solar masses</Description>
55          </Param>
56          <Param name="ProbHasRemnant" dataType="float" value="1.0" ucd="stat.
                probability" unit="">
57              <Description>Probability that there is matter in the surroundings of the
                    central object</Description>
58          </Param>
59          <Group type="GW_SKYMAP" name="bayestar-HLV-CBCO2VirgoTest">
60              <Param name="skymap_fits_shib" dataType="string" value="
                    https://gracedb.ligo.org/events/G298048/files/bayestar-HLV.fits.
                    gz" ucd="meta.ref.url" unit="">
61                  <Description>Sky Map FITS Shibboleth protected</Description>
62              </Param>
63              <Param name="skymap_fits_x509" dataType="string" value="
                    https://gracedb.ligo.org/api/events/G298048/files/bayestar-HLV.
                    fits.gz" ucd="meta.ref.url" unit="">
64                  <Description>Sky Map FITS X509 protected</Description>
65              </Param>
66              <Param name="skymap_fits_basic" dataType="string" value="
                    https://gracedb.ligo.org/apibasic/events/G298048/files/bayestar-
                    HLV.fits.gz" ucd="meta.ref.url" unit="">
67                  <Description>Sky Map FITS basic auth protected</Description>
68              </Param>
69              <Param name="skymap_png_shib" dataType="string" value="
                    https://gracedb.ligo.org/events/G298048/files/bayestar-HLV.png"
                    ucd="meta.ref.url" unit="">
70                  <Description>Sky Map image Shibboleth protected</Description>
71              </Param>
72              <Param name="skymap_png_x509" dataType="string" value="
                    https://gracedb.ligo.org/api/events/G298048/files/bayestar-HLV.
                    png" ucd="meta.ref.url" unit="">
73                  <Description>Sky Map image X509 protected</Description>
74              </Param>
75              <Param name="skymap_png_basic" dataType="string" value="
                    https://gracedb.ligo.org/apibasic/events/G298048/files/bayestar-
                    HLV.png" ucd="meta.ref.url" unit="">
76                  <Description>Sky Map image basic auth protected</Description>
77              </Param>
78          </Group>
79      </What>
80      <WhereWhen>
81          <ObsDataLocation>
82              <ObservatoryLocation id="LIGO Virgo"/>
83              <ObservationLocation>
84                  <AstroCoordSystem id="UTC-FK5-GEO"/>
85                  <AstroCoords coord_system_id="UTC-FK5-GEO">
```

```
86                      <Time>
87                          <TimeInstant>
88                              <ISOTime>2017-08-17T12:41:04.445710</ISOTime>
89                          </TimeInstant>
90                      </Time>
91                  </AstroCoords>
92              </ObservationLocation>
93          </ObsDataLocation>
94      </WhereWhen>
95      <How>
96          <Description>Candidate gravitational wave event identified by low-latency
                analysis</Description>
97          <Description>H1: LIGO Hanford 4 km gravitational wave detector</Description>
98          <Description>A gravitational wave trigger identified a possible counterpart
                GRB</Description>
99      </How>
100     <Citations>
101         <EventIVORN cite="supersedes">ivo://gwnet/gcn_sender#G298048-1-
                Initial</EventIVORN>
102         <Description>Updated localization is now available</Description>
103     </Citations>
104     <Description>Report of a candidate gravitational wave event</Description>
105 </voe:VOEvent>
```

Index

Bibliography

Abbott, B. P., Abbott, R., Abbott, T. D., et al. 2016, Physical Review Letters, 116, 131103, doi: 10.1103/PhysRevLett.116.131103

Abbott, B. P., Abbott, R., Abbott, T. D., et al. 2016a, Astrophysical Journal Letters, 826, L13, doi: 10.3847/2041-8205/826/1/L13

—. 2016b, Physical Review Letters, 116, 061102, doi: 10.1103/PhysRevLett.116.061102

—. 2016c, Physical Review Letters, 116, 241103, doi: 10.1103/PhysRevLett.116.241103

—. 2017a, Physical Review Letters, 119, 161101, doi: 10.1103/PhysRevLett.119.161101

—. 2017b, Astrophysical Journal Letters, 848, L12, doi: 10.3847/2041-8213/aa91c9

—. 2017c, Physical Review Letters, 118, 221101, doi: 10.1103/PhysRevLett.118.221101

Abbott, B. P., Abbott, R., Abbott, T. D., et al. 2017, Physical Review Letters, 119, 161101, doi: 10.1103/PhysRevLett.119.161101

Abbott, B. P., Abbott, R., Abbott, T. D., et al. 2017a, Astrophysical Journal Letters, 848, L13, doi: 10.3847/2041-8213/aa920c

—. 2017b, Astrophysical Journal Letters, 850, L40, doi: 10.3847/2041-8213/aa93fc

—. 2018, arXiv e-prints. https://arxiv.org/abs/1811.12907

Abbott, B. P., Abbott, R., Abbott, T. D., et al. 2018, Phys. Rev. Lett., 121, 161101, doi: 10.1103/PhysRevLett.121.161101

Abbott, B. P., Abbott, R., Abbott, T. D., et al. 2018a, All-sky search for short gravitational-wave bursts in the second Advanced LIGO and Virgo run, Tech. Rep. LIGO-P1800308, LIGO Scientific Collaboration and Virgo Collaboration

—. 2018b, Physical Review D, 97, 102002, doi: 10.1103/PhysRevD.97.102002

—. 2019, arXiv e-prints. https://arxiv.org/abs/1901.03310

Acernese, F., Agathos, M., Agatsuma, K., et al. 2015, Classical and Quantum Gravity, 32, 024001, doi: 10.1088/0264-9381/32/2/024001

Adams, T., Buskulic, D., Germain, V., et al. 2016, Classical and Quantum Gravity, 33, 175012, doi: 10.1088/0264-9381/33/17/175012

Albert, A., André, M., Anghinolfi, M., et al. 2017, Astrophysical Journal Letters, 850, L35, doi: 10.3847/2041-8213/aa9aed

Andresen, H., Mueller, B., Mueller, E., & Janka, H. T. 2017, in Monthly Notices of the Royal Astronomical Society, 2032–2051, doi: 10.1093/mnras/stx618

Antoniadis, J., Freire, P. C. C., Wex, N., et al. 2013, Science, 340, 1233232, doi: 10.1126/science.1233232

Ashton, G., Burns, E., Dal Canton, T., et al. 2018, Astrophysical Journal, 860, 6, doi: 10.3847/1538-4357/aabfd2

Baade, W., & Zwicky, F. 1934, in Proceedings of the National Academy of Sciences of the United States of America, 254–259, doi: 10.1073/pnas.20.5.254

Baring, M. G., & Harding, A. K. 1998, Astrophysical Journal Letters, 507, L55, doi: 10.1086/311679

Barsotti, L., Fritschel, P., Evans, M., & Gras, S. 2018, Updated Advanced LIGO sensitivity design curve, https://dcc.ligo.org/LIGO-T1800044/public

Barthelmy, S. D., Chincarini, G., Burrows, D. N., et al. 2005, Nature, 438, 994, doi: 10.1038/nature04392

Bauswein, A., & Janka, H. T. 2012, Physical Review Letters, 108, 011101, doi: 10.1103/PhysRevLett.108.011101

Berger, E., Price, P. A., Cenko, S. B., et al. 2005, Nature, 438, 988, doi: 10.1038/nature04238

Bethe, H. A. 1990, Reviews of Modern Physics, 62, 801, doi: 10.1103/RevModPhys.62.801

Bethe, H. A., & Johnson, M. B. 1974, Nuclear Phys, 230, 1, doi: 10.1016/0375-9474(74)90528-4

Bethe, H. A., & Wilson, J. R. 1985, Astrophysical Journal, 295, 14, doi: 10.1086/163343

Biswas, R., Blackburn, L., Cao, J., et al. 2013, Physical Review D, 88, 062003, doi: 10.1103/PhysRevD.88.062003

Biwer, C., Barker, D., Batch, J. C., et al. 2017, Physical Review D, 95, 062002, doi: 10.1103/PhysRevD.95.062002

Blanco-Pillado, J. J., Olum, K. D., & Shlaer, B. 2014, Physical Review D, 89, 023512, doi: 10.1103/PhysRevD.89.023512

Blondin, J. M., Mezzacappa, A., & DeMarino, C. 2003, Astrophysical Journal, 584, 971, doi: 10.1086/345812

Bruenn, S. W., De Nisco, K. R., & Mezzacappa, A. 2001, Astrophysical Journal, 560, 326, doi: 10.1086/322319

Buonanno, A., & Sathyaprakash, B. S. 2014, ArXiv e-prints. https://arxiv.org/abs/1410.7832

Burbidge, E. M., Burbidge, G. R., Fowler, W. A., & Hoyle, F. 1957, Reviews of Modern Physics, 29, 163, doi: 10.1103/RevModPhys.29.547

Burrows, A., & Ostriker, J. P. 2014, in Proceedings of the National Academy of Sciences of the United States of America, 2409–2416, doi: 10.1073/pnas.1318003111

Camilo, F., Ransom, S. M., Halpern, J. P., et al. 2006, Nature, 442, 892, doi: 10.1038/nature04986

Camilo, F., Cognard, I., Ransom, S. M., et al. 2007, Astrophysical Journal, 663, 497

Cannon, K., Hanna, C., & Peoples, J. 2015, ArXiv e-prints. https://arxiv.org/abs/1504.04632

Chandrasekhar, S. 1931, Astrophysical Journal, 74, 81, doi: 10.1086/143324

Chatterji, S., Blackburn, L., Martin, G., & Katsavounidis, E. 2004, Classical and Quantum Gravity, 21, S1809, doi: 10.1088/0264-9381/21/20/024

Cho, H.-S., Ochsner, E., O'Shaughnessy, R., Kim, C., & Lee, C.-H. 2013, Physical Review D, 87, 024004, doi: 10.1103/PhysRevD.87.024004

Chu, Q. 2017, PhD thesis, The University of Western Australia

Colgate, S. A., & White, R. H. 1966, Astrophysical Journal, 143, 626, doi: 10.1086/148549

Connaughton, V., Burns, E., Goldstein, A., et al. 2016, Astrophysical Journal Letters, 826, L6, doi: 10.3847/2041-8205/826/1/L6

Copeland, E. J., & Kibble, T. W. B. 2009, Proceedings of the Royal Society of London Series A, 466, 623, doi: 10.1098/rspa.2009.0591

Copeland, E. J., Myers, R. C., & Polchinski, J. 2004, Journal of High Energy Physics, 6, 013, doi: 10.1088/1126-6708/2004/06/013

Corsi, A., & Owen, B. J. 2011, Physical Review D, 83, 104014, doi: 10.1103/PhysRevD.83.104014

Cowan, C. L., Reines, F., Harrison, F. B., Kruse, H. W., & McGuire, A. D. 1956, Science, 124, 103, doi: 10.1126/science.124.3212.103

Dal Canton, T., & Harry, I. W. 2017, ArXiv e-prints. https://arxiv.org/abs/1705.01845

Dálya, G., Galgóczi, G., Dobos, L., et al. 2018, Monthly Notices of the Royal Astronomical Society, 479, 2374, doi: 10.1093/mnras/sty1703

Damour, T., & Vilenkin, A. 2000, Physical Review Letters, 85, 3761, doi: 10.1103/PhysRevLett.85.3761

D'Avanzo, P., Campana, S., Ghisellini, G., et al. 2018, ArXiv e-prints. https://arxiv.org/abs/1801.06164

Davidsen, A., Margon, B., Liebert, J., et al. 1975, Astrophysical Journal, 200, L19

Demorest, P. B., Pennucci, T., Ransom, S. M., Roberts, M. S. E., & Hessels, J. W. T. 2010, Nature, 467, 1081, doi: 10.1038/nature09466

Dobie, D., Kaplan, D. L., Murphy, T., et al. 2018, ArXiv e-prints. https://arxiv.org/abs/1803.06853

Duncan, R. C., & Thompson, C. 1992, Astrophysical Journal Letters, 392, L9, doi: 10.1086/186413

Einstein, A. 1916, in Sitzungsberichte der Königlich Preussischen Akademie der Wissenschaften Berlin, 688–696

Einstein, A. 1918, in Sitzungsberichte der Königlich Preussischen Akademie der Wissenschaften Berlin, 154–167

Ellis, C. D. 1937, in Proceedings of the Royal Society A, 447–460, doi: 10.1098/rspa.1937.0155

Ertan, Ü., Çalışkan, Ş., Benli, O., & Alpar, M. A. 2014, Monthly Notices of the Royal Astronomical Society, 444, 1559, doi: 10.1093/mnras/stu1523

Essick, R., Blackburn, L., & Katsavounidis, E. 2013, Classical and Quantum Gravity, 30, 155010, doi: 10.1088/0264-9381/30/15/155010

Essick, R., Vitale, S., Katsavounidis, E., Vedovato, G., & Klimenko, S. 2015, Astrophysical Journal, 800, 81

Fahlman, G. G., & Gregory, P. C. 1981, Nature, 293, 202, doi: 10.1038/293202a0

Farr, W. M., Gair, J. R., Mandel, I., & Cutler, C. 2015, Phys. Rev. D, 91, 023005, doi: 10.1103/PhysRevD.91.023005

Foglizzo, T., Kazeroni, R., Guilet, J., et al. 2015, Publications of the Astronomical Society of Australia, 32, doi: 10.1017/pasa.2015.9

Ford, K. E. S., Fraschetti, F., Fryer, C., et al. 2019, arXiv e-prints. https://arxiv.org/abs/1903.11116

Foucart, F. 2012, Physical Review D, 86, 124007, doi: 10.1103/PhysRevD.86.124007

Fox, D. B., Frail, D. A., Price, P. A., et al. 2005, Nature, 437, 845, doi: 10.1038/nature04189

Franco, L. M., Link, B., & Epstein, R. I. 2000, Astrophysical Journal, 543, 987

Gehrels, N., Chincarini, G., Giommi, P., et al. 2004, Astrophysical Journal, 611, 1005, doi: 10.1086/422091

Gehrels, N., Sarazin, C. L., O'Brien, P. T., et al. 2005, Nature, 437, 851, doi: 10.1038/nature04142

Goldstein, A., Veres, P., Burns, E., et al. 2017, Astrophysical Journal Letters, 848, L14, doi: 10.3847/2041-8213/aa8f41

Haggard, D., Nynka, M., Ruan, J. J., et al. 2017, Astrophysical Journal Letters, 848, L25, doi: 10.3847/2041-8213/aa8ede

Harry, G. M., & the LIGO Scientific Collaboration. 2010, Classical and Quantum Gravity, 27, 084006

Herant, M., Benz, W., Hix, W. R., Fryer, C. L., & Colgate, S. A. 1994, Astrophysical Journal, 435, 339, doi: 10.1086/174817

Hewish, A., Bell, S. J., Pilkington, J. D. H., Scott, P. F., & Collins, R. A. 1968, Nature, 217, 709, doi: 10.1038/217709a0

Hicken, M., Friedman, A. S., Blondin, S., et al. 2017, Astrophysical Journal Supplement Series, 233, 6, doi: 10.3847/1538-4365/aa8ef4

Hjorth, J., Watson, D., Fynbo, J. P. U., et al. 2005, Nature, 437, 859, doi: 10.1038/nature04174

Hulleman, F., van Kerkwijk, M. H., & Kulkarni, S. R. 2000, Nature, 408, 689, doi: 10.1038/35047024

Hulse, R., & Taylor, J. H. 1975, Astrophysical Journal, 195, L51

Hurley, K. 2011, Advances in Space Research, 47, 1337, doi: 10.1016/j.asr.2010.08.036

Hurley, K., Kouveliotou, C., Woods, P., et al. 1999, Astrophysical Journal Letters, 510, L107, doi: 10.1086/311821

Hurley, K., Boggs, S. E., Smith, D. M., et al. 2005, Nature, 434, 1098, doi: 10.1038/nature03519

Iben, Jr., I., & Tutukov, A. V. 1984, Astrophysical Journal Supplement Series, 54, 335, doi: 10.1086/190932

—. 1996, Astrophysical Journal, 456, 738, doi: 10.1086/176693

Israel, G., Stella, L., Covino, S., et al. 2004, in IAU Symposium, Vol. 218, Young Neutron Stars and Their Environments, ed. F. Camilo & B. M. Gaensler, 247

Israel, G. L., Covino, S., Stella, L., et al. 2002, Astrophysical Journal Letters, 580, L143, doi: 10.1086/345612

Israel, G. L., Covino, S., Perna, R., et al. 2003, Astrophysical Journal Letters, 589, L93, doi: 10.1086/375832

Izumi, K., & Sigg, D. 2017, Classical and Quantum Gravity, 34, 015001, doi: 10.1088/0264-9381/34/1/015001

Janka, H.-T. 2001, Astronomy & Astrophysics, 368, 527, doi: 10.1051/0004-6361:20010012

—. 2012, Annual Review of Nuclear and Particle Science, 62, 407, doi: 10.1146/annurev-nucl-102711-094901

Janka, H.-T., Hanke, F., Hüdepohl, L., et al. 2012, Progress of Theoretical and Experimental Physics, 2012, 01A309, doi: 10.1093/ptep/pts067

Kanner, J., Huard, T. L., Márka, S., et al. 2008, Classical and Quantum Gravity, 25, 184034, doi: 10.1088/0264-9381/25/18/184034

Kanner, J. B. 2011, PhD thesis, University of Maryland, College Park

Kapadia, S. J., Caudill, S., Creighton, J. D. E., et al. 2018, A self-consistent method to estimate the rate of compact binary coalescences with a Poisson mixture model, Tech. Rep. LIGO-T1800072, LIGO Scientific Collaboration and Virgo Collaboration

Kashiyama, K., Murase, K., Bartos, I., Kiuchi, K., & Margutti, R. 2016, Astrophysical Journal, 818, 94, doi: 10.3847/0004-637X/818/1/94

Kaspi, V. M., Gavriil, F. P., Woods, P. M., et al. 2003, Astrophysical Journal Letters, 588, L93

Keil, W., Janka, H.-T., & Mueller, E. 1996, Astrophysical Journal Letters, 473, 111

Klimenko, S., Vedovato, G., Drago, M., et al. 2016, Physical Review D, 93, 042004, doi: 10.1103/PhysRevD.93.042004

Kotake, K. 2013, Comptes Rendus Physique, 14, 318, doi: 10.1016/j.crhy.2013.01.008

Kouveliotou, C. 1999, in Proceedings of the National Academy of Sciences of the United States of America, Vol. 96, doi: https://doi.org/10.1073/pnas.96.10.5351

Kumar, H. S., & Safi-Harb, S. 2008, Astrophysical Journal Letters, 678, L43

Kuroda, T., Kotake, K., Hayama, K., & Takiwaki, T. 2017, Astrophysical Journal, 851, 62, doi: 10.3847/1538-4357/aa988d

Kyutoku, K., Shibata, M., & Taniguchi, K. 2010, Physical Review D, 82, 044049, doi: 10.1103/PhysRevD.82.044049

—. 2011, Physical Review D, 84, 049902, doi: 10.1103/PhysRevD.84.049902

Lattimer, J. M. 2012, Annual Review of Nuclear and Particle Science, 62, 485, doi: 10.1146/annurev-nucl-102711-095018

Lattimer, J. M., & Prakash, M. 2011, in From Nuclei to Stars: Festschrift in Honor of Gerald E Brown, ed. S. Lee, 275

Lentz, E. J., Bruenn, S. W., Hix, W. R., et al. 2015, Astrophysical Journal Letters, 807

Li, L.-X., & Paczyński, B. 1998, Astrophysical Journal Letters, 507, L59, doi: 10.1086/311680

Liebendörfer, M., Rampp, M., Janka, H.-T., & Mezzacappa, A. 2005, Astrophysical Journal, 620, 840

LIGO Scientific Collaboration, & Virgo Collaboration. 2017, GRB Coordinates Network, 20982

Lorenz, L., Ringeval, C., & Sakellariadou, M. 2010, Journal of Cosmology and Astroparticle Physics, 10, 003, doi: 10.1088/1475-7516/2010/10/003

Lorimer, D. R. 2008, Living Reviews in Relativity, 11, 8, doi: 10.12942/lrr-2008-8

Lorimer, D. R., & Kramer, M. 2004, Handbook of Pulsar Astronomy (Cambridge University Press)

Lynch, R., Vitale, S., Essick, R., Katsavounidis, E., & Robinet, F. 2017, Physical Review D, 95, 104046, doi: 10.1103/PhysRevD.95.104046

Marassi, S., Ciolfi, R., Schneider, R., Stella, L., & Ferrari, V. 2011, Monthly Notices of the Royal Astronomical Society, 411, 2549, doi: 10.1111/j.1365-2966.2010.17861.x

Marek, A., & Janka, H.-T. 2009, Astrophysical Journal, 694, 664

Margutti, R., Alexander, K. D., Xie, X., et al. 2018, ArXiv e-prints. https://arxiv.org/abs/1801.03531

Mazets, E. P., & Golenetskii, S. V. 1981, Astrophysics and Space Science, 75, 47, doi: 10.1007/BF00651384

Mazets, E. P., Golenetskij, S. V., & Guryan, Y. A. 1979a, Soviet Astronomy Letters, 5, 641

Mazets, E. P., Golentskii, S. V., Ilinskii, V. N., Aptekar, R. L., & Guryan, I. A. 1979b, Nature, 282, 587, doi: 10.1038/282587a0

Mereghetti, S. 2008, Astronomy and Astrophysics Review, 15, 225, doi: 10.1007/s00159-008-0011-z

Messer, O. E. B., Harris, J. A., Parete-Koon, S., & Chertkow, M. A. 2013, in Applied Parallel and Scientific Computing: 11th International Conference, ed. P. Manninen & P. Oster, 92–106

Messick, C., Blackburn, K., Brady, P., et al. 2017, Physical Review D, 95, 042001, doi: 10.1103/PhysRevD.95.042001

Metzger, B. D., Bauswein, A., Goriely, S., & Kasen, D. 2015, Monthly Notices of the Royal Astronomical Society, 446, 1115, doi: 10.1093/mnras/stu2225

Metzger, B. D., & Berger, E. 2012, Astrophysical Journal, 746, 48, doi: 10.1088/0004-637X/746/1/48

Metzger, B. D., & Fernández, R. 2014, Monthly Notices of the Royal Astronomical Society, 441, 3444, doi: 10.1093/mnras/stu802

Mezzacappa, A., Liebendörfer, M., Cardall, C. Y., Messer, O. E. B., & Bruenn, S. W. 2006, in Computational Methods in Transport: Granlibakken 2004, ed. F. Graziani, Vol. 48, doi: 10.1007/3-540-28125-8_3

Mezzacappa, A., Bruenn, S. W., Lentz, E. J., et al. 2014, Recent Progress on Ascertaining the Core Collapse Supernova Explosion Mechanism. https://arxiv.org/abs/1501.01688

Miller, M. C. 2013, ArXiv e-prints. https://arxiv.org/abs/1312.0029

Miller, M. C., & Lamb, F. K. 2016, European Physical Journal A, 52, 63, doi: 10.1140/epja/i2016-16063-8

Minkowski, R. 1941, Publications of the Astronomical Society of the Pacific, 53, 224, doi: 10.1086/125315

Misner, C. W., Thorne, K. S., & Wheeler, J. A. 1973, Gravitation (W. H. Freeman and Company)

Mukherjee, D., et al. 2017, On the bank used in Advanced LIGO's second observing run by the GstLAL search for inspiraling compact binaries, Tech. Rep. LIGO-P1700412, LIGO Scientific Collaboration and Virgo Collaboration

Murase, K., Dasgupta, B., & Thompson, T. A. 2014, Physical Review D, 89, 043012, doi: 10.1103/PhysRevD.89.043012

Murphy, J. W., Ott, C. D., & Burrows, A. 2009, Astrophysical Journal, 707, 1173

Nakamura, K., Horiuchi, S., Tanaka, M., et al. 2016, in Monthly Notices of the Royal Astronomical Society, Vol. 461, 3296–3313

Nather, R. E., Robinson, E. L., & Stover, R. J. 1981, Astrophysical Journal, 244, 269, doi: 10.1086/158704

Necula, V., Klimenko, S., & Mitselmakher, G. 2012, in Journal of Physics Conference Series, Vol. 363, Journal of Physics Conference Series, 012032, doi: 10.1088/1742-6596/363/1/012032

Negreiros, R., Bernal, C., Dexheimer, V., & Troconis, O. 2018, Universe, 4, 43, doi: 10.3390/universe4030043

Nitz, A. H. 2018, Classical and Quantum Gravity, 35, 035016, doi: 10.1088/1361-6382/aaa13d

Nitz, A. H., Dal Canton, T., Davis, D., & Reyes, S. 2018, Physical Review D, 98, 024050, doi: 10.1103/PhysRevD.98.024050

Nomoto, K. 1984, Astrophysical Journal, 277, 791, doi: 10.1086/161749

—. 1987, Astrophysical Journal, 322, 206, doi: 10.1086/165716

Olausen, S. A., & Kaspi, V. M. 2014, Astrophysical Journal Supplement Series, 212, 6, doi: https://doi.org/10.1088/0067-0049/212/1/6

Oppenheimer, J. R., & Snyder, H. 1939, Physical Review, 56, 455, doi: 10.1103/PhysRev.56.455

Ott, C. 2009, Classical and Quantum Gravity, 26, 063001, doi: 10.1088/0264-9381/26/6/063001

—. 2014, Core Collapse Supernovae and Compact Object Mergers, http://hipacc.ucsc.edu/LectureSlides/25/456/140722_2_Ott.pdf

Özel, F., Psaltis, D., Ransom, S., Demorest, P., & Alford, M. 2010, Astrophysical Journal Letters, 724, L199, doi: 10.1088/2041-8205/724/2/L199

Palmer, D. M., Barthelmy, S., Gehrels, N., et al. 2005, Nature, 434, 1107, doi: 10.1038/nature03525

Pankow, C. 2018, Projected Event Detection Rates in O3, Tech. Rep. LIGO-G1800370, LIGO Scientific Collaboration and Virgo Collaboration

Pannarale, F., & Ohme, F. 2014, Astrophysical Journal Letters, 791, L7

Pauli, W. 1925, Zeitschrift für Physik, 31, 765, doi: 10.1007/bf02980631

Poisson, E., & Will, C. M. 2014, Gravity (Cambridge University Press)

Pons, J. A., Reddy, S., Prakash, M., Lattimer, J. M., & Miralles, J. A. 1999, Astrophysical Journal, 513, 780

Popov, S. B., & Prokhorov, M. E. 2006, Monthly Notices of the Royal Astronomical Society, 367, 732, doi: 10.1111/j.1365-2966.2005.09983.x

Powell, J., Gossan, S. E., Logue, J., & Heng, I. S. 2016, Physical Review D, 94, 123012, doi: 10.1103/PhysRevD.94.123012

Rea, N., Viganò, D., Israel, G. L., Pons, J. A., & Torres, D. F. 2014, Astrophysical Journal Letters, 781, L17, doi: 10.1088/2041-8205/781/1/L17

Rea, N., Zane, S., Turolla, R., Lyutikov, M., & Götz, D. 2008, Astrophysical Journal, 686, 1245

Rea, N., Israel, G. L., Esposito, P., et al. 2012, Astrophysical Journal, 754, 27

Robinet, F. 2016, Omicron: an algorithm to detect and characterize transient events in gravitational-wave detectors, Tech. Rep. VIR-0545B-14, Virgo Collaboration

Ruan, J. J., Nynka, M., Haggard, D., Kalogera, V., & Evans, P. 2018, Astrophysical Journal Letters, 853, L4, doi: 10.3847/2041-8213/aaa4f3

Sakellariadou, M. 2007, ArXiv e-prints, doi: 10.1007/3-540-70859-6_10

Sathyaprakash, B. S., & Schutz, B. F. 2009, Living Reviews in Relativity, 12, 2, doi: 10.12942/lrr-2009-2

Savchenko, V., Ferrigno, C., Kuulkers, E., et al. 2017, Astrophysical Journal Letters, 848, L15, doi: 10.3847/2041-8213/aa8f94

Schutz, B. F. 2004, Gravity from the Ground Up: An Introductory Guide to Gravity and General Relativity (Cambridge University Press)

Schutz, B. F. 2011, Classical and Quantum Gravity, 28, 125023, doi: 10.1088/0264-9381/28/12/125023

Shenar, T., Hamann, W.-R., & Todt, H. 2014, Astronomy & Astrophysics, 562, A118, doi: 10.1051/0004-6361/201322496

Singer, L. P. 2015, PhD thesis, California Institute of Technology

Singer, L. P., & Price, L. R. 2016, Physical Review D, 93, 024013, doi: 10.1103/PhysRevD.93.024013

Singer, L. P., Chen, H.-Y., Holz, D. E., et al. 2016, Astrophysical Journal Letters, 829, L15

Stott, M. J., Elghozi, T., & Sakellariadou, M. 2017, Physical Review D, 96, 023533, doi: 10.1103/PhysRevD.96.023533

Taylor, J. H., Fowler, L. A., & McCulloch, P. 1979, Nature, 277, 437

Taylor, J. H., Hulse, R. A., Fowler, L. A., Gullahorn, G. E., & Rankin, J. M. 1976, Astrophysical Journal, 206, L53, doi: 10.1086/182131

Taylor, J. H., & Weisberg, J. M. 1982, Astrophysical Journal, 253, 908, doi: 10.1086/159690

Thompson, C., & Beloborodov, A. M. 2005, Astrophysical Journal, 634, 565

Thompson, C., & Duncan, R. C. 2001, Astrophysical Journal, 561, 980

Thompson, C., Lyutikov, M., & Kulkarni, S. R. 2002, Astrophysical Journal, 574, 332

Togashi, H., Nakazatoc, K., Takeharad, Y., et al. 2017, Nuclear Physics A, 961, 78, doi: 10.1016/j.nuclphysa.2017.02.010

Troja, E., Piro, L., van Eerten, H., et al. 2017, Nature, 551, 71, doi: 10.1038/nature24290

Turolla, R., Zane, S., Pons, J. A., Esposito, P., & Rea, N. 2011, Astrophysical Journal, 740, 105

Turolla, R., Zane, S., & Watts, A. L. 2015, Reports on Progress in Physics, 78, 116901, doi: 10.1088/0034-4885/78/11/116901

Tutukov, A., & Yungelson, L. 1996, Monthly Notices of the Royal Astronomical Society, 280, 1035, doi: 10.1093/mnras/280.4.1035

van den Bergh, S., & Tammann, G. A. 1991, Annual Review of Astronomy and Astrophysics, 29, 363, doi: 10.1146/annurev.aa.29.090191.002051

Villasenor, J. S., Lamb, D. Q., Ricker, G. R., et al. 2005, Nature, 437, 855, doi: 10.1038/nature04213

Wanajo, S., Janka, H.-T., & Müller, B. 2010, Astrophysical Journal Letters, 726, L15, doi: 10.1088/2041-8205/726/2/L15

Wanajo, S., Nomoto, K., Janka, H.-T., Kitaura, F. S., & Müller, B. 2009, Astrophysical Journal, 695, 208, doi: 10.1088/0004-637X/695/1/208

Webbink, R. F. 1984, Astrophysical Journal, 277, 355, doi: 10.1086/161701

Weber, J. 1969, Phys. Rev. Lett., 22, 1320, doi: 10.1103/PhysRevLett.22.1320

Weisberg, J. M., Nice, D. J., & Taylor, J. H. 2010, Astrophysical Journal, 722, 1030

Weisberg, J. M., & Taylor, J. H. 2002, Radio Pulsars. https://arxiv.org/abs/astro-ph/0211217

Weisstein, E. W. 2018, Orbital Elements, http://scienceworld.wolfram.com/physics/OrbitalElements.html

Wilson, J. R. 1985, in Numerical Astrophysics, ed. J. M. Centrella, J. M. LeBlanc, & R. L. Bowers, 422

Woosley, S. E., Heger, A., & Weaver, T. A. 2002, Reviews of Modern Physics, 74, 1015, doi: 10.1103/RevModPhys.74.1015

Woosley, S. E., & Weaver, T. A. 1981, in Supernovae: A Survey of Current Research, ed. M. J. Rees & R. J. Stoneham, Vol. 90, 79–122, doi: 10.1007/978-94-009-7876-8_6

Yakunin, K. N., Mezzacappa, A., Marronetti, P., et al. 2015, Physical Review D, 92, 084040, doi: 10.1103/PhysRevD.92.084040

—. 2017, The Gravitational Wave Signal of a Core Collapse Supernova Explosion of a 15$M_\odot$ Star. https://arxiv.org/abs/1701.07325